

---

**Intercellular Interactions Promote Collective Behavior in Bacterial Colonies and Developing Epithelia****Aboutaleb Amiri****Publication Date**

12-04-2017

**License**

This work is made available under a All Rights Reserved license and should only be used in accordance with that license.

**Citation for this work (American Psychological Association 7th edition)**

Amiri, A. (2017). *Intercellular Interactions Promote Collective Behavior in Bacterial Colonies and Developing Epithelia* (Version 1). University of Notre Dame. <https://doi.org/10.7274/bc386h4682f>

This work was downloaded from CurateND, the University of Notre Dame's institutional repository.

For more information about this work, to report or an issue, or to preserve and share your original work, please contact the CurateND team for assistance at [curate@nd.edu](mailto:curate@nd.edu).

INTERCELLULAR INTERACTIONS PROMOTE COLLECTIVE BEHAVIOR IN  
BACTERIAL COLONIES AND DEVELOPING EPITHELIA

A Dissertation

Submitted to the Graduate School  
of the University of Notre Dame  
in Partial Fulfillment of the Requirements  
for the Degree of

Doctor of Philosophy

by

Aboutaleb Amiri

---

Mark Alber, Director

Graduate Program in Physics

Notre Dame, Indiana

April 2017

© Copyright by

Aboutaleb Amiri

2016

All Rights Reserved

# INTERCELLULAR INTERACTIONS PROMOTE COLLECTIVE BEHAVIOR IN BACTERIAL COLONIES AND DEVELOPING EPITHELIA

Abstract

by

Aboutaleb Amiri

Collective behavior has been observed in many animal groups including schools of fish, flocks of birds, as well as in colonies of swarming bacteria, and even in group of cells in epithelial tissues of *Drosophila* fruit fly during development. The self-organizing behavior and adjustment, which results from local interactions, leads to group behavior at time and space scales that are larger than the scale of interactions between individual organisms and cells. In this thesis, we study the impact of physical properties of individual cells and intercellular interactions on the swarming behavior in bacterial colonies and self-organization of epithelial cells during development. In particular, by using combination of computational modeling and experimentation, we explore the role that pili interactions play in expanding swarms of the pathogenic bacterium *Pseudomonas aeruginosa* under different environmental conditions. We find that pili-pili interactions in a colony of wild-type *P. aeruginosa* slow down the swarm expansion as well as enable bacteria to alter their movement to avoid antibiotics. We also demonstrated that periodic reversals of motion direction with periods within the experimentally observed range, high flexibility of bacterial cells and a moderate level of strength of cell-cell adhesion are crucial for a colony of self-propelled rod-shaped *Myxococcus xanthus* to spread protein within the population efficiently. This contact-mediated protein exchange mechanism is necessary for bac-



terial self-organization during predation, fruiting body formation and genetic repair of damaged cells. Finally, we study role of cellular mitotic rounding during growth of epithelial tissues. Our results show that increase of cortical stiffness and reduction in cell-cell adhesion are the main factors in increasing cell roundness, and change in the cytoplasmic pressure is the primary factor that controls the cell size.

This dissertation is dedicated to my family, especially my mother for supporting me throughout my life and studies.

# CONTENTS

FIGURES . . . . .	v
TABLES . . . . .	vi
ACKNOWLEDGMENTS . . . . .	vii
CHAPTER 1: INTRODUCTION . . . . .	1
CHAPTER 2: ROLE OF TYPE IV PILI INTERACTIONS ON SWARMING BEHAVIOR OF PSEUDOMONAS AERUGINOSA . . . . .	7
2.1 Cell based biophysical model . . . . .	7
2.2 Results . . . . .	11
2.2.1 TFP affect cell-cell arrangement during swarming. . . . .	12
2.2.2 Simulations of swarming cells predict that TFP affect collective motion. . . . .	15
2.2.3 TFP interact with other TFP during swarming. . . . .	17
2.3 Discussion . . . . .	20
CHAPTER 3: REVERSALS AND COLLISIONS PROMOTE PROTEIN SPREAD- ING IN BACTERIAL SWARMS . . . . .	24
3.1 Biologically calibrated computational model . . . . .	26
3.2 Evaluation of protein spreading using Shannon entropy . . . . .	31
3.3 Results . . . . .	33
3.3.1 Cell-cell connection rate and duration . . . . .	34
3.3.2 Evaluation of protein spreading efficiency. . . . .	38
3.4 Discussion . . . . .	41
CHAPTER 4: COMPUTATIONAL STUDY OF DEVELOPING EPITHELIA . . . . .	45
4.1 Modeling background . . . . .	49
4.2 SEM computational model . . . . .	50
4.2.1 Subcellular elements . . . . .	52
4.2.2 Equations of motion . . . . .	53
4.2.3 Cell cycle . . . . .	54
4.2.4 Model calibration . . . . .	56
4.3 Results . . . . .	59

4.3.1	Tissue topology emerges from self-organization driven by cellular mechanics. . . . .	59
4.3.2	Impacts of adhesion, stiffness, and cytoplasmic pressure on MR	61
4.4	Discussion . . . . .	66
APPENDIX A: PSEUDOMONAS AERUGINOSA MOTILITY SOURCE CODE		69
A.1	Main.cpp . . . . .	69
A.2	Initializer.cpp . . . . .	77
A.3	BufferFn.h . . . . .	78
A.4	BufferCounter.h . . . . .	79
A.5	CellDistance.h . . . . .	80
APPENDIX B: SENSITIVITY ANALYSIS OF CELL SHAPE AND SIZE . .		83
B.1	Calculation of area and roundness . . . . .	83
B.2	Response surface method . . . . .	84
B.2.1	Exploring the impact of physical properties on MR . . . . .	84
B.2.2	Calibration of mitotic physical parameters . . . . .	84
B.2.3	Improving the resolution of investigating the impact of physical properties on MR . . . . .	85
B.3	Sensitivity analysis . . . . .	85
REFERENCES . . . . .		88

## FIGURES

1.1	Schematics figure of the bacteria <i>P. aeruginosa</i> and <i>M. xanthus</i> . . . .	3
2.1	TFP interaction in simulations. . . . .	9
2.2	Experimental plates of <i>P. aeruginosa</i> plates. . . . .	12
2.3	Alignment between bacteria . . . . .	14
2.4	Clustering in bacterial colony . . . . .	15
2.5	Expansion rate of different populations. . . . .	16
2.6	TFP-deficient cells swarm through the population. . . . .	18
2.7	Mixture of bacteria . . . . .	20
2.8	Wild-type bacteria avoid toxic regions. . . . .	21
3.1	Schematic figure of <i>M. xanthus</i> cells in SCE model. . . . .	29
3.2	Initial distribution of cells in simulations. . . . .	32
3.3	Time evolution of protein distribution. . . . .	33
3.4	Experimental range of reversal period. . . . .	35
3.5	Rate of cell-cell connections and protein spreading in bacterial popu- lations. . . . .	36
3.6	Connection duration and clustering behavior of bacterial colonies. . .	39
4.1	Epithelial mechanics. . . . .	47
4.2	Cell cycle. . . . .	51
4.3	Initialization of simulations. . . . .	57
4.4	Biological calibration of cell mechanical properties in simulations. . .	58
4.5	Biological calibration of the model parameters. . . . .	60
4.6	Topological properties of simulated tissues. . . . .	62
4.7	Contour plots for FFD experiment. . . . .	63
4.8	Contour plots for CCD experiment. . . . .	64
4.9	Sensitivity analysis of mitotic rounding. . . . .	65
B.1	Calculation of area and perimeter. . . . .	83
B.2	Response surface method analysis of mitotic rounding. . . . .	86

## TABLES

3.1	DEFAULT VALUES OF THE MODEL PARAMETERS USED IN SIMULATIONS . . . . .	30
4.1	POTENTIAL ENERGY FUNCTIONS IN THE MODEL . . . . .	52
B.1	VALUES OF THE MODEL PARAMETERS USED TO SIMULATE DEVELOPMENT OF EPITHELIAL TISSUE . . . . .	87

## ACKNOWLEDGMENTS

I would like to especially thank my advisor Dr. Mark Alber for introducing me to the field of computational biology and biophysics and for kindly supporting me during my graduate studies. He generously advised me on how to conduct research, stay focused on the important aspects and present work clearly. I also would like to thank my thesis defense committee members Dr. Zoltán Toroczkai, Dr. Kathie Newman and Dr. Daniel Bardayan for their helpful comments and discussions.

I am thankful to Dr. Jeremiah Zartman and his lab members Pavel Brodskiy, Cody Narciso, Megan Levis and Jamison Jangula for their collaboration and support. Working with Dr. Zartman's lab was a great research experience which helped me extend my knowledge in the field of developmental biology and inspired me to pursue my post-graduate studies in this field. I also would like to express my gratitude to Dr. Joshua Shrout and Dr. Igor Aranson for their fruitful discussions and guidance during my studies. I am very grateful for all the kind help and advise that I received from Dr. Amin Doostmohammadi during my research. I would like to express my deep gratitude to current and former members of Dr. Alber's group Ali Nematbakhsh, Cameron Harvey, Amy Buchmann, Shixin Xu, Shant Mahserjian and Francesco Pancaldi for all helpful discussions. My sincere appreciation to my wonderful friends Melinda Varga, Madan Lamichhane, and my amazing friends from the Iranian community at Notre Dame who made my graduate life a joyful and memorable chapter of my life.

My deepest thanks go to my beloved family, especially my mother, who always wanted the best for me and supported me throughout my life.

## CHAPTER 1

### INTRODUCTION

Collective behavior involves coordinated dynamics of a group of organisms or cells and determines emergent properties at the population level. This can include self-organization, synchronization, pattern formation as well as spreading of proteins at the population level [21]. Modeling studies of collective behavior have produced novel results about dynamics of human populations, flocks of birds, schools of fish, marching ants, swarming insects, self-organization of epithelial cells and swarming bacteria [5, 55, 91, 99]. Collective behavior provides effective strategies, among others, for predation, avoiding predators, and surviving the harsh conditions such as starvation and exposure to antibiotics. In this thesis, we use several novel biologically calibrated computational models coupled with experimental observations to suggest and test mechanisms used by two types of bacteria and epithelial cells for self-organization, and determine how the coordinated group behavior benefits the whole population. More specifically, we study swarming behavior of *Pseudomonas aeruginosa* and *Myxococcus xanthus* bacteria, as well as dynamics and micro-mechanics of the epithelial morphogenesis.

In chapter 2, we study swarming behavior of *Pseudomonas aeruginosa*, which is a pathogenic bacterium which can cause skin, gut, eye and lung infection in human body. This bacterium is stiff and rod-shaped cell with average length of approximately 2 microns and the diameter of about 0.5 micron. The wild type strain of bacterium has a single helical flagellum at their pole and several Type IV pili (TFP) attached to their membrane that are thin appendages with a length varying from



0.5 micron to 7 microns (see Fig. 1.1a). Most motile bacteria use either flagella or type IV pili (TFP), but *P. aeruginosa* is one of few bacteria that possess both of these motile appendage types. *P. aeruginosa* TFP or flagella confer multiple motility modes in addition to swarming, including swimming, twitching, crawling, and walking [18, 30, 48]. *P. aeruginosa* requires a functional flagellum to swarm [20]. Both TFP and flagella are important to *P. aeruginosa* biofilm formation [97] and mediate attachment to different surfaces, including eukaryotic epithelial cells [17], but the role of TFP during swarming and biofilm formation is not fully understood. Given that *P. aeruginosa* is among many bacteria that grow as a biofilm during infection, there is a need to understand how TFP-TFP interactions between individual cells during swarming help them coordinate their motion to colonize new surfaces and subsequently transition to stationary biofilms. We present evidence that *P. aeruginosa* promotes physical cell-cell interactions during swarming via their TFPs to control their collective motion and limit individual cell's movement in swarms. Because of the difficulty of specifically identifying the influence and dynamics of TFPs upon swarming cells using a traditional experimental approach, a series of coordinated laboratory and computational experiments were used in [4] to study the physical influence of TFP among groups of *P. aeruginosa* cells. Using simulations, it was shown that prior reports of improved swarming by *P. aeruginosa* TFP-deficient mutants can be caused by TFP-deficient cells displaying increased displacement compared with wild-type cells. This prediction was confirmed by in vitro experiments that were performed in Dr. Shrout's lab which demonstrated that a population of TFP-deficient mutants outcompeted *P. aeruginosa* wild type in coculture experiments in reaching the swarm edge first. The benefit of TFP-mediated collective motion was shown by demonstrating, using combination of model simulations and experiments, that wild-type, but not TFP-deficient, *P. aeruginosa* altered its swarming to avoid high concentrations of the antibiotic carbenicillin. My contribution to this project in-

clude novel model extensions together with model calibration and running predictive simulations which provided basis for the conclusions in [4].

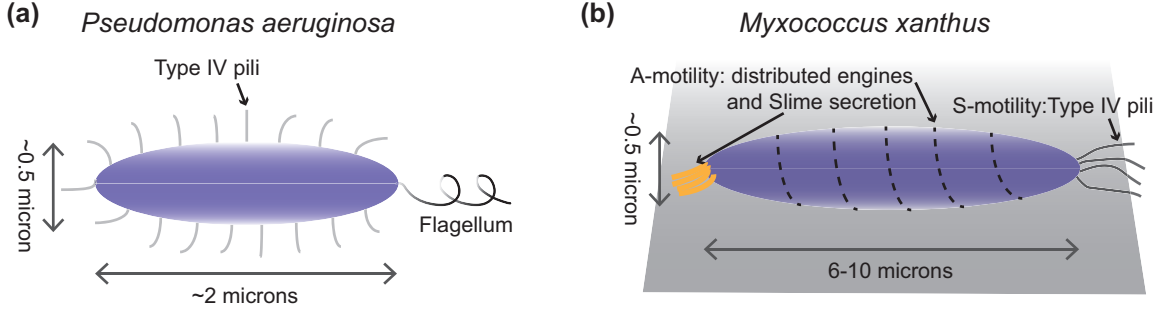


Figure 1.1: Schematic figure of the shape and motility engines of two bacteria that are studied in this thesis: (a): *Pseudomonas aeruginosa*, (b): *Myxococcus xanthus*.

Next, the collective motion exhibited by *Myxococcus xanthus* is studied. *M. xanthus* is a soil bacterium which is among the most social bacteria. This bacterium has a shape of a capsular rod that is about 6-10 microns long and has a diameter of 0.5 micron. *M. xanthus* bacteria move by gliding motility. Gliding motility is traditionally described as a movement in the direction of the long axis of the cell at a solid-liquid, solid-air or an air-liquid interface without the aid of flagella. *M. xanthus* utilizes two genetically distinct motility mechanisms (A-motility and S-motility) to swarm and colonize on a substrate (see Fig. 1.1b). Social (S)-motility facilitates the movement of bacteria as groups, while adventurous (A)-motility enables the individual bacteria to move on their own. Social motility is mediated by the extension and retraction of TFP at the leading pole of the cells, but the mechanism for adventurous motility is not fully understood. Two distinct mechanisms have been proposed to explain the adventurous gliding motility: (i) polar secretion of slime and (ii) an unknown motor that uses cell surface adhesion complexes that form periodic attachments along the cell length. However, experimental studies support the existence of distributed

motility engines along the cell body [122], a hypothesis that we use in setting our computational model (see chapter 3 for more details). It is known that individual *M. xanthus* cells regularly reverse their direction of motion [12] which has an important impact on the swarming expansion rate of the colony [139]. *M. xanthus* can prey and lyse on a variety of other bacteria and grow on the released nutrients [57, 69]. They are also known for their interesting response to nutrient depletion, when a large number (approximately  $10^5$ ) of cells aggregate, reduce their metabolic rate and form fruiting bodies to survive the harsh condition [38]. During both predation and fruiting body formation they exhibit rippling motility behavior where cells self-organize into waves with high and low density regions. While chemical cue signaling known as quorum sensing is well described, swarming bacteria often act and coordinate on time scales that could not be achieved via these extracellular quorum sensing cues.

In chapter 3 of this thesis, cell-cell contact dependent protein exchange is explored as a possible novel mechanism of bacterial self-organization for the social bacterium *Myxococcus xanthus*. It has been observed that certain outer membrane lipoproteins can be transferred from one cell to another by direct contact between cells. This contact-mediated transfer is sufficient to restore function in mutants that are deficient for these specific proteins [62, 64, 95, 111, 112]. Yet a role for protein exchange as a mechanism to stimulate social behavior and collective motion has not been determined. Experimental results on *M. xanthus* protein exchange can be summarized as follows. It is known that cells exchange proteins related to signaling during development of *M. xanthus* fruiting bodies under starvation resulting in some cells differentiating into spores [38, 59, 81, 113, 117]. Also, lipoproteins related to the motility of cells, such as Tgl, CglB, and CglC, can be exchanged to restore gliding motility under nutrient rich conditions [64, 95, 101]. *M. xanthus* cells lacking motility genes are able to acquire these proteins when in contact with cells expressing them and become motile through a process known as stimulation.

As explained in more details in chapter 3, by performing simulations we quantify how quickly outer membrane (OM)-protein could spread throughout the populations of *M. xanthus* bacteria. We compare the ability of wild-type bacteria of spreading protein within population with that for different mutants by varying the parameters that represent physical and behavioral properties of individual cells in the domain close to the swarm edge. The optimal rate of cell-cell connections and efficiency of protein transfer was obtained for reversal periods in the range from 4 to 12 minutes that is the dominant range in experiments. This range has also been reported to optimize the expansion rate of the swarming *M. xanthus* population [139]. This suggests that swarm expansion and the efficiency of the protein spreading could be related to each other. For example, optimized protein exchange and connection rate may result in more efficient motility recovery that enhances the expansion rate of the swarm, or they could be linked to the increase in the orientation correlation between bacteria [139]. However, this remains a very important open question to be investigated in future studies. I am the first author of the recent published paper on these results [3] and developed the model and conducted all predictive simulations on this project.

Collective behavior and self-organization have also been observed for cells in multicellular organisms [55, 105, 131]. The coordinated motion of cells play an important role during the development of tissues as well as in processes such as wound healing and tumorigenesis [43, 85, 90]. In chapter 4, we study the role of cellular physical and mechanical properties in morphogenesis of epithelial tissues by using a combination of experimental observations and detailed biophysical model simulations. Epithelia are tissues composed of tightly packed cells that provide barriers between internal cells of organs and the environment. Epithelium is one of four basic tissue types in the human body [44, 54, 79]. Cell divisions during development must occur robustly, as mis-segregation of chromosomes leads to severe genetic abnormalities in

daughter cells. Over 90% of all human tumors are epithelially-derived [89], and the accumulation of genetic errors during cell division can lead to all of the hallmarks of cancer [56]. In tissues, mitotic cells must become sufficiently round during division to avoid the mis-segregation of chromosomes while still remaining connected with their neighbors [19]. A better understanding of the biophysical mechanisms governing the behavior of mitotic cells in epithelia will result in a better understanding of many diseases including cancer.

Therefore, we developed a sub-cellular biophysical model to study the impact of mechanical interactions between cells in the tissue on the shape and size of cells during division and in general on the tissue patterning. Epithelial cells entering mitosis rapidly undergo structural changes that result in the apical area of the cell becoming larger and rounder, in a process known as mitotic rounding [87, 125]. The beginning of MR in epithelia coincides with an increased polymerization of actomyosin at the cell cortex, which results in an increase in cortical tension and is necessary for MR [107, 124]. Simultaneously, intracellular pressure increases [124], and cells partially reduce adhesion to their neighbors and the substrate [107]. Experiments that can specifically target only dividing cells and measure physical properties of individual cells within tissues are very challenging. Biophysically calibrated computational models can complement current experimental methods by predicting the response of tissue to mechanical perturbations of individual cells. As explained in more details in chapter 4, by performing computer simulations we predict that cytoplasmic pressure is the dominant factor that leads to the increase in the size of cell as it goes to mitotic phase. However, increasing the cortical stiffness, decreasing the cell-cell adhesion during the mitotic phase are crucial for mitotic rounding. Computational modeling environment described in [92] and in this thesis also provides a strong tool to suggest and test the mechanisms of wound healing without leaving scars or disturbing the tissue patterning.

## CHAPTER 2

### ROLE OF TYPE IV PILI INTERACTIONS ON SWARMING BEHAVIOR OF PSEUDOMONAS AERUGINOSA

We study in this chapter how the collective behavior of a colony of *Pseudomonas aeruginosa* bacteria is influenced by the Type IV pili (TFP) interactions between individual cells. TFPs are flexible appendages that are attached to the cell body and have a varying length from 0.5 microns to 7 microns (See Fig. 1.1a). The role these appendages play when not facilitating motility or attachment to surfaces is not yet understood. Due to the small size of temporal and spatial scales of TFP-TFP interactions, it is not possible to investigate the role of TFP interactions by using only the traditional experimental tools. Therefore, we use a combination of biophysical modeling, computer simulations and laboratory experiments to study the swarming behavior at the cellular level and explain the resultant patterns of cells imaged from *in vivo* swarms. The results presented in this chapter are published in [4]. The laboratory experiments are done in collaboration with Joshua Shrout's lab at the department of Civil Engineering and Environmental Sciences, University of Notre Dame.

#### 2.1 Cell based biophysical model

*P. aeruginosa* cells use a single rotating flagellum located at their lagging pole to generate the propulsion force that they need to swim in a liquid environment or swarm within a thin film. A wild type *P. aeruginosa* bacterium has several TFP located on their membrane. The cells are rod-shaped and they do not bend while

interacting with other cells or the environment. Hence, we modeled the cells as rigid self-propelled capsular rods. The length of the cells  $L$  is set to 2 microns and their diameter  $D$  is assumed to be 0.5 microns, as suggested by *in vivo* experimental observations. A schematic figure of the cells is shown in Figure 1.1a. Every cell is self-propelled with a constant velocity  $v_{prop}$  along the direction of the cell axis. The magnitude of self-propulsion velocity is set to  $3 \mu m/sec$  the average velocity of cells from *in vivo* experiments. Wild type cells are assumed to have an external TFP zone with a relaxed length equal to the average length of pili  $L_p$ . As two wild type cells get closer than the set cutoff distance  $r_m$ , the springs become compressed and a repulsion force and torque arises between the cells. The cutoff distance is given by

$$r_m = D + L_p. \quad (2.1)$$

TFP have a polymer structure and show complex behavior under external forces. In our model, we approximate TFP-TFP interaction with a linear force as for a spring, which is based on prior investigation of pili of *E. coli* and *P. aeruginosa*. In particular, Jass et al. [66] studied physical properties of *E. coli* pili by using an optical trapping methodology to measure the force applied by a trapped pilus upon a latex bead. They showed that this force had linear behavior as the pilus was stretched (for the force not being too large to unfold the polymer structure of the pilus). Touhami et al. [128] studied the adhesion forces of *P. aeruginosa* pili using Atomic Force Microscopy. They fastened bacteria to a mica surface through their pili and measured the force applied by pili. They reported that slopes of force curves were nearly linear, but with a little variation for different pilus length. In our model, the magnitude of the linear force is adjusted to slow down cells and rotate them when they are inside the TFP interaction range so that the behavior of cells during collisions resembles to that observed in experiments. This approach has also been applied to modeling

cross-linked liquid crystals [120]. However, in comparison with cross-linked liquid crystals, TFP-TFP interactions are generally more transient. In our model, when

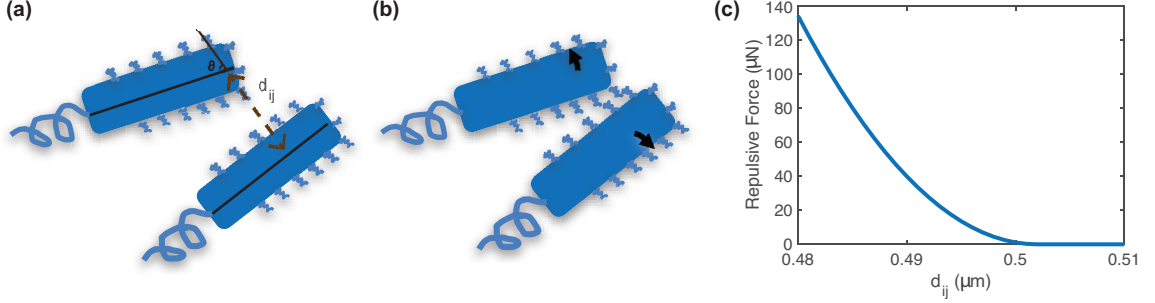


Figure 2.1: (a) Schematic view of criteria used to model interactions of *P. aeruginosa* cells. (b) Hypothesized altering of trajectory between two cells due to torque introduced from TFP effects of two swarming cells. (c) A short-range potential between two cells to avoid overlapping.

the distance between cell  $i$  and cell  $j$  ( $d_{ij}$ ) is less than the cutoff distance  $r_m$  a linear force is used for TFP-TFP interaction and when  $d_{ij}$  is less than the cell diameter  $D$ , a hard-core potential is used to prevent cells from overlapping and for volume exclusion (Figure 2.1c), similar to the approach introduced by Glowinski et al. [52]. This approach has been previously used for modeling rigid spheres. Here we modify the approach to model rigid self-propelled rods representing the *P. aeruginosa* cells. Hence, the spring force ( $\vec{F}_{spring}$ ) and the short-range repulsive force ( $\vec{F}_{repulsive}$ ) are determined as follows:

$$\vec{F}_{spring} = k_{spring}(d_{ij} - r_m) \frac{\vec{d}_{ij}}{d_{ij}}, \quad (2.2)$$

$$\vec{F}_{repulsive} = \frac{c_{ij}}{\epsilon} \left( \left[ \frac{d_{ij} - D - \rho}{\rho} \right]^- \right)^2 \frac{\vec{d}_{ij}}{d_{ij}}, \quad (2.3)$$



where  $c_{ij}$  is the characteristic force,  $\vec{d}_{ij}$  is a vector from cell  $i$  to cell  $j$  of length  $d_{ij}$ , and  $\rho$  and  $\epsilon$  are parameters for defining the range and strength of the repulsive force. The notation  $[a]^- = \max(0, -a)$  is used in Eqn. 2.3. This potential is shown in Figure 2.1c. Due to small size  $L$  of bacteria ( $\approx 10^{-6}m$ ) and their small velocity  $v$  ( $\approx 10^{-6}m/s$ ), the viscous forces dominate the inertial forces and the Reynold's number which is the ratio of inertia to viscosity ( $Re = \rho v L / \mu$ ) becomes a very small number ( $Re \ll 1$ ), where  $\rho \approx 1000 Kg/m^3$  is the density of thin liquid film, and  $\mu \approx 10^{-3} Pa \cdot sec$  is the dynamic viscosity of the liquid. In this regime, we can use the Stoke's equation to describe the motion of bacteria. Hence, the force and torque exerted on the cell  $i$  around its center of mass at each time step is calculated by the following equations [37].

$$\begin{aligned}\vec{f}_i &= \vec{F}_{i,prop} + \sum_j (\vec{F}_{ji,spring} + \vec{F}_{ji,repulsive}) = - \left[ \xi_{\perp} v_{i\perp} \hat{n} + \xi_{\parallel} v_{i\parallel} \hat{t} \right], \\ \vec{\tau}_i &= \vec{l}_i \times (\vec{F}_{i,spring} + \vec{F}_{i,repulsive}),\end{aligned}\tag{2.4}$$

where  $\hat{t}$  and  $\hat{n}$  are the unit vectors parallel and perpendicular to the cell orientation, respectively.  $v_{i\perp}$  and  $v_{i\parallel}$  are the projection of the velocity in the normal and tangent direction to the cell orientation, respectively.  $\vec{l}_i$  is a vector from the center of mass of the cell  $i$  to the point of collision with neighboring cell  $j$ .  $\xi_{\parallel}$  and  $\xi_{\perp}$  are the resistive drag coefficients in parallel and perpendicular direction to the cell's orientation, respectively, and for rod-shaped bacteria are given by

$$\xi_{\parallel} \approx \frac{2\pi\mu}{\log(2L/D) - 1/2}, \quad \xi_{\perp} \approx \frac{4\pi\mu}{\log(2L/D) + 1/2},\tag{2.5}$$

where  $\mu$  is the dynamic viscosity of the thin film [37]. For the rod-shaped bacterium *P. aeruginosa* with aspect ratio  $L/D = 4$ , we have  $\xi_{\perp} \approx 1.63\xi_{\parallel}$ . By obtaining the linear velocity and the angular velocity of each bacterium around its center of mass from Eqn. 2.4, the position of bacteria at time  $t$ , defined by  $\vec{r}(t)$ , and their orientation

$\theta(t)$  are updated in the following way

$$\vec{r}(t) = \vec{r}(t - dt) + \vec{v} \cdot dt, \quad (2.6)$$

$$\theta(t) = \theta(t - dt) \pm \omega \cdot dt. \quad (2.7)$$

Periodic boundary conditions have been used for performing the simulation. The source code that we developed for these simulations is provided in Appendix A.

## 2.2 Results

We examined a potential TFP interaction mechanism among cells using the cell-based computational model (*in silico*) that is described above. The motion and interaction of *P. aeruginosa* was modeled where TFP, distributed uniformly around a cell, affect cell trajectory but not self-propulsion of the cell. The self-propulsion velocity of the cells was set to a constant value equal to the average velocity of cells from *in vivo* observations ( $3\mu\text{m/s}$ ). The model was calibrated using experimental data obtained at different scales for individual *P. aeruginosa* cells and entire *P. aeruginosa* swarms. Simulation experiments were then conducted using this model to study the importance of specific cellular features to collective motion of swarming where we could simulate and track the behavior of every cell over time as well as collective behavior of the population.

Given the observation of our group and others that TFP-deficient *P. aeruginosa* strains (mutants that do not have TFP) exhibit a superswarming phenotype [73, 74, 119], we were interested in explaining the role of TFP during swarming. How do TFP participate during swarming if they do not increase cell motility and are not conferring attachment to surfaces? We studied *P. aeruginosa* wild-type and TFP mutants under conditions where TFP-deficient swarms expand five times faster than

wild-type swarms, despite the fact that these strains produce the same levels of rhamnolipid [119] and show the same swimming (flagellar motility) speed. Rhamnolipids are biochemicals that are released by bacteria due to quorum sensing (assessing the change in population density), and it leads to the extraction of water from substrate which helps them expand the biofilm.

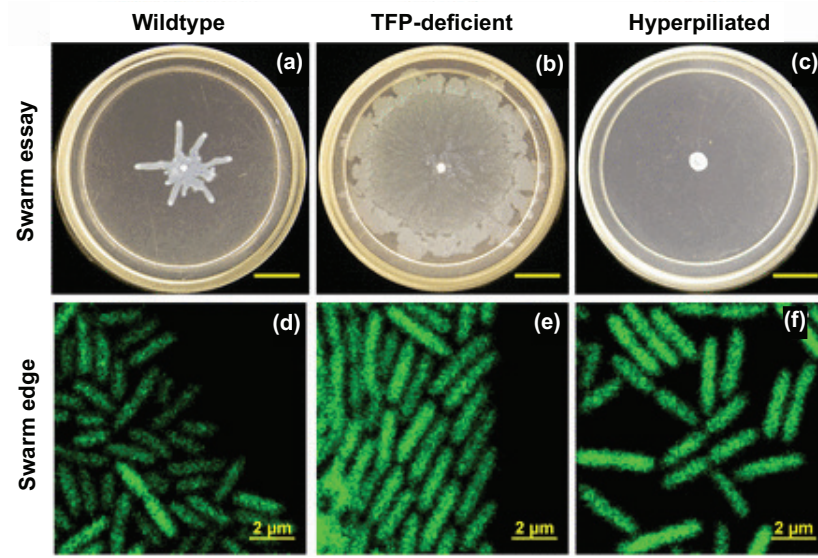


Figure 2.2: Impact of TFP on *P. aeruginosa* swarming. (a-c) Whole population and (d-f) single-cell scales imaged by confocal microscopy during swarming of *P. aeruginosa* wild-type and isogenic  $\Delta pilA$  (TFP-deficient) and  $\Delta pilU$  (hyperpiliated) TFP mutant. The scale bars in a-c and d-f represent 12 mm and 2  $\mu m$ , respectively. Data are adopted from our publication [4].

### 2.2.1 TFP affect cell-cell arrangement during swarming.

We found that the presence of TFP affects the arrangement of cells at the advancing swarm edge (Fig. 2.2). Cells without TFP ( $\Delta pilA$ ) appear more systematically ordered than wild-type cells while hyperpiliated ( $\Delta pilU$ ) cells appear less ordered than wild-type cells. Inspection of cells in swarm tendrils ( $\sim 1-2$  mm toward the

swarm center away from the swarm edge) shows a less-marked distinction between cell-cell patterns for cells with and without TFP.

Alignment of cells was calculated by measuring the parallel orientation of each cell-cell pair both in our simulations and in our *in vivo* experimental observations. The orientation vector for a cell is defined as a vector between two end points of a cell. The alignment correlation coefficient  $C(r)$  for cell pairs was calculated using the following equation [34]:

$$C(r) = \frac{1}{N(r)} \sum_{i,j,i \neq j}^{N(r)} (2 \cos^2(\theta_{ij}) - 1) \quad (2.8)$$

where  $\theta_{ij}$  is the difference between orientation vector angles for the  $i$ th and  $j$ th cells, and  $N(r)$  is the number of pairs of cells separated by a distance  $r$ . An alignment correlation coefficient of 1 indicates that, on average, any two cells that are  $r$  cell lengths apart are perfectly parallel to each other, while a value of 0 indicates that two cells are perfectly perpendicular to each other.

Swarming cells without TFP exhibited the highest alignment values (Fig. 2.3), but the trends of the alignment showed similar behavior across different strains. As expected, cell-cell pairs for all strains tested exhibited the greatest alignment with their closest neighbors (fewer than five cells apart). At greater distances, cell-cell alignment decreases for each different strain until reaching a constant alignment value. Our simulations were able to capture the overall emerging arrangement patterns seen and measured in our swarm plate assays, but the alignment values and the cluster size showed differences with those measured from experiments (Fig. 2.3).

We also quantified cell-cell clustering and population density for swarming cells with and without TFP. We define a cluster as having cells with  $\leq 15^\circ$  difference in orientation and  $\leq 3 \mu m$  separation. The presence of TFP contributed to cluster size, as TFP-deficient cells were the most likely to form larger clusters of 10 or more

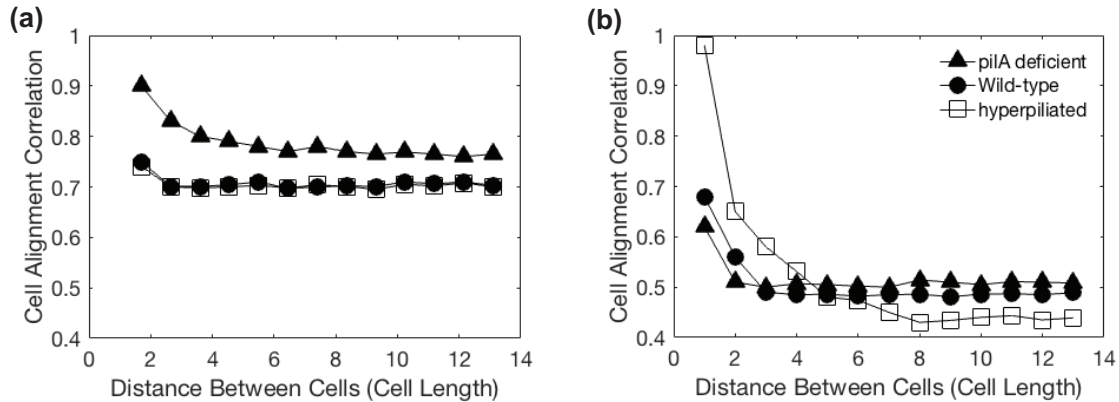


Figure 2.3: Cell-cell alignment for swarm edge cells for wild-type,  $\Delta$ pilA (TFP-deficient), and  $\Delta$ pilU (hyperpilated) swarms. The y axis values of 0-1 represent a measure of alignment where 1.0 = perfectly parallel cells, while 0 = perfectly perpendicular cells. The x axis values represent the number of cell lengths between the compared cells for (a) *in vitro* swarms calculated from images of swarming bacteria at the swarm edge obtained using confocal microscopy (for six images containing 122-715 cells each) and (b) *in silico* computational simulation results of swarming bacteria. Data are adopted from our publication [4].

cells (Fig. 2.4), while hyperpilated cells were more likely to exist as single cells. The majority of cells are not part of a cluster for any strain examined (i.e., cluster size is one cell). With regard to clustering, the simulations partially captured the clustering phenotypes observed *in vitro* (Fig. 2.4). The simulation results did fit the general pattern observed for wild-type cells with TFP; however, the absence of TFP did not lead to the greater cluster sizes observed *in vitro* (Fig. 2.4). Altering the range (or zone) of TFP interaction did not lead to the emerging cell alignment or clustering measured *in vitro*. We also calculated population density as a packing fraction of cells within the available total space (i.e., cell coverage area divided by total swarm area). Higher packing fraction indicates that cells are more tightly packed. TFP-producing wild-type cells exhibited a packing fraction that is 60% of the TFP-deficient  $\Delta$ pilA strain at their swarm edge. Within these high-population swarms, TFP of wild-type cells appear to limit the 2D cell density that can be achieved for *P. aeruginosa*. Overall, the differences in alignment and clustering between these

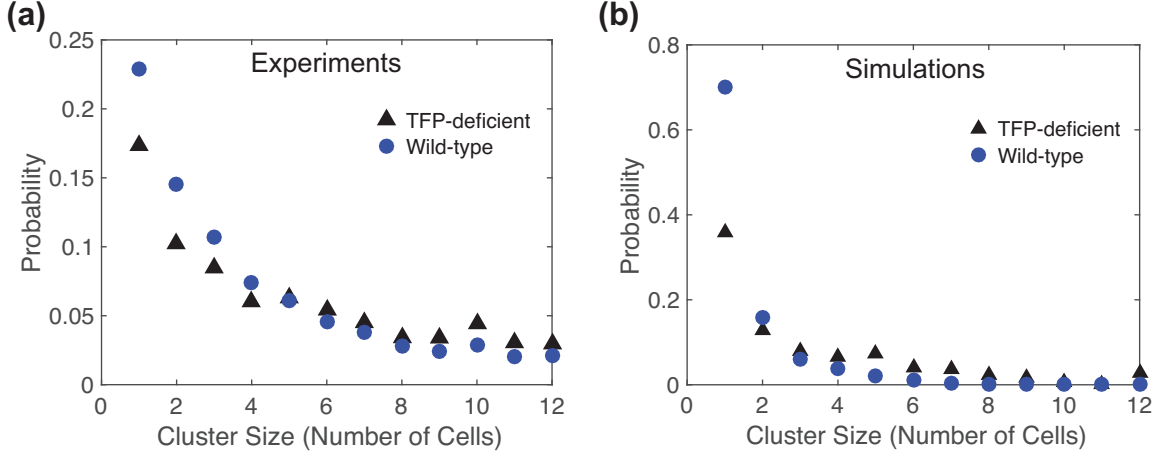


Figure 2.4: Cell clustering during swarming. Cluster size distribution for (a) *in vitro* swarm edge cells ( $n \geq 122$  frames), where TFP-deficient cells are more likely to form large clusters ( $>10$  cells) than wild-type cells at the swarm edge, and (b) *in silico* simulations. Data are adopted from our publication [4].

*in vitro* and *in silico* experiments suggest that these cell-cell arrangement properties are not causative traits for differences in collective motion of bacteria. Hence, if our assumption that TFP impact cell-cell motion is correct, the faster collective motion of TFP-deficient cells must involve cell-cell interactions that promote more than just parallel cell alignment and cluster size to affect swarming. Since few flagellar-motile bacteria also have functional TFP, it is possible that traits of collective motion exhibited by *P. aeruginosa* to swarm are distinct from those of other bacterial species.

### 2.2.2 Simulations of swarming cells predict that TFP affect collective motion.

We further analyzed our *in silico* results to determine how populations with and without TFP might swarm differently. We calculated the mean squared displacement (MSD) over time for simulations of cells with and without TFP, and found that the population of cells exhibited three different types of behavior that can be separated into phases (or regimes) that have been studied for small self-propelled particles: i) ballistic, ii) super-diffusive, and iii) diffusive [32, 63, 106]. The diffusion coefficient  $D$  was measured from the following equation by fitting a linear line to the MSD curve

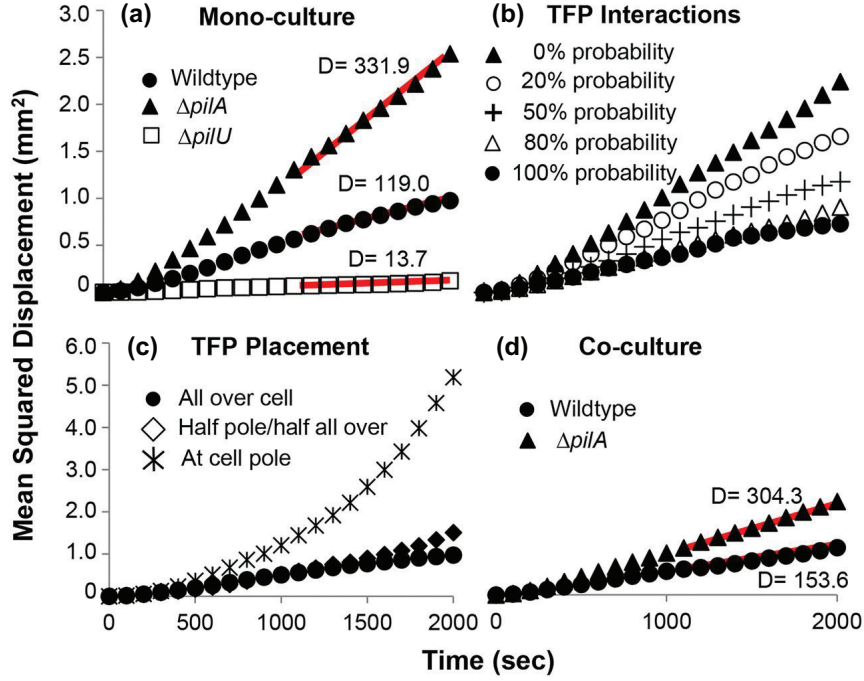


Figure 2.5: Computational simulations of swarming bacteria show MSD of cells over time to be impacted by TFP. The effective cell density of each simulation was kept constant at 75%. (a) Monocultures simulated with differing amounts of TFP. TFP-deficient cells are modeled as having no TFP, whereas wild-type cells have 0.5- $\mu\text{m}$ -long TFP and hyperpiliated cells have 1.0- $\mu\text{m}$ -long TFP. (b) Monoculture of wild-type cells with varied probability of TFP-TFP interaction. (c) Monoculture of cells with varied TFP placement. (d) Coculture simulation of wild-type with TFP-deficient cells that assumes only TFP-TFP interactions and no TFP-cell interactions. The total number of cells in this simulation was 360, and they were randomly assigned to be either TFP deficient or wild type at the onset of the simulation. The diffusion coefficient  $D$  ( $\mu\text{m}^2/\text{s}$ ) for cells in (a) and (d) is measured by linear fit to data within the diffusive phase indicated by the red line. Data are adopted from our publication [4].

in the diffusive regime.

$$MSD = 4Dt \quad (2.9)$$

Diffusion coefficient  $D$  for wild-type cells with TFP was much less than for TFP-deficient cells (Fig. 2.5a). We also implemented TFP-TFP interaction among swarming bacteria in a probabilistic manner to consider the possibility that TFP between neighboring cells may not always interact. Our simulations showed that decreasing

the probability that TFP interact between neighboring cells leads to increased swarm expansion and MSD of these cells (Fig. 2.5b). Thus, our *in silico* results predicted that *P. aeruginosa* cells that have minimal TFP-TFP interaction or cells without TFP should spread more easily (as individual cells) than wild-type cells with considerable TFP interaction at any time during swarm expansion. We also considered the possible placement of TFP on swarming cells by simulating cells with TFP present only at one cell pole. We found that TFP placement also impacts swarm expansion, as cells with more polar TFP exhibited greater swarm expansion and MSD values (Fig. 2.5c). Lastly, we simulated swarming for a mixture of cells with and without TFP and again find that the MSD of cells without TFP is greater than cells with TFP (Fig. 2.5d). We therefore conclude from these *in silico* results that increasing parallel alignment does not improve collective motion a priori; rather, cells within swarms that expand faster tend to exhibit higher alignment. These changes in displacement did not have a linear correlation with alignment or clustering of these cells. Although previous research has postulated that *P. aeruginosa* cells must align with each other to allow swarms to expand in some cases [34, 100], our results suggest alignment as a consequence of swarming behavior rather than a conditional requirement for *P. aeruginosa*. We attributed the higher expansion rates of TFP-deficient strains observed *in vitro* with limiting TFP-TFP interactions between cells within motile populations.

### 2.2.3 TFP interact with other TFP during swarming.

We investigated how differently bacteria with or without TFP spread within swarms by performing simulations of cocultures of *P. aeruginosa* strains with and without TFP. We found that cells with TFP largely interacted with other TFP-producing cells. Swarms composed of a 1:1 ratio of wild-type and TFP-deficient cells exhibit a swarm phenotype that appears between that of wild-type and TFP-



deficient swarms. When TFP-deficient cells were introduced to a population of cells with TFP in a simulation, they were able to move through this population of TFP cells. Conversely, motile cells with TFP moved in clusters and not as single cells. The TFP-deficient cells in these simulations traveled farther and more of these cells reached the swarm edge than wild-type cells (Fig. 2.6). Thus, we explain the reduced spreading rate of wild-type compared with TFP-deficient cells as caused by TFP interacting primarily, if not solely, with other TFP during swarming. The ability of TFP-deficient cells to pass through wild-type (TFP-joined) cell clusters was then observed experimentally when inspecting swarming cells for a few seconds roughly 10 hours after inoculation. We found that wild-type cells remained associated with each other while TFP-deficient cells moved past wild type to reach the swarm edge in a manner similar to that predicted in our computational simulations.

Swarms composed of a 1:10 ratio of  $\Delta pilA$  cells and wild-type cells exhibit an

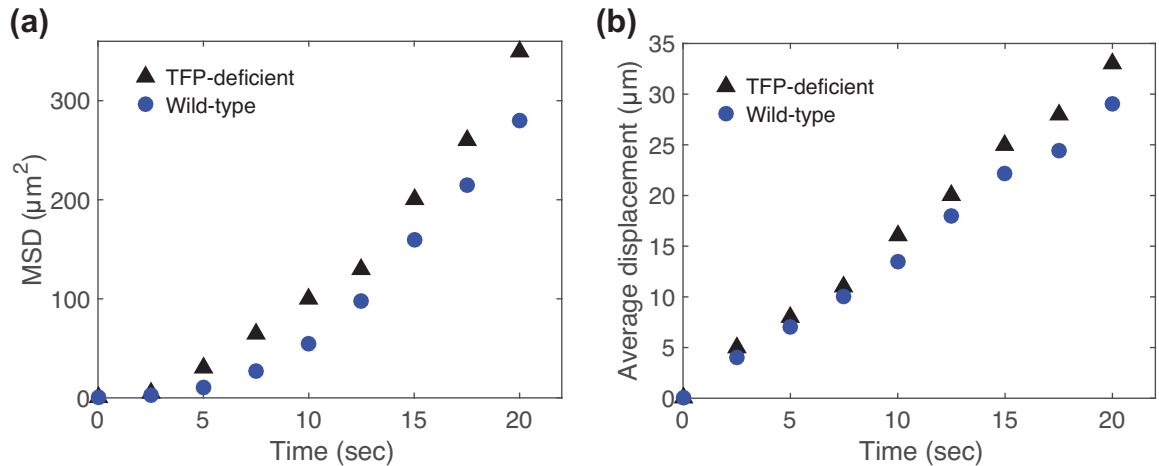


Figure 2.6: Mean squared displacement (a) and average displacement compared between TF-deficient cells and wild-type (b). The population is a 1:1 mixture of wild-type and TFP-deficient bacteria. Data are adopted from our publication [4].

overall pattern that is similar to the wild type alone. However, inspection of single cells within these coculture swarms shows that these strains are not uniformly distributed. At either inoculation ratio, coculture swarm edges become dominated by TFP-deficient cells, while swarm centers are almost exclusively populated by wild-type cells. When wild-type and TFP-deficient cells are present in roughly equal numbers, TFP-deficient cells concentrate on top of the wild-type cells. In all dimensions, interaction between cells with and without TFP appears limited. Overall, TFP-deficient cells advance more rapidly than wild type when growing in coculture (Fig. 2.7). Further, we find these differences in swarm expansion are general for mixing any two strains with differing levels of TFP. For pairwise mixtures of TFP-deficient, wild-type, and hyperpilated strains examined *in vitro*, the  $\Delta pilA$  TFP-deficient strain always expands the fastest, the wild type has the next highest expansion rate, and the  $\Delta pilU$  hyperpilated strain has the slowest swarm expansion rate. This consistent separation between cell types suggests that TFP are important to interactions among *P. aeruginosa* cells during swarming. In coculture these TFP-deficient cells exhibit a higher diffusivity than their TFP-producing counterparts. Because wild-type cells do not cluster with TFP-deficient cells to improve their spreading, we conclude that wild-type cells display strong associations by using their TFP, thus excluding the TFP-deficient cells.

Lastly, we demonstrated a benefit of TFP during swarming by monitoring growth of the wild-type and TFP-deficient strains in the presence of a toxic agent. In plate assays where we spotted a solution containing the  $\beta$ -lactam antibiotic carbenicillin, we observed that wild-type cells avoid this region of the plate (Fig. 2.8). Similar results showing *P. aeruginosa* swarms avoiding various inhibitory compounds have been shown in other studies [10, 77]. Conversely, the TFP-deficient  $\Delta pilA$  mutant swarmed at its higher expansion rate and proceeded into the region containing the highest amounts of antibiotic. Within the timeframe of the experiment ( $\sim 19$

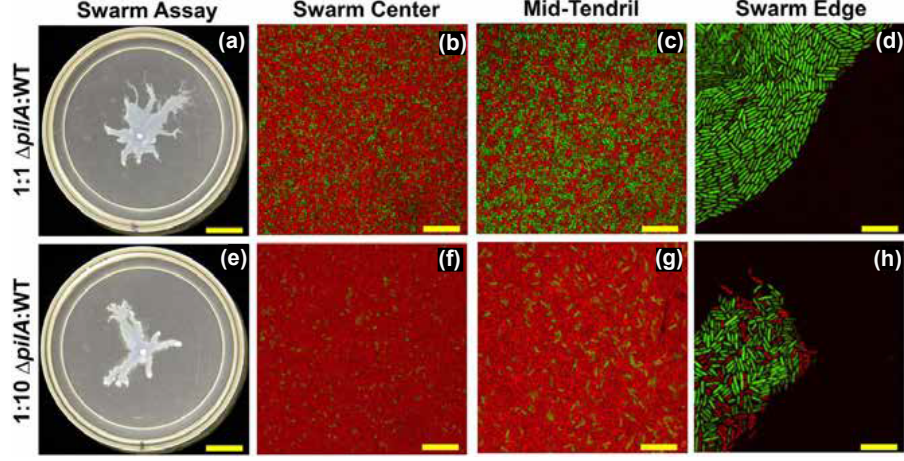


Figure 2.7: Wild-type (WT) cells (red) do not prevent expansion of TFP-deficient ( $\Delta pilA$ ) (green) cells in coculture swarms. TFP-deficient cells do not colocalize with WT over time and are most prevalent at the edges of cocultured swarms, while WT cells dominate the swarm center. This phenotype is observed at inoculation ratios of either (a-d) 1:1 or (e-h) 1:10  $\Delta pilA$ :WT. The scale bars for (a) and (e) represent 10 mm, and the scale bars for (b-d) and (f-h) represent 2  $\mu m$ . Data are adopted from our publication [4].

h), viability staining showed many of these cells stain "dead" by propidium iodide. However, the uncontrolled TFP-deficient cells exhibited amplified signs of their exposure to carbenicillin for much of its swarm area. The TFP-deficient swarms showed cell elongation and cell death well away from their advancing swarm edge. Hence, the TFP-TFP associations that reduced overall swarming allowed *P. aeruginosa* cell groups to deviate their overall swarming direction to avoid a toxic environment.

### 2.3 Discussion

We conclude that *P. aeruginosa* TFP preferentially interact with TFP of other cells during swarming to promote cell-cell association and limit lone cell movement in expanding swarms. We reached this conclusion by studying swarming of *P. aeruginosa* wild-type and TFP-mutant strains using computational simulation (*in silico*) experiments and *in vitro* plate assay swarming experiments in an iterative fashion. We first detailed differences in cell-cell patterning during swarming for cells with

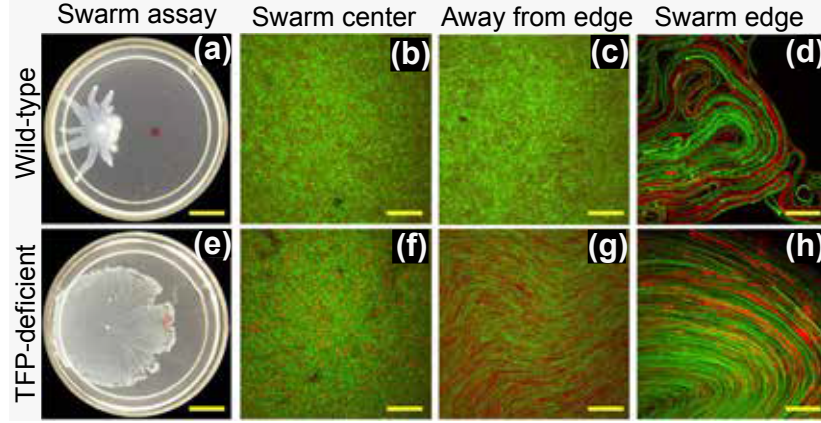


Figure 2.8: TFP limit expansion to allow for avoiding toxic environments during swarming. (a) *P. aeruginosa* wild type avoids a spot inoculation of  $63 \mu\text{g}$  carbenicillin (marked by red dot). (e) The isogenic  $\Delta\text{pilA}$  (TFP-deficient) strain swarms over the carbenicillin. (b-d and f-h) Single-cell scale of swarms imaged by confocal microscopy. Cell elongation and cell death (i.e., stained red with propidium iodide) is apparent in maximum-intensity projections of confocal micrographs at the edges for both (d) wild type and (h)  $\Delta\text{pilA}$ . The impact of carbenicillin is more widespread for the (g)  $\Delta\text{pilA}$ , as exemplified  $\sim 25$  mm from its swarm edge, compared with (c) wild type  $\sim 4$  mm from the swarm edge. The scale bars for (a) and (e) represent 10 mm, and the scale bars for (b-d) and (f-h) represent  $2 \mu\text{m}$ . Data are adopted from our publication [4].

and without TFP from *in vitro* experiments (Fig. 2.2). We then explored potential mechanism of TFP interactions between cells using a cell-based computational model to simulate *P. aeruginosa* swarming. Our simulation results predicted that displacement properties of single cells should be affected by TFP. Additional simulations predicted that mixtures of cells with and without TFP should separate. We confirmed the *in silico* predictions of displacement and separation behavior by showing *in vitro* that TFP-deficient cells will predominate at swarm edges in coculture swarm experiments, even when added 1:10 with a wild-type strain harboring more TFP (Fig. 2.7). Not only did the TFP-deficient ( $\Delta\text{pilA}$ ) strain spread faster during swarming, but this strain also consistently separated from the TFP-producing wild type. Thus, we infer that TFP-TFP interactions between *P. aeruginosa* cells are a dominant mechanism of cell-cell interaction during swarming. This mechanism was

general for *P. aeruginosa* strains with differing TFP levels, as groups of strains with more TFP could always be distinguished from strains with fewer (or no) TFP over time in our experiments. The TFP-TFP interactions we report help explain previous experimental results that showed increased swarming of TFP-deficient mutant strains [73, 74, 119] even though the (uninhibited) swim motility of these strains is the same. Effectively, wild-type *P. aeruginosa* limit their collective motion because of TFP interactions. The importance of TFP associations for *P. aeruginosa* communities for development of static biofilms is well established [7, 70, 71]. Here we further extend our knowledge of TFP function by demonstrating that TFP allow swarming *P. aeruginosa* some directional control of its collective motion. The direct advantage of this TFP mechanism during swarming was evidenced when swarms are monitored in the presence of the antibiotic carbenicillin. A TFP-deficient strain was unable to alter its radial swarming direction and traveled into a toxic environment that led to cell death (Fig. 2.8). TFP-intact wild-type cells were able to stop swarming in the direction of this soluble toxic compound, thus promoting their survival. Based upon our *in silico* and *in vitro* results, we conclude that the TFP influence upon collective behavior we report is passive and does not require extension and retraction of TFP. Our simulations were able to capture the results we observed *in vitro* when we assumed a high interaction probability between cells with uniformly distributed TFP. These results are also consistent with a nonretraction TFP mechanism, as *P. aeruginosa* cells displaying TFP-mediated motility are reported to have polar TFP [27, 121]. The duration of the TFP-TFP/cell-cell associations we report remains to be determined. TFP associations as a precursor to biofilm formation have been observed for *Vibrio cholerae* [68]. Here, *P. aeruginosa* may be using TFP as a means of sensing physical proximity to neighbor cells in addition to sensing population density via diffusible quorum sensing cues. Such a mechanism is in agreement with evidence showing swarming as a transition step between initial surface colonization and static

biofilm development [7, 18, 68, 73, 119]. Further evidence for this transitional role for swarming was provided by van Ditmarsch et al., who demonstrated that selection for hyperswarming *P. aeruginosa* mutations comes at a fitness cost, as these mutants were at a disadvantage in other phenotypic assays [129]. Importantly, none of the hyperswarming mutants obtained by van Ditmarsch et al. were TFP deficient. Evolving to curtail TFP synthesis must come at a cost even for swarming *P. aeruginosa* even in the absence of an antagonist, as we have demonstrated in our experiments. We suggest that this can be explained by the ability of TFP to confer advantageous cell-cell associations by linking to other TFP.

## CHAPTER 3

### REVERSALS AND COLLISIONS PROMOTE PROTEIN SPREADING IN BACTERIAL SWARMS

In this chapter, we use a biologically calibrated computational model to study the mechanism that is utilized by a colony of swarming bacteria to efficiently spread the protein within the population. This work is mainly computational and is accepted for publication in the journal of *Physical Review E* [2].

Swarming groups of bacteria coordinate their behavior by self-organizing as a population to move over surfaces in search of nutrients and optimal niches for colonization. Many open questions remain about the cues used by swarming bacteria to achieve this self-organization. While chemical cue signaling known as quorum sensing is well described, swarming bacteria often act and coordinate on time scales that could not be achieved via these extracellular quorum sensing cues [132]. In this chapter, cell-cell contact-mediated exchange of protein is explored as a possible novel mechanism of bacterial self-organization using well-known social bacterium *Myxococcus xanthus* as an example. Spreading of protein within a bacterial colony can be compared to people at a party randomly exchanging information with one another in a small group, then moving on to another small group. How long it will take to inform everyone depends on the population structure, its density, and the specific strategy of the information exchange. Here, we used Shannon entropy [116] to evaluate the dynamics of protein spreading in the population of bacteria. This approach can be applied for investigating the impact of any molecular exchange between cells that make transient contact with each other. The Shannon entropy has been pre-

viously used for studying, among others, diversity of species [110], diversity in the bacterial and archaeal DNA [60], collective motion of moving animal groups [23, 84] and interacting non-conservative units such as bubbles in a foam [11].

Myxobacteria are common soil bacteria that are among the most “social” bacteria in nature [38, 140]. *M. xanthus* is the most studied of the myxobacteria which was extensively used to explore collective behavior. It is known that individual *M. xanthus* cells regularly reverse their direction of motion [12] which has an important impact on the swarming expansion rate of the colony [139]. It has been observed that certain outer membrane lipoproteins can be transferred from one cell to another by direct contact between cells. This contact-mediated transfer is sufficient to restore function in mutants that are deficient for these specific proteins [62, 64, 95, 111, 112]. Yet a role for protein exchange as a mechanism to stimulate social behavior and collective motion has not been determined.

It is known that cells exchange proteins related to signaling during development of *M. xanthus* fruiting bodies under starvation resulting in some cells differentiating into spores [38, 81, 113, 117]. Also, lipoproteins related to the motility of cells, such as Tgl, CglB, and CglC, can be exchanged to restore gliding motility under nutrient rich conditions [64, 95, 101]. *M. xanthus* cells lacking motility genes are able to acquire these proteins when in contact with cells expressing them and become motile through a process known as stimulation. At least one of the cells (donor, recipient or even another cell that is not directly involved in the outer membrane protein exchange) must be motile to facilitate the transfer [61, 132]. Outer membrane exchange can also enable predation [9, 39, 141] and repair of damaged or deficient cell outer membranes [130]. It has been shown that *M. xanthus* cells with different levels of outer membrane protein that come into direct contact, efficiently share an equal amount of outer membrane material within a relatively short period of time [22, 36, 95, 101, 134].

While the physical properties of *M. xanthus* have been partially characterized



in experiments [102, 138], *in vivo* modification of flexibility or adhesion strength in a deliberate and controlled way in mutants can not be easily done at this time. Changing parameters in computer simulations provides one with a fast and efficient way of producing and testing different hypotheses. Computational modeling of *M. xanthus* swarming and collective behavior has previously focused on the emergence of cell clusters and patterns within a bacterial population [6, 103, 104, 136]. Here, we study how flexibility, adhesivity and reversals of *M. xanthus* bacteria could optimize formation of cell-cell connections within a swarming population and the speed of protein spreading within the population. To achieve this, we extended the Sub-Cellular Element (SCE) model of bacterial swarming [58] by incorporating a novel submodel representing mechanism of protein transfer between contacting cells. The model parameters are calibrated using experimental observations. In order to perform simulations involving large number of cells, a Graphical Processing Unit (GPU) implementation of the SCE model has been developed.

### 3.1 Biologically calibrated computational model

The SCE method has been introduced to study multi-cellular systems [93], and used for simulating epithelial cell growth [29], platelets in blood flow [127], and gliding bacteria [58]. In this approach cells are represented as a collection of interconnected subcellular elements. The dynamics of each SCE results from the elastic forces in response to changes in cell shape or cell-cell and cell-environment interactions. The SCE model of bacterial swarming developed in [58] takes into account adhesive forces between cells and the substrate they move on as well as the flexibility of individual cells and frequency of reversals. The inclusion of adhesion and reversal periods in this computational model sets this approach apart from previous studies [6, 103, 136, 141].

The model that is presented in this chapter is set for studying the A+S- *M. xanthus* mutants. The A+S- mutants only utilize the A-(Adventurous) motility engine

that enables them to move on their own on the surface, but lack the S- (Social) motility engine that works by cells attaching their type IV pili to the neighboring cells and moving together. We model these mutants because it enables us to focus on protein exchange between self-propelled bacteria without interference from the S-motility engine. In the model, cells are represented by 16 interconnected SCEs, and to model the cell motion due to slime A-motility on individual SCEs, distributed force engine is used. Distributed force engine is implemented by applying force to every fourth element of the cells. This allowed for greater flexibility of cells because in highly flexible cells a single lagging force applied to one of the poles can cause flailing motion. The distributed engine model is also amenable to different models of A-motility including focal adhesion. We assume that each cell interacts with the substrate through an adhesive force representing a slime capsule interaction with the substrate. Cells reverse their motion direction by switching which cell pole is identified as the head and tail, thus switching the direction of the forces ( $F_s$ ) applies on the elements. The directional change is controlled by an internal reversal clock assigned to every cell with the fixed reversal period ( $t_r$ ). The reversal clock time increases at every simulation step until it reaches  $t_r$ . Reflecting boundary conditions are implemented in the simulations. Cells in our computational model are assumed, based on experimental observations, to be  $5 \mu m$  in length with an aspect ratio of 10:1. A random noise in the direction of cell movement,  $\mathbf{R}(t) = k_{rand}\boldsymbol{\zeta}$ , is used to model the intrinsic motility fluctuation of bacteria gliding on agar.  $\boldsymbol{\zeta}$  is a normally distributed random vector. Because these bacteria glide in a highly viscous slime, we can make the simplifying assumption that inertia effects can be neglected, resulting in the following form of the equation of motion

$$\frac{d}{dt}\mathbf{x}(t) = \frac{1}{\gamma}(\mathbf{R}(t) - \nabla U(\mathbf{x}(t))). \quad (3.1)$$

The second term on the left hand side accounts for the forces due to the interactions

that are applied on each SCE. The force acting on SCE  $i$  can be described by

$$-\nabla_x U(\mathbf{x}_i(t)) = \mathbf{F}(\mathbf{x}(t)) = \mathbf{F}_{\text{bond}} + \mathbf{F}_{\text{bend}} + \mathbf{F}_{\text{LJ}} + \mathbf{F}_{\text{slime}} \quad (3.2)$$

where

$$\mathbf{F}_{\text{bond}} = \sum_{j \in \text{bonded neighbor}} k_b (||\mathbf{x}_i - \mathbf{x}_j|| - x_{eq}) \hat{\mathbf{r}}_i, \quad (3.3)$$

and

$$\mathbf{F}_{\text{LJ}} = \sum_{j \in \text{non-bonded SCE}} \epsilon \left( 12 \frac{\lambda_{ij}^{12}}{||\mathbf{x}_i - \mathbf{x}_j||^{13}} - 6 \frac{\lambda_{ij}^6}{||\mathbf{x}_i - \mathbf{x}_j||^7} \right) \hat{\mathbf{r}}_i. \quad (3.4)$$

The sum in Eq. 3.3 is over all bonded neighboring SCEs (i.e. neighboring SCEs that belong to one cell). All SCEs have two bonded neighbors except for the SCEs at the ends of the string representing a cell, which only have one. The list of “non-bonded SCE” in the sum of Eq. 3.4 includes all SCEs that belong to other cells and are within the  $LJ_{\text{cutoff}}$  distance of SCE  $i$ . The strength of the non-bonded interaction between the  $i$ th and  $j$ th SCEs of two different cells that are separated by the distance  $x_{ij}$  is defined by the parameter  $\epsilon$ , which represents the strength of the adhesion interaction between slime capsules of the cells. Transition from repulsion to attraction takes place at the distance  $\lambda_{ij}$ . The value of  $\lambda_{ij}$  is chosen based on the known width of bacteria cells and is set to  $0.5\mu m$ .

The interaction due to bending rigidity is defined by the potential:

$$U_{\text{bend}} = \frac{1}{2} k_b (\theta - \theta_{eq})^2, \quad (3.5)$$

where  $k_b$  is the bending rigidity coefficient, and  $\theta_{eq} = \pi$  is the equilibrium angle between three neighboring nodes. Angles between neighboring segments are calculated as follows. For SCEs  $i, j, k$ , where  $i$  is the SCE between  $j$  and  $k$ ,  $\mathbf{r}_1 = \mathbf{x}_j - \mathbf{x}_i = (dx_1, dy_1, dz_1)$  is the vector pointing from  $i$  to  $j$  and  $\mathbf{r}_2 = \mathbf{x}_k - \mathbf{x}_i = (dx_2, dy_2, dz_2)$  is the vector pointing from  $i$  to  $k$ . Three components of the bending force  $\mathbf{F}_{\text{bend}}$  acting

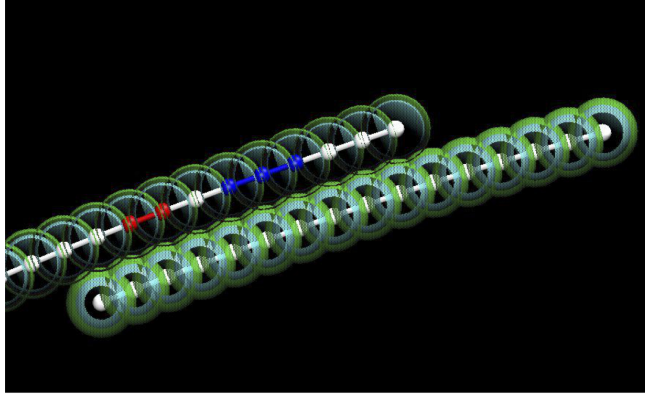


Figure 3.1: Representation of cells with SCEs. White spheres and segments indicate positions and bonds of SCEs. The green (outer) shell represents the boundary for the zone of attraction, the cyan (inner) shell represents the boundary of the repulsive force. (Repulsion and attraction zones are not to exact scale). Red SCEs highlight stretching interactions between SCEs. Blue SCEs represent the bending interaction between SCEs. Figure is adopted from our publication [2].

on the SCEs  $i, j, k$  are as follows

$$F_{i \text{ bend}}^n = a_n + b_n \quad (3.6)$$

$$F_{j \text{ bend}}^n = -a_n \quad (3.7)$$

$$F_{k \text{ bend}}^n = -b_n \quad (3.8)$$

where

$$a_n = \frac{k_b \Delta \theta}{r_1 \sin \theta} \left( \frac{\mathbf{r}_2^n}{\|\mathbf{r}_2\|} - \cos \theta \frac{\mathbf{r}_1^n}{\|\mathbf{r}_1\|} \right) \quad (3.9)$$

$$b_n = \frac{k_b \Delta \theta}{r_2 \sin \theta} \left( \frac{\mathbf{r}_1^n}{\|\mathbf{r}_1\|} - \cos \theta \frac{\mathbf{r}_2^n}{\|\mathbf{r}_2\|} \right). \quad (3.10)$$

Three components refer to the  $x$ ,  $y$ , and  $z$  components of the vectors, so that  $\mathbf{r}_1^1 = dx_1, \mathbf{r}_2^3 = dz_2$ , etc. These expressions are obtained by taking derivative of  $\theta(\mathbf{r}_1, \mathbf{r}_2)$  with respect to  $\mathbf{x}_i$ . The forces acting on all SCEs are then determined and Eq. 3.1 is

integrated using the forward-Euler method

$$x(t+1) = x(t) + \frac{dt}{\gamma}(\mathbf{R}(t) - \mathbf{F}(\mathbf{x}(t))). \quad (3.11)$$

TABLE 3.1:  
DEFAULT VALUES OF THE MODEL PARAMETERS USED IN  
SIMULATIONS

Parameter	Value
Cell width	$0.5 \mu m$
Cell length	$5 \mu m$
Compressibility $k_b$	$148.0 fJ\mu m^{-2}$
Flexibility $k_\theta$	$0.01 fJ$
Friction Coefficient $\gamma$	$1.0e5 nN\mu s\mu m^{-1}$
Cell-cell Adhesion $\epsilon$	$0.01 fJ$
Repulsion Distance $\lambda_{ij}$	$0.5 \mu m$
Adhesion Distance $LJ_{cutoff}$	$0.6 \mu m$
Reversal Period $t_r$	$480 s$
Slime Force $F_s$	$120 pN$
Head Noise $k_{rand}$	$0.1$
Protein Exchange Rate $R_p$	$0.003 sec^{-1}$
Number of cells N	$512$
Size of domain $L_x \times L_y$	$100 \times 100 \mu m^2$

Biologically calibrated model parameters are provided in the Table 3.1. Reversal periods, length and width of bacteria were measured by tracking *M. xanthus* cells in *in vivo* experiments. The dynamic curvature analysis algorithm was used to measure changes in shapes of cells when they collided with each other. A comparison between these measurements for *in vivo* and *in silico* experiments was used in [58] to calibrate the values of different model parameters determining the level of cell rigidity, compressibility, cell-cell and cell-substrate adhesion as well as the magnitude of the

force produced by A-motility engine. The rate of protein exchange is set specifically for motility proteins such as Tgl, CglB and CglC based on reported experimental observations [36, 95, 101, 134].

### 3.2 Evaluation of protein spreading using Shannon entropy

To test how different physical and behavioral properties could affect protein spreading within a population of bacteria, in each simulation the level of protein on cells are initialized from a uniformly random distribution on the interval  $[0, 1]$ . This is done to mimic experiments where cells are tagged with a fluorescent protein, and transfer of this protein is visualized [36, 95, 101, 134]. Experimental observations show that contacting cells share their protein efficiently within few minutes, and the rate of protein exchange  $R_p$  is set accordingly in our simulations. Two cells are said to be connected in our simulations if the smallest distance between their SCEs is less than  $0.6 \mu m$ . This accounts for the diameter of a cell ( $0.5 \mu m$ ) and the slime capsule surrounding the cells ( $0.1 \mu m$ ). An exchange of protein is carried out when two cells are in contact, with a constant rate  $R_p$  from the cell with the higher value to the cell with the lower value. Thus, the average value of protein is assumed to remain constant throughout the simulation, and the distribution of protein converges to the average protein level of the population. Here, we used the concept of Shannon entropy from information theory [116] which provides a measure of unpredictability, to determine the dynamics of mixing and spreading of protein in populations of cells with different physical properties. Our simulations are initialized by randomly distributing  $N$  cells in a two-dimensional (2D) simulation domain of the size  $L_x \times L_y$ . The  $k$ th cell ( $1 \leq k \leq N$ ) is initially assigned a level of protein  $n_k(t = 0) \in [0, 1]$  using a uniformly random distribution. The initial configuration of cells in the domain is shown in Fig. 3.2. For a system of  $N$  cells, the total amount of protein in the population is  $\sum_{k=1}^N n_k \approx N/2$ . The protein distribution is normalized by the total

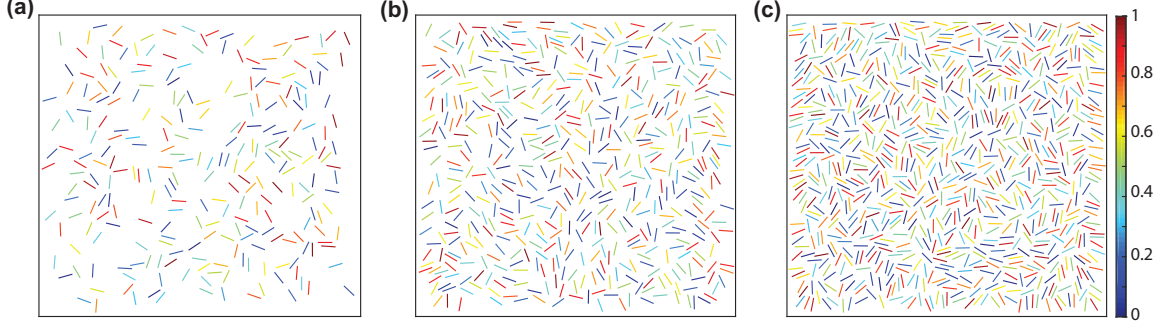


Figure 3.2: Initial cell distributions in simulations of the populations with densities 6.4% (a), 12.8% (b) and 20% (c). The size of simulation domain is set to  $100 \times 100 \mu\text{m}^2$  and the length of cells is  $5 \mu\text{m}$ . The color scale shows the level of the protein on each cell that is chosen randomly from a uniform distribution from  $[0, 1]$ .

amount of protein in the population and is given by

$$\tilde{n}(k, t) = \frac{n_k(t)}{\sum_{k=1}^N n_k} = \frac{2n_k(t)}{N}. \quad (3.12)$$

The entropy of the normalized protein distribution  $\tilde{n}(k, t)$  in a population at time  $t$  is defined as follows

$$I(t) = - \sum_{k=1}^N \tilde{n}(k, t) \log(\tilde{n}(k, t)). \quad (3.13)$$

The time evolution of the normalized protein distribution is shown in Figure 3.3 for a population of 512 cells. The initial value of entropy in a population of  $N$  cells is as follows:

$$I(t=0) = - \sum_{k=1}^N \tilde{n}_k(t=0) \log(\tilde{n}_k(t=0)). \quad (3.14)$$

Cells in model simulations establish physical connections with each other and exchange protein at rates observed in experiments [36]. As a result of protein exchange, the entropy of the system increases with time because mixing of protein in the population increases the uncertainty of knowing which cell has specific level of the protein. Every cell in the population will end up with the same level of protein  $n_k=0.5$  over

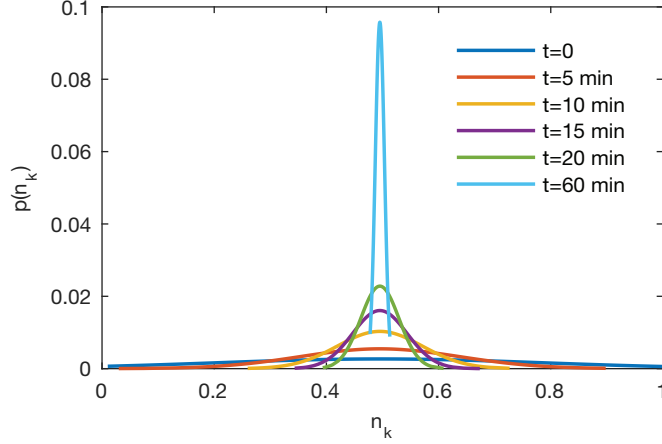


Figure 3.3: Normalized protein distribution at time  $t$ . Initial protein levels of cells are chosen from a uniform random distribution. Over time cells make connections and exchange protein with each other. The level of protein on all cells approaches the same value  $n_k = 0.5$  assuming that enough time is given. Population consists of 512 cells moving inside a 2D simulation domain of the size  $100 \times 100 \mu m^2$ . Data are adopted from our publication [2].

long enough period of time (Fig. 3.3). Therefore, given enough time, the normalized protein distribution of the population approaches the value  $\tilde{n}(k) = 1/N$ . As a result, the entropy of the system will reach its maximum value

$$I(t = \infty) = - \sum_{k=1}^N \frac{1}{N} \log\left(\frac{1}{N}\right) = \log(N). \quad (3.15)$$

Therefore, in a system with  $N$  cells, the normalized entropy change from the start of the simulation (at  $t=0$ ) to time  $t$  is equal to  $\widetilde{\Delta I}(t) = (I(t) - I(0))/E$ . Normalization factor  $E = I(\infty) - I(0)$  is the maximum amount by which the entropy of the system could be increased.

### 3.3 Results

In what follows we identify a range of reversal frequencies and physical properties of *M. xanthus* optimizing the ability of the population to make cell-cell connections



and spread proteins. We test in simulations the effect of varying one parameter while keeping the others constant to their biologically calibrated values (see Table 3.1.)

### 3.3.1 Cell-cell connection rate and duration

Distribution of reversal periods observed in experiments was presented in [139] (see Fig. 3.4). Most of the experimentally observed reversal periods were between 4 and 12 minutes ( $\sim 77\%$ ) with a skew towards shorter reversal periods in that range even though the average reversal period was between 8 and 9 minutes. Very few cells ( $\sim 6\%$ ) reversed in less than four minutes while some ( $\sim 17\%$ ) reversals took more than 12 minutes.

Reversal period  $t_r$  is varied in our simulations from 1 to 30 minutes. The cumulative number of cell-cell connections (without repeated connections) is calculated for each cell and is averaged over all cells in the population at time  $t$ , resulting in the average number of cell-cell connections. The rate of cell-cell connections  $R_c$  is calculated using linear fit to the average number of cell-cell connections as a function of time. The average connection duration  $\tau = \sum_{ev=1}^{N_{tot}} w(ev)D(ev)$  is calculated for  $N_{tot} = 10^4$  collision events, where  $w(ev)$  is the weight for each event (the number of occurrences divided by  $N_{tot}$ ).  $D(ev)$  is the duration of each event. Simulations showed that populations with reversal frequencies in the experimental range had a maximal rate of cell-cell connections (Fig. 3.4). For example, population of cells that reversed with a period from the experimentally observed range of 4 to 12 minutes made connections with the rate  $R_c = 0.65 \pm 0.01 \text{ min}^{-1}$  which was 14% more than  $R_c$  of the population of cells reversing every minute and 41% more than  $R_c$  for the population of cells that did not reverse at all. Figure 3.5a shows the average number of cell-cell connections over  $t$  min for different reversal periods. The results showed very similar behavior for all the reversal periods within the range from 4 to 12 minutes. Therefore, we only show the results for the end points of this range in

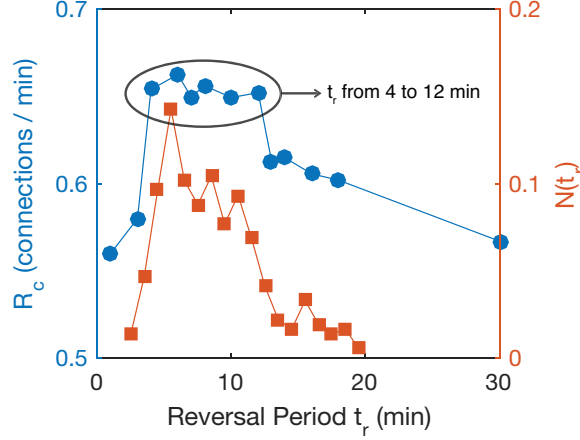


Figure 3.4: Dependence of rate of cell-cell connections  $R_c$  on reversal periods. Solid circles represent  $R_c$  for populations in simulations with different reversal periods.  $R_c$  for the population of non-reversing cells was measured to be of the order of 0.46 connections/min. The filling fraction in the simulations was set at 12.8% close to the average fraction observed in experiments at the swarm edge. Solid squares display the distribution of reversal periods within a population of bacteria in an experiment (adopted from [139]).

the Figures 3.5a-b.

Our simulations also predict (see Figure 3.5) that, as the reversal period  $t_r$  increases, two important transitions occur between the following three different phases: i) non-motile state, ii) effective swarming state, and iii) jammed state. Namely, increasing the reversal period from a very low value ( $t_r=1\text{min}$ ) to the values in the experimentally observed range ( $t_r$  from 4 to 12 min) results in increased ability of bacteria to effectively move in one direction which results in an increased rate of cell-cell connections  $R_c$ . Further increase of  $t_r$  above the experimental range causes the formation of traffic jams and reduces  $R_c$  since the bacteria that are stuck in traffic jams can not explore the domain efficiently and make new cell-cell connections. A qualitative evidence to support this hypothesis is given in the snapshot of the simulations in Figure 3.6B. The phase transition as a result of varying filling fraction has been previously studied for a population of self-propelled rod-shaped bacteria with

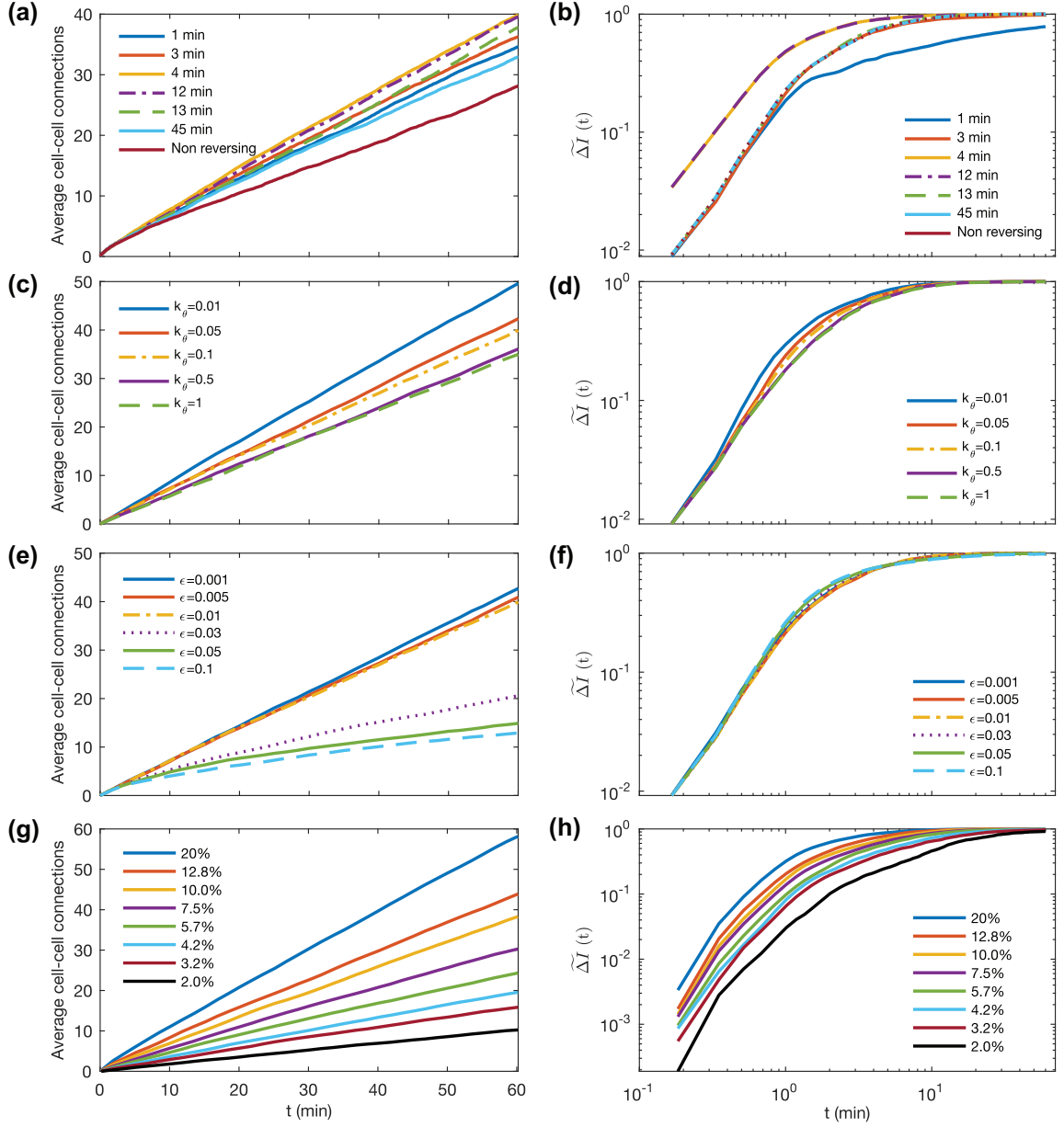


Figure 3.5: a), c), e), g) Dependence of average number of cell-cell connections on reversal frequency, flexibility, adhesion and filling fraction, respectively. b), d), f), h) Change of the normalized Shannon entropy  $\widetilde{\Delta I}(t)$  characterizing distribution of protein over time in bacterial populations with different reversal frequencies, cell flexibilities, cell-cell adhesions and filling fraction, respectively. Data are adopted from our publication [2].

directional reversals [135].

Model simulations also showed that experimentally observed levels of cell flexibility maximized the rate of cell-cell connections and spread of protein in the population. Cell rigidity was varied from the high level (corresponding to the bending rigidity constant  $k_\theta = 1 \text{ fJ}^1$ ) to the very low level (with  $k_\theta = 0.01 \text{ fJ}$ ). The values of the bending rigidity less than this range ( $k_\theta < 0.01 \text{ fJ}$ ) caused cells in the simulations to bend to the extent that they started forming loops and knots. We consider this as a non-biological behavior since cells have not been observed to form loops and knots in the experiments. Using the values higher than this range would not change the rigidity of cells any further (see [58] for details on model calibration). Figure 3.5c demonstrates that cells with the experimentally calibrated value of flexibility parameter ( $k_\theta=0.01 \text{ fJ}$ ) have a connection rate that is 42% bigger than that for rigid cells ( $k_\theta=1 \text{ fJ}$ ). This occurs because more flexible cells have slightly higher collision cross-section due to bending and they explore space more efficiently than rigid cells, resulting in the increased rate of cell-cell connections. Furthermore, the direction of motion of more flexible cells can be perturbed (as a result of interaction with the environment) more easily due to less cost of energy. Once a cell that is adhered to a cluster of cells experiences this change in the direction of motion, it can split from the cluster and travel until it reaches to another cluster and start making new connections. Variation of the bending rigidity parameter  $k_\theta$  was shown to have a negligible impact on the average connection duration (Fig. 3.6c) and clustering behavior (Fig. 3.6d).

Next, the impact of cell-cell adhesion on the connection rate was investigated. Adhesion force between two contacting cells comes from the interaction between capsular polysaccharide that covers bacterial bodies. Figure 3.5e shows that weaker adhesive interaction between cells (lower  $\epsilon$ ) results in considerably higher connection rate. Cells with the experimentally calibrated value of cell-cell adhesion parameter

---

<sup>1</sup>Femtojoule (fJ), unit of bending or adhesion energy, is equal to  $10^{-15}$  Joules.

( $\epsilon=0.01$  fJ) make connections at the rate that is 15% less than the rate of less adhesive cells (with  $\epsilon=0.001$  fJ) and 2.29 times the connection rate of more adhesive cells (with  $\epsilon=0.1$  fJ). This occurs because strong cell-cell adhesion results in cells holding on to each other more effectively, sequestering them from the rest of the population. We found that with the increase of value of the parameter that controls the strength of cell-cell adhesion from  $\epsilon = 0.01$ fJ to  $\epsilon = 0.03$ fJ the rate of cell-cell connections decreased sharply as a result of significant increase in connection duration (Fig. 3.6e). Namely, duration of a cell-cell connection exceeded the time it took for them to exchange protein efficiently, resulting in reduction of the number of new cell-cell connections.

The average rate of cell-cell connections  $R_c$  was also shown to increase as a result of increasing the population number density defined as the two-dimensional filling fraction (Fig. 3.5g). This happens because bacteria in populations with higher number density (20%) spend considerably less time (approximately 4.4 times less) moving freely before making contact with another cell compared to the cells in a population with number density 2%. Fig. 3.6g demonstrates that varying the filling fraction does not have a significant impact on the duration of connections and that improved efficiency of protein spreading is mainly due to increased rate of cell-cell connections.

### 3.3.2 Evaluation of protein spreading efficiency.

To quantify the efficiency of protein transfer, we used the Shannon entropy as a metric indicating the amount of uncertainty in the level of protein in each cell in the population. The simulations results are represented for different reversal periods (Fig. 3.5b), levels of flexibility (Fig. 3.5d) and adhesion (Fig. 3.5f), while all other parameter values were fixed to their experimentally calibrated values listed in Table 3.1. The entropy of the population eventually approached the same maximum value in

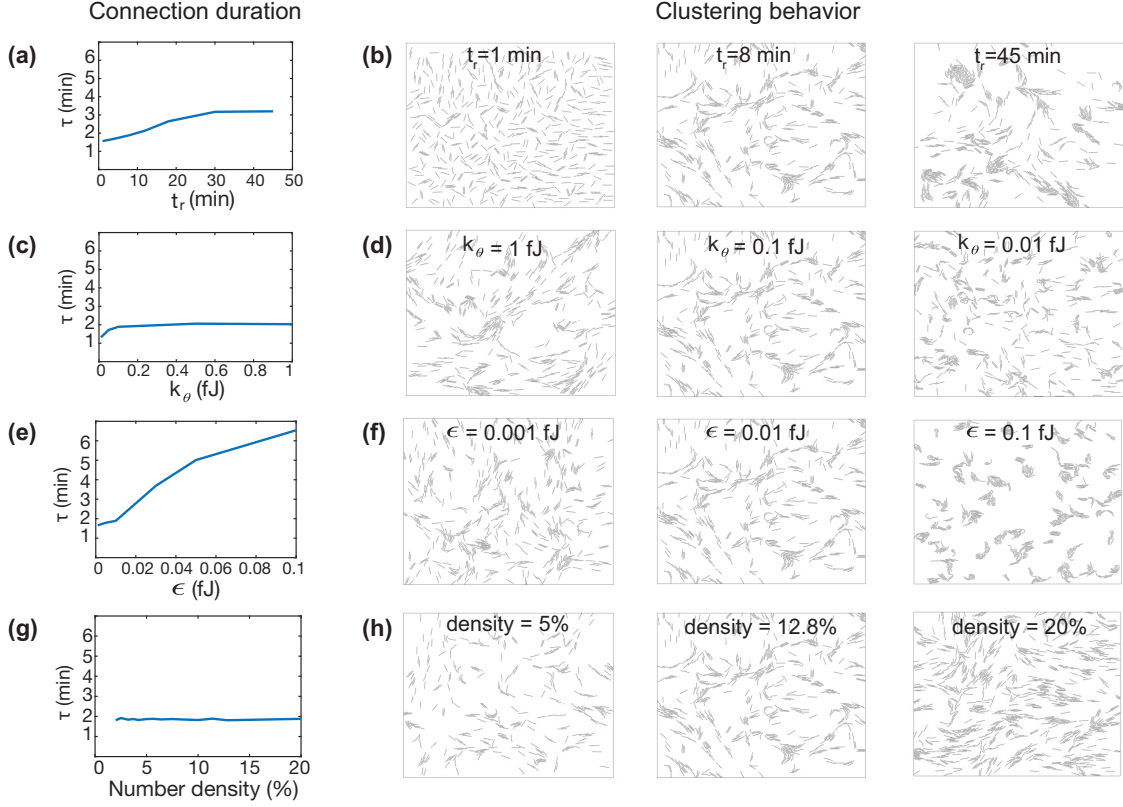


Figure 3.6: a, c, e, g) Average connection duration for different values of reversal period, bending rigidity, adhesion strength, and number density, respectively. b, d, f, h) Clustering behavior for different (low, calibrated with experiments, and high) values of reversal period, bending rigidity, adhesion strength, and number density, respectively. Data are adopted from our publication [2].

all simulations, but over different time intervals. Therefore the time required for a system to reach half the maximum entropy was used as a measure of the efficiency of protein spreading.

The optimal efficiency of protein transfer was obtained for reversal periods in the range observed in experiments from 4 to 12 minutes. In extreme cases of non-reversing cells or cells reversing very frequently, protein spreading efficiency drops dramatically (see Fig. 3.5b). This happens because cells that reverse with periods less than the experimental range move back and forth frequently, hence they are not able to move on the substrate efficiently to make new cell-cell connections and exchange protein with new cells. On the other hand, if cells reverse with periods that are larger than the values of the experimental range, they get stuck in traffic jams which reduces their ability to swarm efficiently, make new cell-cell connections and spread the protein within the population. Our simulation results show that for the population of cells that reverse with periods in the experimentally observed range, the time required to reach half the maximum entropy is 84% less than that for the populations that reverse every minute, and 49% less than that for the population of cells that do not reverse at all.

Figure 3.5d shows that simulations with higher cell flexibility have faster entropy increase in comparison with simulations with more rigid cells. The time it takes the population with experimentally calibrated cell flexibility to reach half the maximum entropy was shown to be 33% less than that for rigid cells ( $k_\theta=1$  fJ). Changing adhesion strength between cells in the range from  $\epsilon = 0.001$  fJ (negligible adhesion force between two neighboring cells) to  $\epsilon = 0.1$  fJ (resulting in cells sticking together after they get connected) did not have a significant impact on the efficiency of protein transfer (Fig. 3.5f), although it was shown to significantly impact the rate of cell-cell connections. As the strength of cell-cell adhesion increases, duration of cell-cell connections increases monotonically and, as a result, stable clusters of cells are

formed (Fig. 3.6f). This suggests existence of a balance between the rate of making cell-cell connections and the duration of the connection between two contacting cells. Relatively short cell-cell connection due to weak cell-cell adhesion leads to a higher rate of cell-cell connections with new cells, but protein can not be exchanged efficiently because of the short connection time.

The efficiency of the protein spreading was also studied for different values of the filling fraction. Figure 3.5h shows that monotonic increase in the filling fraction results in the monotonic increases of the efficiency of the protein spreading. This results from formation of bacterial clusters (Fig. 3.6h) leading to increased rate of cell-cell connections (Fig. 3.5g). The time it takes the population with filling fraction 2% to reach half the maximum entropy is about 5 times bigger than that for the population with filling fraction 20%.

### 3.4 Discussion

Previous studies have demonstrated the important role of cell reversals and physical properties of cells in optimizing the swarming expansion rate of a *M. xanthus* population. We studied in this chapter, by using a detailed biologically calibrated computational model and Shannon entropy, their impact on the rate of cell-cell connections and spread of proteins in the population.

It has been shown experimentally that exchange of outer membrane proteins can be beneficial to the bacterial population in several ways such as rescuing the gliding motility of motility mutants under nutrient-rich conditions [61, 64, 95, 101, 111], predation [9, 39], and genetic repair of damaged cells [130]. It is not currently possible to control flexibility or adhesion strength *in vivo* with an isogenic *M. xanthus* mutant strain. Therefore, a detailed computational model was used to study how quickly outer membrane (OM)-protein could spread throughout the populations of *M. xanthus* A+S- mutants with different physical and behavioral properties of indi-



vidual cells at the swarm edge. Cells at the swarm edge are monolayered, exposed to a maximum level of nutrient and oxygen and behave distinctively compared to the interior cells [31, 139]. The optimal rate of cell-cell connections and efficiency of protein transfer was obtained for reversal periods in the range from 4 to 12 minutes observed in experiments. This range has also been reported to optimize the expansion rate of the swarming *M. xanthus* population [139]. This suggests that swarm expansion and the efficiency of the protein spreading could be related to each other. For example, optimized protein exchange and connection rate may result in more efficient motility recovery that enhances the expansion rate of the swarm, or they could be linked to the increase in the orientation correlation between bacteria [139]. However, this remains a very important open question to be investigated in future studies.

Higher cell-cell connection rates were also obtained for populations with more flexible cells. Tracking cells from *in vivo* experimental movies confirmed cells to be very flexible. Although it was shown that decreasing the strength of cell-cell adhesion considerably increased the rate of cell-cell connections, it had a negligible effect on the protein spreading. Fig. 3.6 shows that this happens because cells in a population with high strength of cell-cell adhesion ( $\epsilon = 0.1$  fJ) on average make connections that last 6.4 minutes, while cells in a population with low strength of cell-cell adhesion ( $\epsilon = 0.001$  fJ) on average stay connected for about 2 minutes. Therefore, although longer connection duration enables two connected cells to efficiently exchange their proteins, the efficiency of the protein spreading at the population level is penalized by reduction of the average rate of cell-cell connections. Consequently, the positive effect of longer connection duration between cells is reduced by the decrease of the average rate of the cell-cell connections. As a result, the efficiency of the protein spreading does not depend significantly on the strength of the cell-cell adhesion.

The rate of collisions between rod-shaped particles such as *M. xanthus* can be

estimated by using analogy with molecular gases as follows:  $r_c = fv\sigma/V$ , where  $f$  is the volume fraction,  $v$  is the average particle speed,  $\sigma$  is the collision cross-section, and  $V$  is the particle volume. In two dimensions  $\sigma \approx L$ , where  $L$  particle length, and  $V \approx dL$ ,  $d$  is particle width. For typical simulation conditions of  $L = 5 \mu\text{m}$ ,  $d = 0.5 \mu\text{m}$ ,  $f = 0.128$ , and  $v = 4.3 \mu\text{m}/\text{min}$ , we obtain the collision rate  $r_c \approx 1.1 \text{ min}^{-1}$ . This value has the same order of magnitude as the experimentally measured connection rate  $R_c$  (see Fig. 3.4). It implies that under the assumption that *M. xanthus* bacteria do not follow slime trails left by other bacteria, the mechanism based on mostly uncorrelated collisions between bacteria is primarily responsible for forming connections and protein spreading.

Figure 3.4 shows a large increase in value of  $R_c$  from  $t_r=3$  minutes to  $t_r=4$  minutes which can be explained as follows. Cells need some minimal time to move in one direction before they reverse, in order to make enough physical connections with different cells in the population to spread protein. The sum of the estimated time that two cells stay in contact ( $2.2 \pm 0.07$  minutes) with the time that is required for a cell to move freely before reaching another cell ( $1.1 \pm 0.05$  minutes) is approximately 3.3 minutes which is very close to the time of the sharp increase in the value of  $R_c$  in Fig. 3.4.

Most bacteria grow in a mixed (and potentially hostile) environment. Many bacteria use extracellular signals via a variety of quorum sensing mechanisms to coordinate actions at the species level. However, the chemical signals for most of these quorum sensing systems are insufficient to coordinate action on time scales that lead to collective motion and swarming on surfaces. Thus the ability to use protein cues to coordinate collective actions is very appealing. In this work, we have demonstrated that experimentally observed physical properties and multicellular behavior of *M. xanthus* favor population with an efficient spread of protein. Our findings suggest that organisms with accelerated protein spreading should have a

competitive advantage in a swarm environment. Periodic reversals of movement have been reported for several bacterial species besides *M. xanthus* [8, 51, 72, 82]. Therefore, given the importance of reversals for *M. xanthus* swarming and potential mechanism of extracellular signaling that is investigated here, we suggest that more species might utilize periodic reversal strategies to optimize their collective behavior. Furthermore, our findings suggest that predesigned motion reversal can be employed to enhance the collective behavior of biological synthetic active systems. An extension of our computational environment can also provide an efficient platform for studying the phase separation in bacterial colonies [47], and the edge geometry of microbial population [41].

## CHAPTER 4

### COMPUTATIONAL STUDY OF DEVELOPING EPITHELIA

In this chapter we investigate the impact of intercellular mechanical interactions on the mitotic rounding during cell division and on dynamics of tissue morphogenesis, by developing a biologically calibrated computational model. The experiments that are used to calibrate the model parameters and the data analysis are done in collaboration with Professor Jeremiah Zartman’s lab in the Department of Chemical and Biomolecular Engineering at the University of Notre Dame. The work presented in this chapter is being considered for publication in a journal [92]. The first four authors Ali Nematbakhsh, Wenzhao Sun, Pavel Brodskiy and Aboutaleb Amiri have made equal contributions to this work. Wenzhao Sun started the development of the basic structure of the simulation code. Ali Nematbakhsh and Aboutaleb Amiri contributed to the development and extension of the code for studying the development of epithelial tissues of *Drosophila* fruit fly. The experimental data used for calibrating the model were obtained by Cody Narciso with technical assistance from Luis Lazalde at Dr. Zartman’s lab. Aboutaleb Amiri performed the simulations and analyzed the data for quantifying the roundness and size of cells during mitotic rounding. Pavel Brodskiy developed the multiple linear regression analysis, including the the design of experiments, response surface methods and sensitivity analysis described in [92] and in Appendix B of this thesis. All first four authors contributed to discussion of the results, figure generation and writing of the text.

Epithelia are tissues composed of tightly adherent cells (Fig. 4.1a-d) that provide barriers between internal cells of organs and the environment. Epithelial tissues are

one of the four basic tissue types in the human body [44, 54, 79]. Epithelial expansion is driven by cell proliferation during development, but it also occurs in early stages of cancer. Robust and precise cell divisions are crucial during development, as mis-segregation of chromosomes leads to severe genetic abnormalities in daughter cells. It is known that over 90% of all human tumors are epithelially-derived [89], and the accumulation of genetic errors during cell division can lead to all of the hallmarks of cancer [56]. In tissues, mitotic cells must become sufficiently round to avoid the mis-segregation of chromosomes, while still remaining connected with their neighbors [19]. Epithelial cells entering mitosis rapidly undergo structural changes that result in the apical area of the cell becoming larger and rounder, in a process known as mitotic rounding (MR) [87, 125]. Although the precise function of mitotic rounding in different systems remains to be investigated in more details, it is likely that the round shape provides a suitable environment for the spindle<sup>1</sup> to assemble, while also delimiting the space in which microtubules have to search to find the mitotic chromosomes [78]. In addition, by simplifying cell geometry, mitotic rounding might contribute to the accurate partitioning of cellular contents into the two daughter cells. A deeper understanding of the biophysical mechanisms governing the behavior of mitotic cells in epithelia will result in a better understanding of many diseases including cancer.

MR occurs in detached cells, cells adherent to a substrate as well as in epithelial cells within tissues [123, 124]. The beginning of MR in epithelia coincides with an increased polymerization of actomyosin at the cell cortex, which results in an increase in cortical tension and is necessary for MR [107, 124]. Simultaneously, as a result of osmotic swelling the intracellular pressure increases [124], and cells partially reduce adhesion to their neighbors and the substrate [107]. Experiments that can specifically target only dividing cells and measure physical properties of individual cells

---

<sup>1</sup>The spindle helps split the sister chromatides from a parental cell into two daughter cells.

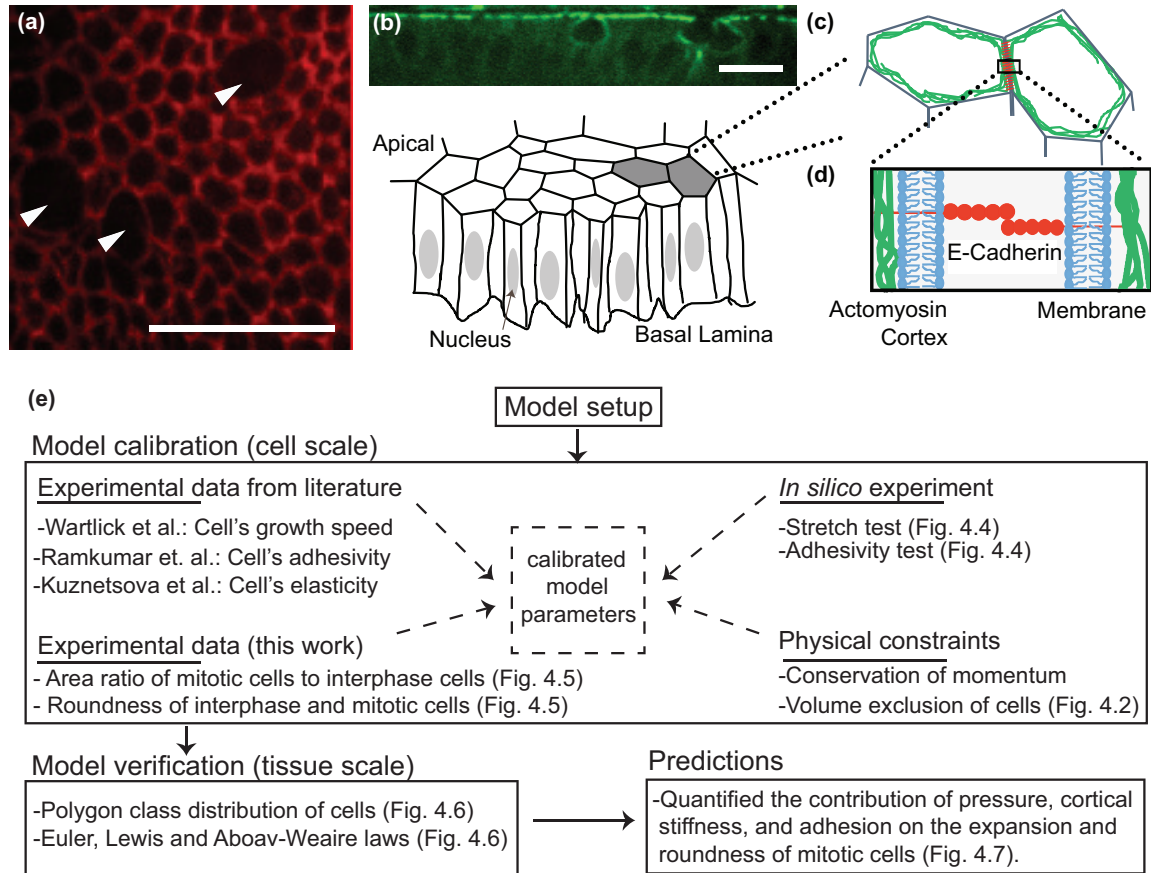


Figure 4.1: (a) Apical surface of epithelial cells within the *Drosophila* wing imaginal disc that are marked by E-cadherin tagged with fluorescent GFP (DE-cadherin::GFP). Multiple cells within the displayed region are undergoing mitotic rounding with a noticeable decrease in fluorescent intensities of E-Cadherin. (b) Experimental image of cross-section of wing disc marking levels of actomyosin (Myosin II::GFP) and cartoon abstraction of epithelial cells, which are polarized with apical and basal sides. Actomyosin and mechanical forces during mitotic rounding are primarily localized near the apical surface. (c) At the molecular scale, the boundary between cells consists of a lipid bilayer membrane for each cell, E-cadherin molecules that bind to each other through homophilic interactions, and adaptor proteins that connect the adhesion complexes to an underlying actomyosin cortex that provides contractile forces along the cell cortex. Arrows indicate mitotic cells. Scale bars are 10 micrometers. (e) Workflow of our computational model.

within tissues are currently impossible. Consequently, computational simulations provide a critical means in which the interplay between multiple physical regulatory mechanisms during the cell division process can be investigated.

Computational modeling coupled with experimentation can provide a powerful tool for investigating the biophysical principles governing organogenesis<sup>2</sup> [14]. Biophysically-derived computational models can complement current experimental methods by predicting the response of tissue to mechanical perturbations of individual cells. Here, MR is investigated by using a novel multi-scale sub-cellular element model (SEM) that simulates epithelial cells in growing tissues. Novel biologically relevant features of the model include: i) detailed representations of cell-cell interactions; ii) a decoupled description of mechanical properties of cells during mitotic rounding; and iii) a systematic calibration of model parameters to provide accurate biological simulations of tissue growth. We performed a sweep study on the model parameters that control the strength of cell-cell adhesion, membrane stiffness, or cytoplasmic pressure during mitotic rounding. Consequently, we analyzed the impacts of such parameter variations on cross-sectional areas of mitotic cells at the apical surface as well as the roundness of mitotic cells right before division.

This chapter is organized as follows (and is also depicted in Fig. 4.1e). The modeling background and model development is first described. Then, the Results section provides details of model calibration of single cell parameters using quantitative biophysical data. The calibrated model predicts emergent properties of epithelial topology. The model is then used to investigate the relative contributions of cell-cell adhesion, membrane stiffness and intracellular pressure in controlling the size and shape of mitotic cells. Finally, we discuss the possible future extensions of the computational model, for studying a variety of different important biological problems including wound healing.

---

<sup>2</sup>The process of organ production during development.

## 4.1 Modeling background

Multiple computational approaches have been used to model the growth of epithelial tissue, each with its particular focus and applications [83]. For example, the cellular Potts modeling (CPM) approach has been used successfully to take into account cell adhesivity to study cell aggregation as well as cell morphogenesis [25, 26]. Finite element models (FEMs) have also been implemented to investigate epithelial cell behavior [15, 142]. Vertex based models (VBM) provided an efficient approach to study the regulation of cell topology, tissue-size regulation, tissue morphogenesis, and the role of cell contractility in determining tissue patterning and shape [40, 42, 96, 108, 109].

In VBMs cells are defined by the several vertices that represent the meeting points of shared cell-cell contacts (as reviewed in [109]). The implementation and comparison of the five popular cell-based modelling approaches for simulating the self-organization of multicellular tissues has been described in [1, 67].

The Subcellular Elements Model (SEM) was initially developed by Newman’s group [126] for simulating multi-cellular systems to encompass multiple length scales. SEMs have been extended to predict how mechanical forces generated by cells are redistributed in a tissue and for studying tissue rheology, and cell-cell signaling. SEM was also used to study the mechanical properties of epithelial cells without making pre-defined assumptions about cell shapes [94]. For example, SEM model was used to compare multiple mechanisms governing the formation of stratified layers of the epidermis [115] as well as mechanisms governing intestinal crypt homeostasis [127]. Each cell in a SEM consists of a set of nodes representing a coarse-grained representation of subcellular components of biological cells. Node-node interactions are represented by potential energy functions. Another SEM developed by Jamali et al. [65] represents the membrane and nucleus of the cell by nodes that are connected by overdamped springs. Gardiner et al. [45] described a SEM with locally-defined



mechanical properties. Christely et al. [29] have developed an efficient computational implementation of the SEM simulating role of Notch signaling in cell growth and division, on GPU cluster to decrease computational time. A particular advantage of the SEM approach is that it can provide local representations of mechanical properties of individual cells which can be directly related to the experimental data [35].

## 4.2 SEM computational model

We developed a multi-scale SEM, to study the development of epithelia with the focus on the two-dimensional (2D) planar cell shapes near the apical surfaces of cells. This is a simplifying approximation that was used in many previous models of wing disc growth [40, 42, 45, 65]. In particular, it is reasonable to use a 2D model for studying many epithelial processes in the *Drosophila* wing disc pouch because it consists of a single layer of cells and the essential structural components of those cells, including E-cadherins and actomyosin, are concentrated on the apical surface of the epithelia (Fig. 4.1c-d). E-cadherin is responsible for adhesion between two neighboring cells, and actomyosin, which is concentrated at the apical surface drives cell contractility. The nucleus and most of the cytoplasm are pushed up to the apical surface during cell division. Using a 2D approximation also allows us to model a large number of cells with high resolution and special attention to mechanical cell properties. Future development of our simulation platform implemented on GPU clusters, will also enable 3D simulations with reasonable computational costs.

In what follows, we first describe different types of the subcellular elements that are used to simulate each cell, and the interactions between them. Then, the equations of motion of each subcellular element are provided. Finally, approaches for modeling cell's growth, transition to mitotic phase, and division are described.

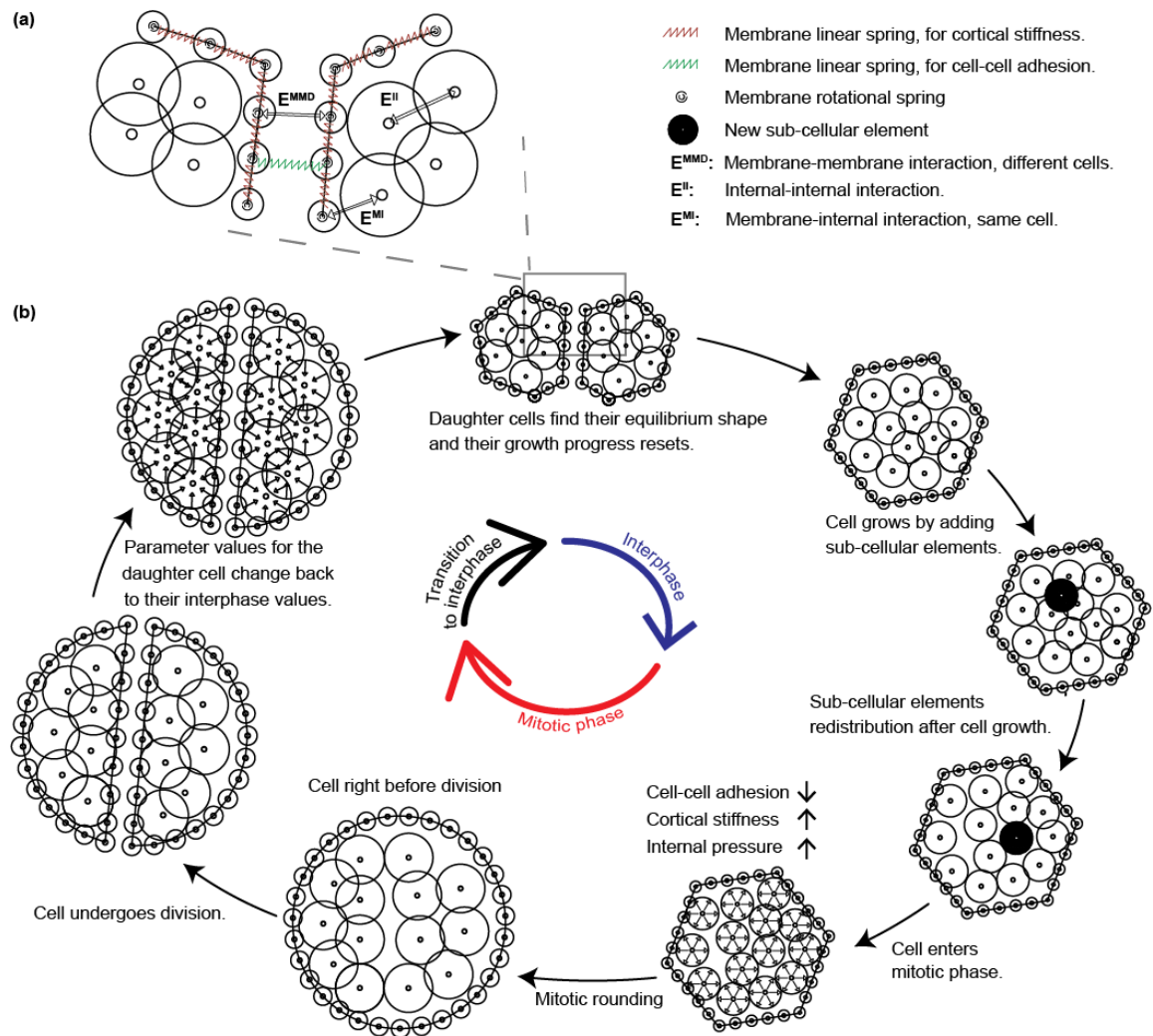


Figure 4.2: Diagram of the underlying physical basis of model simulations. (a) Intra-cellular and intercellular interactions between different elements of the model. Symbols and notations are indicated in the legend. (b) Implementation of the simulation of cell cycle in the model.

#### 4.2.1 Subcellular elements

Individual cells are represented as collections of two types of interacting subcellular elements: internal nodes and membrane nodes (Fig. 4.2a). The internal nodes account for the cytoplasm of the cell, and the membrane nodes represent both plasma membrane and associated contractile actomyosin cortex. The internal and membrane nodes are placed on a 2D plane, representing the apical surface of epithelia.

Interactions between internal and membrane nodes account for the cytoplasmic pressure and are modeled using potential energy functions as depicted in Fig. 4.2a. The internal-internal nodes interactions represent the cytoplasmic materials inside a cell, and the interactions between membrane nodes of the same cell are used to model the cortical stiffness. Cell-cell adhesion is modeled by membrane-membrane nodes interactions between two neighboring cells. A list of all potential functions that are used to model mechanical properties of cells and epithelial tissue and description of their biological relevance are provided in Table 4.1.

TABLE 4.1:  
POTENTIAL ENERGY FUNCTIONS IN THE MODEL

Potential function	Type	Biological concept
Internal-internal nodes ( $E^{II}$ )	Morse	Cytoplasmic materials
Membrane-internal nodes ( $E^{MI}$ )	Morse	Internal pressure
Membrane-membrane nodes of neighboring cells $E^{MMD}$	Morse	Volume exclusion
Membrane-membrane nodes of neighboring cells $E^{adh}$	Linear spring	Cell-cell adhesion
Membrane-membrane nodes of same cell $E^{MMS}$	Linear and torsional springs	Cortical stiffness

Linear and torsional springs are used for modeling interactions  $E_{ik}^{adh}$  and  $E_{ik}^{MMS}$ , while Morse potential functions are used for modeling interactions  $E_{ij}^{MI}$ ,  $E_{ik}^{II}$  and  $E_{ik}^{MMD}$  (Fig. 4.2a). Morse potential consists of two terms, generating short-range repulsive and long-range attractive forces [126]. For example, the Morse potential function between a membrane node  $i$  and an internal node  $j$  of the same cell ( $E_{ij}^{MI}$ ) is described as following:

$$E_{ij}^{MI} = \left[ U^{MI} \exp\left(\frac{\mathbf{x}_i - \mathbf{x}_j}{\xi^{MI}}\right) - W^{MI} \exp\left(\frac{\mathbf{x}_i - \mathbf{x}_j}{\gamma^{MI}}\right) \right] \quad (4.1)$$

where  $U^{MI}$ ,  $W^{MI}$ ,  $\xi^{MI}$ , and  $\gamma^{MI}$  are the morse parameters for  $E_{ij}^{MI}$  and are carefully calibrated using specific experimental data. The same form of the potential with different sets of parameters is also used for  $E_{ij}^{II}$  and  $E_{il}^{MMD}$  (Table B.1). These potential functions govern the motion of internal and membrane nodes inside the cells resulting in the deformation and rearrangement of cells within the tissue.

#### 4.2.2 Equations of motion

Equations of motion differ for membrane nodes and internal nodes since they experience different types of interactions. Due to small size and speed of cells, we assume in the model that nodes are in an overdamped regime [42, 45] where inertia forces acting on the nodes can be neglected compared to the viscous effects. This leads to the following equations of motion describing movements of membrane and internal nodes, respectively:

$$\eta \dot{\mathbf{x}}_i^I = - \left( \sum_j \nabla E_{ij}^{II} + \sum_k \nabla E_{ik}^{MI} \right), \quad (4.2)$$

$$\eta \dot{\mathbf{x}}_j^M = - \left( \sum_i \nabla E_{ij}^{MI} + \sum_k \nabla E_{kj}^{MMS} + \sum_l \nabla E_{lj}^{MMD} + \nabla E_{i(j)-j}^{adh} \right), \quad (4.3)$$

where  $\eta$  is the damping coefficient,  $\mathbf{x}^I$  and  $\mathbf{x}^M$  are positions of internal and membrane nodes, respectively. The dot represents a time derivative.

Eqns. 4.2 and 4.3 are discretized in time using forward Euler method and positions of nodes  $\mathbf{x}_i^I$  and  $\mathbf{x}_i^M$  are incremented at discrete times. The forward Euler discretization of the equation of motion of internal nodes (Eqn. 4.2) has the form:

$$\mathbf{x}_i^I(t + \Delta t) = \mathbf{x}_i^I(t) - \left( \sum_j \nabla(E_{ij}^{II})(t) + \sum_k \nabla(E_{ik}^{MI})(t) \right) \frac{\Delta t}{\eta} \quad (4.4)$$

where  $\Delta t$  is the time step size. The same discretization technique is used for the equation of motion of the membrane nodes.

The model is implemented on a cluster of Graphical Processing Units (GPUs). This enabled us to run large number of simulations with subcellular resolution at the micro-scale with low computational cost and to study the impact of changes in individual cell physical properties on the tissue development at the macro-scale.

#### 4.2.3 Cell cycle

Many of the model parameters were set based on experimental values determined from studies of the *Drosophila* wing disc development, which is an established genetically accessible model of organ development [16]. The growth of the wing disc is relatively spatially uniform, and the growth rate decreases over time as the tissue reaches to its final size [118]. The growth rate for cell  $i$  is modeled by an exponentially decaying function fit to the specific experimental data [118], with a random term representing stochastic variation among cells:

$$g_i(t) = (g_{0_{avg}} + Rand[-g_0, g_0]) e^{-k_g t} \quad (4.5)$$

where  $g_{0_{avg}}$  is the average growth rate of cells in the beginning of a simulation and  $Rand[-g_0, g_0]$  is a random number chosen from a uniform distribution in the range  $[-g_0, g_0]$ .  $k_g$  is the decay constant of the growth rate. The growth progress of the cells at time  $t$  is represented by  $CP(t)$ . The variable Cell Progress ( $CP \in [0, 1]$ )

evolves with the rate  $g_i(t)$  from the beginning of interphase  $CP = 0$  to the end of the cell division  $CP = 1$  as described by the following:

$$CP_i(t + \Delta t) = CP_i(t) + g_i(t) \cdot \Delta t \quad (4.6)$$

The number of internal nodes inside the cell increases as the cell grows (Fig. 4.2). It has been shown experimentally that epithelial cells undergoing mitosis increase their intracellular pressure by adjusting their osmolarity relative to their surroundings [107]. Additionally, the actomyosin cortex is enriched, and cellular adhesion to the substrate and to neighboring cells are downregulated [107, 133]. Since these changes in mitotic cells occur concurrently, the relative impact on mitotic cells cannot easily be decomposed into separable effects in experiments.

To simulate mitotic rounding, parameters regulating cell-cell adhesion, actomyosin cortex, and internal pressure of cells in the mitotic phase (M phase) are modified (Table B.1), representing changes of cell physical properties during mitosis [107]. Mitosis is modeled by a linear transition from the interphase parameter range to the mitotic parameter range determined based on the experimental observations. For example  $U^{MI}$ , a Morse parameter used for representing cytoplasmic pressure on the membrane of the cell, is varied from the interphase value  $U_{Inter}^{MI}$  to the mitotic value  $U_{Mit}^{MI}$ , by using the following function of CP:

$$U^{MI} = U_{Inter}^{MI} \frac{1 - CP}{1 - CP_{Mit}} + U_{Mit}^{MI} \frac{CP - CP_{Mit}}{1 - CP_{Mit}} \quad (4.7)$$

where  $U_{Mit}^{II}$  is the parameter value in the mitosis range, and  $CP_{Mit}$  is the threshold of growth progress at which the mitotic phase starts. Similar linear variations of parameter values are used for representing enrichment of actomyosin cortex and reduction in cell-cell adhesion with neighboring cells in mitotic phase (see Table B.1).

Cells in the mitotic (M) phase - which lasts approximately 30 minutes - divide into

two daughter cells (Fig. 4.2b). As CP becomes equal to 1, cytokinesis occurs that is modeled by separating internal and membrane elements of the mother cell into two sets representing daughter cells. The axis of division is implemented perpendicular to the cell’s longest axis, following Hertwig’s rule [75], prior to the initiation of mitotic rounding [78]. New membrane elements are created along the cleavage plane for each daughter cell. After division, cell parameters for nodes of each daughter cell are set to calibrated interphase values. CP is reset to zero for both daughter cells.

Membrane nodes in the beginning of a simulation are arranged in a circle for each cell, and internal nodes randomly placed within each cell (Fig. 4.3a). After initialization, internal nodes rapidly rearrange in a simulation, and cells self-organize into a polygonal network (Fig. 4.3b), similar to the experimentally observed cell packing geometry of epithelia. Cells constantly grow, divide and interact with each other resulting in a detailed simulation of the developing epithelial tissue (Fig. 4.3c-d).

#### 4.2.4 Model calibration

Before running predictive model simulations, the model parameters, described in previous section, were calibrated using experimental data for the *Drosophila* wing disc, which is a powerful model for studying organ formation.

Mechanical stiffness of the actomyosin cortex is primarily responsible for the modulus of elasticity  $E$  and the Poisson’s ratio of the cells [86].  $E$  is experimentally obtained by applying stretching forces to the opposite sides of a cell, and measuring the cell’s deformation due to stretching [76, 88]. This experiment can be reproduced *in silico* by applying forces to membrane nodes on either side of a simulated cell, and measuring the deformation (Fig. 4.4a-a”, 4.4c). Model parameters that control cortical stiffness ( $k_{Inter}^{St}$  and  $L_{Inter}^{St}$ ) were calibrated such that the cell deformations match the experimental data. The calibrated parameters lead to  $E= 19 \text{ kPa}$ , which

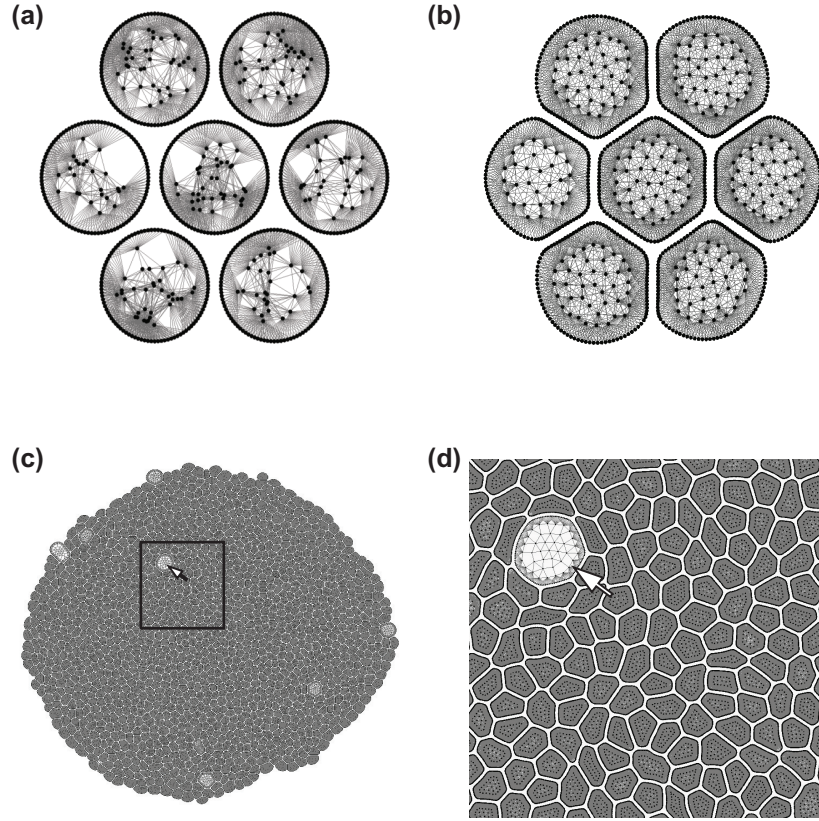


Figure 4.3: Initial conditions and sample simulation output. (a) Initial condition of a simulation with seven initially non-adherent circular cells. Each cell starts with 100 membrane elements and 20 internal elements. (b) Initial formation of an epithelial sheet after cells adhere to each other. An equilibrium distribution of internal nodes is reached for each cell. (c) Epithelial sheet after 55 simulated hours of proliferation. (d) Enlarged view of the selected region showing different cell shapes and sizes due to interactions between cells. The large cell is undergoing mitotic rounding (MR). Arrow indicates a mitotic cell before division.



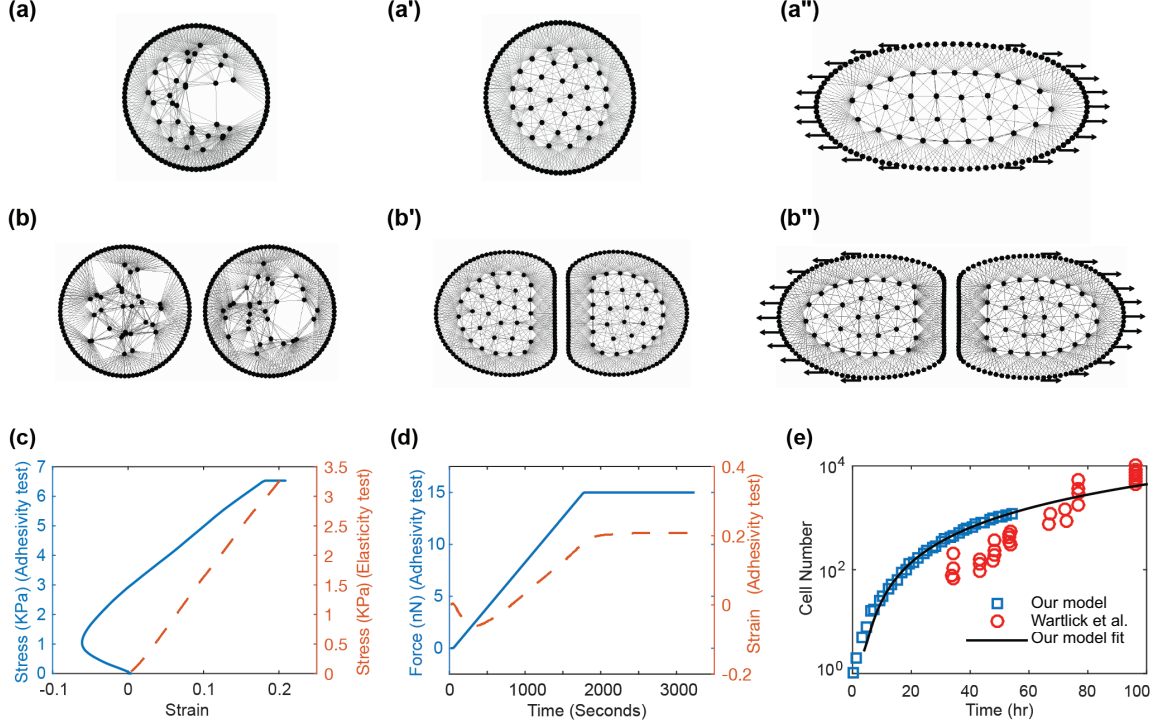


Figure 4.4: Calibration of model parameters through simulations. (a-a'') Calibration test to determine parameters for cell elasticity, analogous to experimental single cell stretching tests [88], (a) Initial condition  $t=0$ , (a') 6 minutes after simulation with no force applied, (a'') after 72 minutes cell is completely on tension (b-b'') Cell adhesivity test, analogous to experimental tests [76] for calibrating the level of cell-cell adhesion between adjacent cells. (b) Initial condition  $t=0$ , (b') 6 minutes after simulation begins with no force applied, (b'') after 72 minutes, 15 nN force is applied. (c) Stress versus strain for single cell calibration (red line) and stress versus strain for calibrating the level of adhesivity between the two cells (blue line). Initial negative strain in adhesivity test is due to strong adhesion between two cells. (d) Force and strain as a function of time for adhesivity test. (e) Tissue growth rate calibration by comparing with the experimental data by Wartlick et al. [133].

is within the biological range of 10 - 55  $kPa$  measured for epithelial cells [76, 88].

The cell-cell adhesive force  $F_{adh}$ , or the force needed to detach two adhered cells from each other, can be adjusted in our model by varying the model parameter that control the strength of cell-cell adhesions ( $k_{Inter}^{Adh}$ ).  $F_{adh}$  is experimentally obtained by measuring the force needed to detach two adhered epithelial cells from each other [76]. This experiment can be reproduced *in silico* by applying forces to membrane nodes on either side of two adhered cells (Fig. 4.4b-b"). Parameters corresponding to cell-cell adhesion ( $k_{Inter}^{adh}$  and  $L^{adh}$ ) were calibrated such that for a cell with apical perimeter  $p$  we have  $F_{adh}/p = 20nN/\mu m$  (Fig. 4.4d), which is in the range of experimental results for epithelial cells [13, 50] .

Cells in the wing disc have spatially-uniform growth-rates that slow down as the tissue approaches its final size [133]. The growth rate parameter described by Eqn. 4.5 was calibrated such that the number of cells in time as the tissue grows matches experimental data [133] (Fig. 4.4e). Cells in mitosis deviate from cells in interphase in their area and roundness (Fig. 4.5a). Force parameters such as the internal pressure, cortical stiffness, and adhesivity of cells were linearly increased from the start of mitosis to the end of mitosis (Fig. 4.5b-d). Model parameters were selected such that the ratio of mitotic area to interphase area ( $A_{ratio}$ ), and cell roundness ( $R$ ) were calibrated to data from the wing disc. Details on measurements of  $A_{ratio}$  and  $R$  are provided in Appendix B.1.

### 4.3 Results

#### 4.3.1 Tissue topology emerges from self-organization driven by cellular mechanics.

After model calibration, simulations were run to determine whether this cellular-scale calibration was sufficient to recapitulate expected topological properties of the tissue (Fig. 4.6). One way to confirm that our simulations generate reasonable results

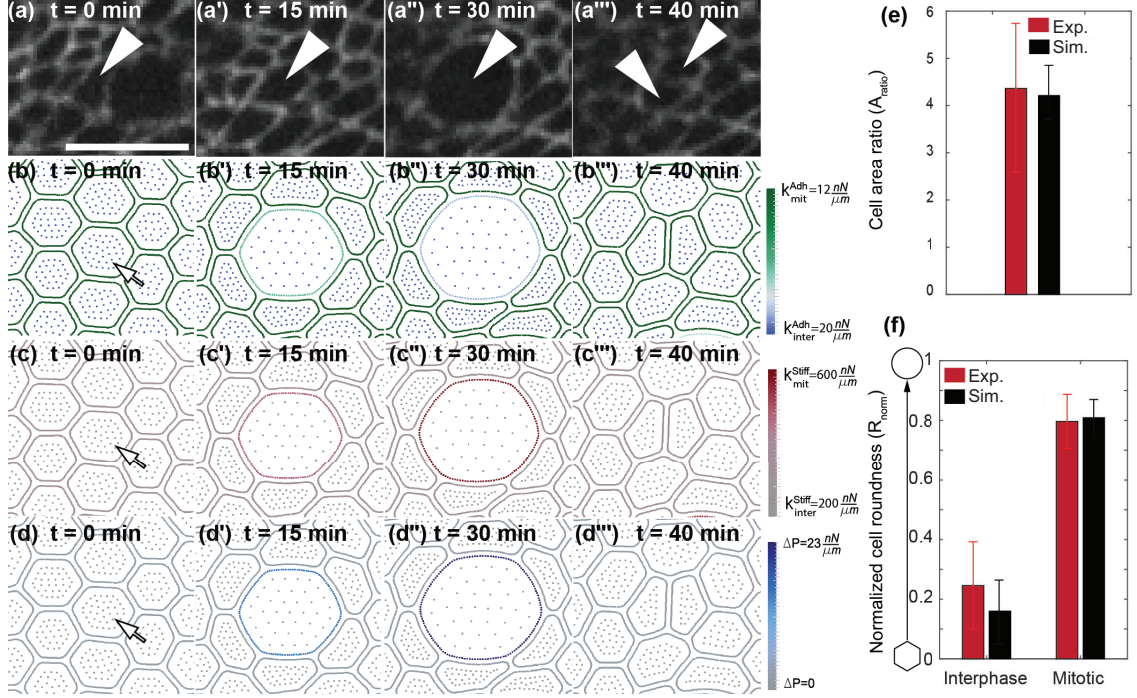


Figure 4.5: (a-a''') Time-lapse confocal images of cell undergoing mitosis in the wing disc with E-Cadherin:GFP-labeled cell boundaries. Scale bar is  $5 \mu\text{m}$ . Arrows indicate daughter cells. (b-d''') Time series from Epi-Scale simulation of a cell undergoing mitosis and division with illustration of: (b) adhesive spring stiffness, (c) cortical spring stiffness, and (d) internal pressure, normalized to their interphase values. (e-f) Comparison of size and roundness of mitotic cells with experimental data for the *Drosophila* wing disc. Arrow represents mitotic cell.

is to confirm that the simulated tissues satisfy through evaluation of the three laws describing topological relationships: Euler’s law, Lewis law, and Aboav-Weaire Law. Euler’s law states that, on average, cells forming a packed sheet should be hexagonal [114]. The Lewis law states that cells with more neighbors should have a larger normalized area [80]. The Aboav-Weaire law states that the average polygon class of each cell’s neighbors decreases as the cell’s polygon class increases [80]. Simulation results obtained using the calibrated model show the average side of cells to be equal to 5.96 in a very good agreement with the Euler’s law. The model simulations also satisfy the other two laws as shown in Fig. 4.6b.

Another metric for tissue topology is the distribution of cell neighbor numbers, or polygon class distribution [28, 80]. Based on the simulation results for studying the tissue growth, the polygon class distribution approaches steady state after 35 hours (Fig. 4.6c). This distribution matches with the ones reported experimentally for the wing disc and other epithelial systems (Fig. 4.6d) as well as obtained using other computational models for simulating growing tissues such as vertex based model [40].

#### 4.3.2 Impacts of adhesion, stiffness, and cytoplasmic pressure on MR

The model is suitable for generating and testing hypotheses regarding mechanical mechanisms of mitotic because it is capable of representing non-polygonal shapes of cells, while other models such as vertex based model impose a polygonal shape to the cells. Moreover, the parameters representing mechanical cell properties in our model can be directly related to the properties of cells measured in experiments. Experiments have shown that cell-cell adhesion, cortical stiffness, and internal pressure are all involved in determining the shape of a mitotic cell, but quantitative contributions of cell mechanical property changes in individual cells within tissues are not currently possible. Simulations were conducted to predict the relative contributions of different cell properties to the relative area ratio ( $A_{mit}/A_{int}$ ) and normalized roundness

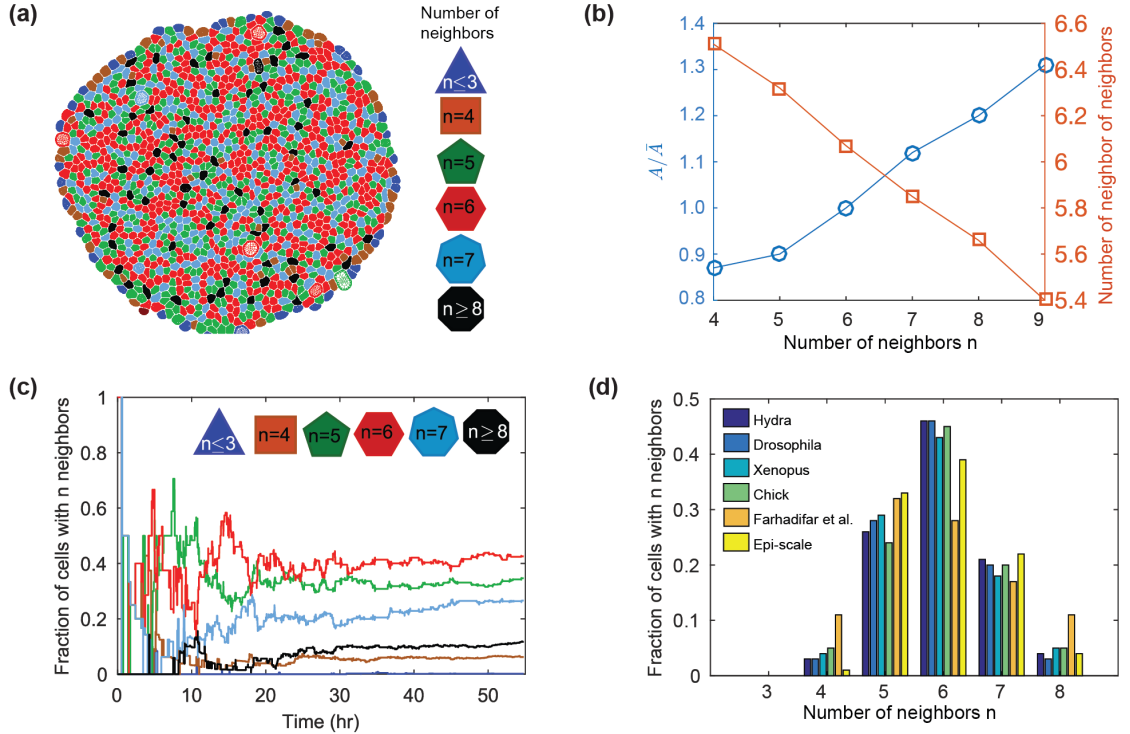


Figure 4.6: Emergence of tissue-level statics from model simulations. (a) Sample simulation output showing cells with different numbers of neighbors as different colors (corresponding to legend in b). (b) Average relative area ( $A/\bar{A}$ ) and average polygon class of neighbors for cells of different polygon classes verifying that simulation results follow Lewis law and Aboav-Weaire law.  $A$  is apical area of cell and  $\bar{A}$  is the average apical area of the population of cells. (c) Simulations initiated from seven cells reaches steady-state polygon-class distribution after approximately 35 h of simulated time. (d) Comparison of polygon class distributions obtained by our model (Epi-Scale) with various biological systems (data extracted from [49]) and a vertex based model by Farhadifar et al. [40].

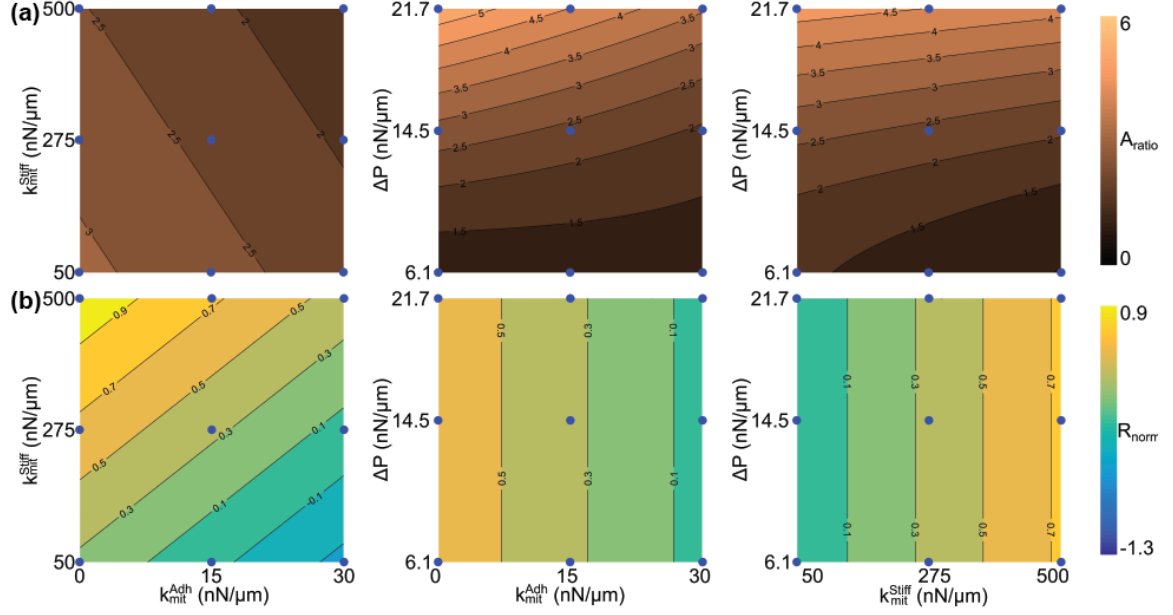


Figure 4.7: Contour plots for FFD experiment where (a) shows the area ratio ( $A_{ratio} = A_{mit}/A_{inter}$ ) and (b) shows the normalized roundness ( $R_{norm}$ ).

( $R_{norm}$ ) of mitotic cells. The details of these calculations are provided in section B.1. To understand the relationships between the mitotic parameters of the model ( $k_{mit}^{Adh}$ ,  $k_{mit}^{Stiff}$ ,  $\Delta P$ ) and mitotic rounding ( $A_{ratio}$  and  $R_{norm}$ ), parameter values were selected in a three-level full factorial design (FFD) (Fig. B.2a, and section B.2.1). A region of parameter space was selected where the error in mitotic rounding measurements ( $A_{ratio}$  and  $R_{norm}$ ) was minimized as shown in the Pareto front (Fig. B.2b). A regression model was fit to the results of the FFD, and showed that for large changes,  $\Delta P$  was the primary regulator of  $A_{ratio}$ , but  $k_{mit}^{Adh}$  and  $k_{mit}^{Stiff}$  were the primary regulators of  $R_{norm}$  (Fig. 4.7a-b).

The region of parameter space closest to experimental values of cell area and roundness was explored [98] with a central composite design (CCD) as a second iteration to more precisely determine the relative contribution of each physical parameter on MR within experimentally observed ranges (Fig B.2a, and section B.2.3). This result quantitatively defines the predicted variation in mitotic cell-cell adhesion,

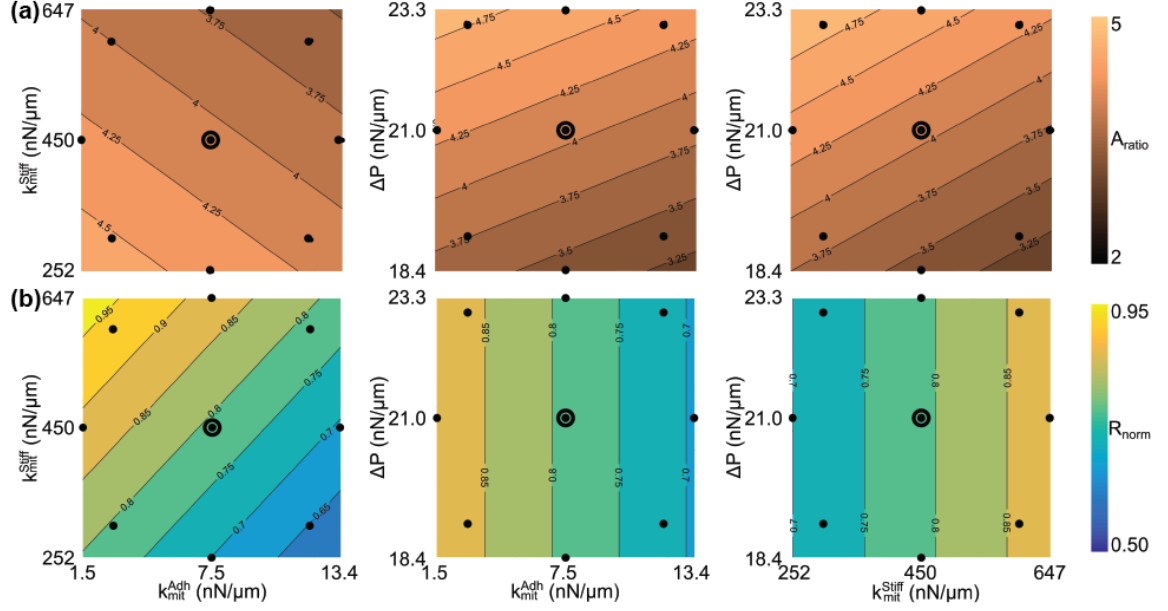


Figure 4.8: Contour plots for CCD experiment where (a) shows the area ratio ( $A_{ratio} = A_{mit}/A_{inter}$ ) and (b) shows the normalized roundness ( $R_{norm}$ ).

stiffness and pressure that explains the variation in mitotic area ratio and rounding observed in mitotic epithelial cells. To keep mitotic rounding within the range of variation observed,  $\Delta P$  must be tightly regulated (2D units of range are 19-23  $nN/\mu m$ ,  $\sim 17\%$  variation in range about the calibrated point), whereas the requirements for  $k_{mit}^{Adh}$  and  $k_{mit}^{Stiff}$  are less stringent  $\sim 100\%$  and  $\sim 67\%$  respectively.

Our results revealed that the regulation of mitotic rounding is approximated well by linear regression models (Fig. 4.8a-b) for parameters that lead to physiological values of  $A_{ratio}$  and  $R_{norm}$  for *Drosophila* wing disc cells (Fig. 4.5). This means that regulation is in the linear regime, which is good attribute for a tightly regulated, engineered process. Since interaction terms are not significant, this means that each cell mechanical property is effectively independently regulated.

Mitotic pressure was found to be the primary regulator of mitotic cell area, while both cell-cell adhesion and cortical stiffness reduce area expansion slightly (Fig 4.8a). An increase in cell-cell adhesion opposes roundness whereas increased cortical stiffness

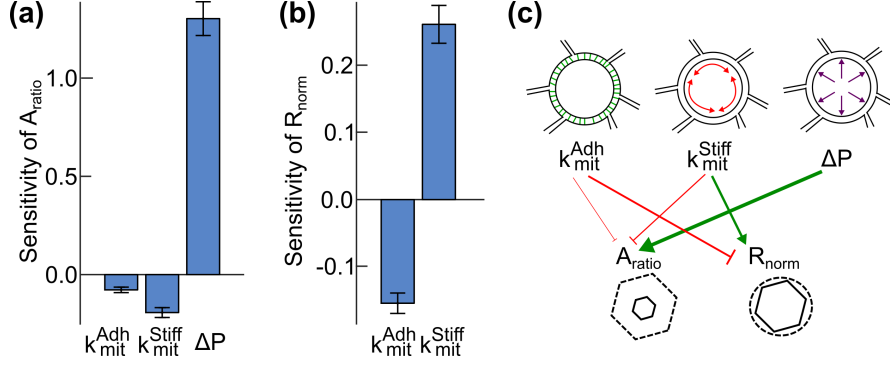


Figure 4.9: Quantification of relative sensitivity of adhesion, stiffness and pressure sensitivities to mitotic area expansion and roundness within experimental ranges. Sensitivity estimation of  $A_{ratio}$  (a) and  $R_{norm}$  (b) to 1% variation in the three mitotic parameter set points  $k_{mit}^{Stiff}$ ,  $k_{mit}^{Adh}$ , and  $\Delta P$ . Sensitivity was estimated from the reduced RSM model described in Fig. 4.7a-b after stepwise model regression (p-value cutoff of 0.01). (c) Proposed mechanical regulatory network defined for physiological ranges within the parameter ranges defined by the CCD (Run 2, Fig. B.2a) that is based on the local sensitivity analysis. Cell adhesivity, an increase in  $k_{mit}^{Adh}$ , slightly inhibits area expansion and strongly inhibits roundness. Membrane stiffness,  $k_{mit}^{Stiff}$ , inhibits area expansion and promotes roundness. Mitotic area expansion is most sensitive to variation in the mitotic pressure change ( $\Delta P$ ), but pressure has little effect on roundness over the calibrated physiological ranges.

promotes roundness for small perturbations (Fig 4.8b).

To define the relative contributions of mechanical properties on  $A_{ratio}$  and  $R_{norm}$  under physiological or wild-type conditions, local sensitivity analysis (Fig. 4.9a-b, and section B.3) was performed. Within the physiologically relevant parameter space, pressure plays an important role in regulating cell size (Fig. 4.9a) but it does not play a strong role on roundness (Fig. 4.9b). Stiffness and Adhesion are important in tuning the degree of mitotic roundness (Figs. 4.8b, and 4.9b).

These results are summarized in the form of mechanical sensitivity model (Fig. 4.9c) analogous to protein interaction networks. The mechanical regulatory network summarizes how small variations in each mechanical property of cells changes the relative mitotic area expansion and roundness within experimentally observed ranges of mitotic rounding. Thus, this model is able to assign to each mechanical property a



unique and separable contribution to overall shape changes that occur during MR under physiological conditions in epithelia.

#### 4.4 Discussion

The roles of pressure, stiffness and adhesion even in mitotic cells in single cell culture in suspension or attached to substrates, are still not resolved in the literature and largely unexplored in the tissue context [124, 143]. Previous conclusions are derived from very strong experimental perturbations such as complete inhibition of actin polymerization that break the system. For example, Stewart et al. indicate that both pressure and the actin-myosin cortex are important for mitotic swelling [124] while Zlotek-Zlotkiewics et al., observed that the actin-myosin cortex is not involved in mitotic swelling [143]. Both studies also are focused on cultured cells and, therefore, the impact of mechanical properties of mitotic cells on mitotic rounding in dense epithelial tissues is even less clear.

General models for investigating epithelial mechanics, including mitotic rounding as a proof of principle, require coupling of biologically calibrated mechanical components capable of representing non-polygonal cell shapes, and simulating the membranes as well as cytoplasm of individual cells as separate entities. To accomplish this, a novel multi-scale sub-cellular model was developed in this work for simulating mechanical and adhesive properties of cells in the developing columnar epithelium of the wing disc which consists of a single layer of cells. The model approximates the tissue as a 2D surface since the majority of the contractile and adhesive forces are localized at the apical surface of the epithelium (Fig. 4.1b). Parameters for the computational model were obtained by calibrating the model using single cell stretching experiments, double cell stretching experiments, area and roundness of mitotic cells, and tissue growth rate of the *Drosophila* wing disc. Cell-cell adhesion and cell elasticity were calibrated using experimental data on single cells. The calibrated

model was tested by successfully reproducing emergent properties of developing tissue such as the polygon class distributions for both interphase and mitotic cells without additional calibration or parameter tuning.

Our computational environment enables systematic testing of new hypotheses about the underlying biophysical mechanisms governing mitotic rounding of epithelial cells within the developing tissue micro-environment. The model predicts the quantitative impact of each mechanical property change on mitotic cell expansion and rounding (Figs. 4.7, 4.8, and 4.9), enabling a predictive model mapping how mitotic mechanical properties specify mitotic rounding. Additionally, our preliminary results show that mitotic rounding under super-physiological pressure increases (greater than calibrated values) can result in cell-cell rearrangements (T1 transitions) of the neighboring cells, due to rapid increase of the apical surface of the mitotic cell. It will be exciting to explore the mechanical impacts of mitotic rounding on epithelial morphogenesis in future studies as well as to expand the model to include a description of the kinetics of cytokinesis.

It is currently challenging to target only dividing cells in a tissue. Cell-cell adhesion is dictated by the adhesive interactions of adherent junctions, which can be modulated through genetic modification of E-cadherin molecules to alter their binding affinities. Cell stiffness can be adjusted by reducing the contractility of the cortex through pharmacological perturbations. Internal pressure of cells is primarily dictated by osmotic channels regulating the flow of water and ions through the cell membrane, and can be adjusted by modulating those channels, or by changing the osmolarity of the media. One experimental approach that might in future be used for testing the model predictions would be to regulate the expression of E-Cadherin, Myosin-II, and osmotic channel antagonists under a Cyclin B promotor, active during mitosis, resulting in modulation only in dividing cells [24, 46]. Alternatively, optogenetic methods could be employed to selectively regulate individual cell properties

[53].

Simulations provide insight into the individual contributions of cell properties to MR and can predict the consequences of dysregulation of mitotic cell rounding on the development and homeostasis of epithelial tissues. Determining which aspects of mitotic rounding are most sensitive to perturbed cell properties in dense tissues, including solid tumors, can help direct efforts to identify cellular processes that specifically block mitosis in highly proliferative tumors, but that are not damaging to non proliferative cells [143].

## APPENDIX A

### PSEUDOMONAS AERUGINOSA MOTILITY SOURCE CODE

The simulation code is consisted of several files. In “Main.cpp” I am including the main operations for solving equations of motion of bacteria. The initial distribution and orientation of bacteria is initialized in “Initializer.cpp”. The header “BufferFn.h” is written to implement the periodic boundary condition in the simulations. The header file “CellDistance.h” searches for the bacteria that are within the interaction distance, to include different cell-cell interactions in the model. The rest of this appendix contains the content of the above mentioned files.

#### A.1 Main.cpp

```
#include <iostream>
#include <fstream>
#include "stdio.h"
#include "nrutil.c"
#include "initializer.h"
#include "BufferFn.h"
#include "BuffCounter.h"
#include "CellDistance.h"
#include <time.h>
#define Num_Of_Cells 648
#define Lx 36
#define Ly 36
#define Cell_Length 2.0
#define Cell_Width 0.5
#define Pili_Length 0.5
#define Cell_Vel 3.0
#define PI 3.14159
```

```

using namespace std;

int main()
{
double Buffer_Width = 2.0* Cell_Length;
double Int_distance;
int n, i, j, cc=0, step=0;
double t, dt = 0.0001, SimTime = 2000.0, rand_noise; //time: sec
int NumSteps = SimTime/dt;
double rm, ru = 20.0*dt, Epsilon = 90.0*SQR(dt), m=1.0e-5, Inertia;
double FMr = 1.0e-1; //F = 10.0e-13N and m = 1.0e-5 Kg F/m*1e6 - unit
double KMr = 1.0e5; //k=1.0e-6 N/m, m=1.0e-5kg. x1.0e6 convert unit
double xProj, yProj, eps=1.0e-10;
char filename[50];
Inertia = (1.0/12)*m*SQR(Cell_Length);
Int_distance = 2.0*Pili_Length+Cell_Width;
rm = Int_distance;
int estimation = 24*Num_Of_Cells/Lx;
double ALPHA, ROTdir, rVel, rALPHA, MVdirX, MVdirY;
double d_x, d_y, d_rx, d_ry, d_wx, d_wy, d_tta, disCMS;
double *NoiseTheta, *DeltaTheta, *xPosChange, *yPosChange;;
double **NewCellDis, **OldCellDis, **PosChange, k_spring=1.0e-6;
double *Real_centerXpos, *Real_centerYpos, *Real_theta;
double **rx, **ry, **wx, **wy;
double *All_centerXpos, *All_centerYpos, *All_theta;
double **x_hit, **y_hit, **disBcells;

// Memory allocation for the defined variables
DeltaTheta = dvector(1, Num_Of_Cells+estimation);
NoiseTheta = dvector(1, Num_Of_Cells+estimation);
NewCellDis = dmatrix(1, Num_Of_Cells+estimation,
                     1, Num_Of_Cells+estimation);
OldCellDis = dmatrix(1, Num_Of_Cells+estimation,
                     1, Num_Of_Cells+estimation);
PosChange = dmatrix(1, Num_Of_Cells+estimation,
                     1, Num_Of_Cells+estimation);
xPosChange = dvector(1, Num_Of_Cells+estimation);
yPosChange = dvector(1, Num_Of_Cells+estimation);
Real_centerXpos = dvector(1, Num_Of_Cells);
Real_centerYpos = dvector(1, Num_Of_Cells);

```

```

Real_theta = dvector(1,Num_Of_Cells);

rx = dmatrix(1,Num_Of_Cells+estimation,1,Num_Of_Cells+estimation);
ry = dmatrix(1,Num_Of_Cells+estimation,1,Num_Of_Cells+estimation);
wx = dmatrix(1,Num_Of_Cells+estimation,1,Num_Of_Cells+estimation);
wy = dmatrix(1,Num_Of_Cells+estimation,1,Num_Of_Cells+estimation);

All_centerXpos = dvector(1,Num_Of_Cells+estimation);
All_centerYpos = dvector(1,Num_Of_Cells+estimation);
All_theta = dvector(1,Num_Of_Cells+estimation);

// intializing the simulation
initializer(Real_centerXpos, Real_centerYpos, Real_theta);

// counting the ghost cells for periodic boundary condition
BuffCounter(Real_centerXpos, Real_centerYpos, Real_theta, cc);

// placing ghost cells around the boundaries
BufferFn(All_centerXpos, Real_centerXpos, All_centerYpos,
          Real_centerYpos, All_theta, Real_theta);

// Here I'm writing the init condition to CellInfo000000.txt
FILE *fid;
fid = fopen("wild-type/CellInfo000000.txt", "w");
for (i=1;i<=Num_Of_Cells;i++){
Real_centerXpos[i] = All_centerXpos[i];
Real_centerYpos[i] = All_centerYpos[i];
Real_theta[i] = All_theta[i];
fprintf(fid, "%d_\\%f_\\%f_\\%f\\n", i, All_centerXpos[i],
        All_centerYpos[i], All_theta[i]);}
fclose(fid);

//***** Now I find the distance between cells *****
x_hit = dmatrix(1, Num_Of_Cells+estimation,
                 1, Num_Of_Cells+estimation);
y_hit = dmatrix(1, Num_Of_Cells+estimation,
                 1, Num_Of_Cells+estimation);
disBcells = dmatrix(1, Num_Of_Cells+estimation,
                    1, Num_Of_Cells+estimation);

CellDistance(All_centerXpos, All_centerYpos, All_theta,

```

```

        cc, x_hit, y_hit, disBcells);

// time steps of simulations performed as follows:
for (t = dt; t<=SimTime+dt; t+=dt)
{
    for (i = 1; i< Num_Of_Cells+cc; i++)
    {
        rand_noise = noiseStrength *
            ( 2.0 * ((double) rand() / (RANDMAX))-1);
        NoiseTheta[i] = rand_noise;
    }
    step = step+1;

    //collision function is copied in here:
    //=====Initial Conditions on rx, ry, wx and wy=====
    for (i = 1; i<=Num_Of_Cells+cc; i++)
        for (j = 1; j<= Num_Of_Cells+cc; j++)
            {if (i!=j && disBcells[i][j] > eps)
                {xProj = (x_hit[i][j] - x_hit[j][i])/disBcells[i][j];
                 yProj = (y_hit[i][j] - y_hit[j][i])/disBcells[i][j];}
            if (i!=j && disBcells[i][j] < eps)
                {xProj = sin(All_theta[j]);
                 yProj = cos(All_theta[j]);}
            if (i==j)
                {xProj=0.0;
                 yProj = 0.0;}
            rx[i][j] = xProj * disBcells[i][j];
            wx[i][j] = 0.0; //Cell_Vel*xProj;
            ry[i][j] = disBcells[i][j]*yProj;
            wy[i][j] = 0.0; //Cell_Vel*yProj;
        }

    /* =====
    each real simulation time step is divided to "NumSteps" time
    steps and the equations are solved using the Euler scheme
    ===== */

    for (i=1; i<=Num_Of_Cells+cc; i++)
        DeltaTheta[i] = 0.0;

    for (i=1; i<=Num_Of_Cells+cc; i++)
    for (j=1; j<=Num_Of_Cells+cc; j++)

```

```

OldCellDis[i][j]=disBcells[i][j];
{
for (i=1;i<=Num_Of_Cells+cc;i++)
  for (j=1; j<=Num_Of_Cells+cc; j++)
    {
      if (i != j && disBcells[i][j]<=(Int_distance)
        && disBcells[i][j]>Cell_Width+ru){
        xProj = (x_hit[i][j] - x_hit[j][i])/disBcells[i][j];
        yProj = (y_hit[i][j] - y_hit[j][i])/disBcells[i][j];

        d_wx = dt*(-KMr*(disBcells[i][j]-rm)* xProj);
        wx[i][j] = wx[i][j] + d_wx;
        d_rx = dt * wx[i][j];
        rx[i][j] = rx[i][j] + d_rx;

        d_wy = dt * (-KMr*(disBcells[i][j]-rm) * yProj);
        wy[i][j] = wy[i][j] + d_wy;
        d_ry = dt * wy[i][j];
        ry[i][j] = ry[i][j] + d_ry;

        // **FINDING TORQUE & ANGULAR VELOCITY **
        X_hitFROMcenter = x_hit[i][j] - All_centerXpos[i];
        Y_hitFROMcenter = y_hit[i][j] - All_centerYpos[i];
        ALPHA = 0.5 * KMr * (disBcells[i][j]-rm)*
          (Y_hitFROMcenter* xProj-X_hitFROMcenter*yProj);
        DeltaTheta[i] = DeltaTheta[i] + 0.5 * ALPHA * SQR(dt);

        // *****Now Delta_Theta is calculated fro each cell
        NewCellDis[i][j] = sqrt(SQR(rx[i][j]) + SQR(ry[i][j]));
        disBcells[i][j] = NewCellDis[i][j];
        disBcells[j][i] = disBcells[i][j];
      }
    }
  if (i != j && disBcells[i][j] <= Cell_Width &&
    disBcells[i][j]>=Cell_Width-ru)
    {xProj = (x_hit[i][j] - x_hit[j][i])/disBcells[i][j];
      yProj = (y_hit[i][j] - y_hit[j][i])/disBcells[i][j];

      d_wx = dt * FMr *(disBcells[i][j]-Cell_Width-ru)*
        (disBcells[i][j]-Cell_Width-ru)/(Epsilon*ru*ru)*xProj;
      wx[i][j] = wx[i][j] + d_wx;
      d_rx = dt * wx[i][j];

```



```

    rx[i][j] = rx[i][j] + d_rx;

    d_wy = dt * FMr * (disBcells[i][j] - Cell_Width - ru) *
    (disBcells[i][j] - Cell_Width - ru) / (Epsilon * ru * ru) * yProj;
    wy[i][j] = wy[i][j] + d_wy;
    d_ry = dt * wy[i][j];
    ry[i][j] = ry[i][j] + d_ry;

    // **FINDING TORQUE AND ANGULAR VELOCITY OF EACH POINT**
    X_hitFROMcenter = x_hit[i][j] - All_centerXpos[i];
    Y_hitFROMcenter = y_hit[i][j] - All_centerYpos[i];
    ALPHA = Cell_Length * (X_hitFROMcenter *
    yProj - Y_hitFROMcenter * xProj);
    DeltaTheta[i] = DeltaTheta[i] + 0.5 * ALPHA * SQR(dt);

    NewCellDis[i][j] = sqrt(SQR(rx[i][j]) + SQR(ry[i][j]));
    disBcells[i][j] = NewCellDis[i][j];
    disBcells[j][i] = disBcells[i][j];}

}
} //end of i loop
for (i=1; i<=Num.Of_Cells+cc; i++)
    for (j=1; j<=Num.Of_Cells+cc; j++)
        PosChange[i][j] = 1.0 *
            (disBcells[i][j] - OldCellDis[i][j]);

for (i=1; i<=Num.Of_Cells+cc; i++)
    {for (j=1; j<=Num.Of_Cells+cc; j++)
        {if (i != j && disBcells[i][j]>eps) //check: zero disBcells
            {xProj = (x_hit[i][j] - x_hit[j][i]) / disBcells[i][j];
            yProj = (y_hit[i][j] - y_hit[j][i]) / disBcells[i][j];
            xPosChange[i] = xPosChange[i] + xProj * PosChange[i][j];
            yPosChange[i] = yPosChange[i] + yProj * PosChange[i][j];}
        if (i != j && disBcells[i][j]<eps)
            {xProj = 0.0;
            yProj = 0.0;
            xPosChange[i] = xPosChange[i] + xProj * PosChange[i][j];
            yPosChange[i] = yPosChange[i] + yProj * PosChange[i][j];}
        }
    }
All_centerXpos[i] = All_centerXpos[i] + xPosChange[i] +
    dt * Cell_Vel * cos(All_theta[i]);

```

```

xPosChange[i] = 0.0;
All_centerYpos[i] = All_centerYpos[i] + yPosChange[i] +
                    dt* Cell_Vel * sin(All_theta[i]);

All_theta[i] = All_theta[i] + DeltaTheta[i] + NoiseTheta[i];
    if (All_theta[i] > 2.0* PI)
        All_theta[i] = All_theta[i] - 2.0*PI;
    else if (All_theta[i] < 0)
        All_theta[i] = All_theta[i] + 2.0*PI;
}

for (i=1; i<=Num_Of_Cells;i++){
    Real_centerXpos[i] = All_centerXpos[i];
    Real_centerYpos[i] = All_centerYpos[i];
    Real_theta[i] = All_theta[i];
}

BuffCounter(Real_centerXpos, Real_centerYpos, Real_theta, cc);
BufferFn(All_centerXpos,Real_centerXpos,
        All_centerYpos,Real_centerYpos, All_theta,Real_theta);

CellDistance(All_centerXpos, All_centerYpos,
            All_theta, cc, x_hit, y_hit, disBcells);

if ( step\%50 == 0)
{FILE *fid;
sprintf(filename, "wild-type/CellInfo\%06d.txt", step);
fid = fopen(filename, "w");
for (i=1;i<=Num_Of_Cells+cc;i++)
fprintf(fid, "\%d_\%f_\%f_\%f\n", i, All_centerXpos[i],
        All_centerYpos[i], All_theta[i]);
fclose(fid);
}

}
//Here I write simulation info
FILE *writer;
writer = fopen("wild-type/SimInfo.txt", "w");

```

```

fprintf( writer , " Number_Of_Cells=\%d\n" " Simulation_domain=\%dby\%d\n" " Simulation_time=\%f\n" " Spring_constant=\%f\n" " time_steps=\%f\n" " Cell_Length=\%f\n" " Cell_Vel=\%f\n" " Cell_width=\%f\n" " Pili_length=\%f\n" ,Num_Of_Cells ,
        Lx, Ly, SimTime, k_spring , dt , Cell_Length ,
        Cell_Vel , Cell_Width , Pili_Length );
fclose( writer );

free_dmatrix( x_hit , 1, Num_Of_Cells+estimation ,
              1, Num_Of_Cells+estimation );
free_dmatrix( y_hit , 1, Num_Of_Cells+estimation ,
              1, Num_Of_Cells+estimation );
free_dmatrix( disBcells , 1, Num_Of_Cells+estimation ,
              1, Num_Of_Cells+estimation );

free_dvector( All_centerXpos ,1 ,Num_Of_Cells+estimation );
free_dvector( All_centerYpos ,1 ,Num_Of_Cells+estimation );
free_dvector( All_theta ,1 ,Num_Of_Cells+estimation );
free_dvector( NoiseTheta ,1 , Num_Of_Cells+estimation );

free_dmatrix( rx ,1 ,Num_Of_Cells+estimation ,1 ,Num_Of_Cell+estimation );
free_dmatrix( NewCellDis ,1 ,Num_Of_Cells+estimation ,
              1 ,Num_Of_Cells+estimation );
free_dmatrix( OldCellDis ,1 , Num_Of_Cells+estimation ,
              1, Num_Of_Cells+estimation );
free_dmatrix( PosChange ,1 ,Num_Of_Cells+estimation ,
              1 ,Num_Of_Cells+estimation );
free_dvector( xPosChange ,1 ,Num_Of_Cells+estimation );
free_dvector( yPosChange ,1 ,Num_Of_Cells+estimation );
free_dmatrix( ry ,1 ,Num_Of_Cells+estimation ,
              1 ,Num_Of_Cells+estimation );
free_dmatrix( wx ,1 ,Num_Of_Cells+estimation ,
              1 ,Num_Of_Cells+estimation );
free_dmatrix( wy ,1 ,Num_Of_Cells+estimation ,
              1 ,Num_Of_Cells+estimation );
free_dvector( DeltaTheta ,1 ,Num_Of_Cells+estimation );

free_dvector( Real_centerXpos ,1 ,Num_Of_Cells );
free_dvector( Real_centerYpos ,1 ,Num_Of_Cells );
free_dvector( Real_theta ,1 ,Num_Of_Cells );
return (0);

```

```
}
```

## A.2 Initializer.cpp

```
void initializer
    (double Real_Xpos[], double Real_Ypos[], double Real_theta[])
{
    double X, Y, tta, delta_Dx, delta_Dy, rand_tilt,
    double choose_dir, x_change=0.0, y_change=0.0;
    int counter=0, i, j, k, l;

    srand((unsigned)time(NULL));

    for (i = 1; i<= 6; i++)
        for (j=1; j<=6; j++)
            {X = Cell_Length + (i-0.5) * 6.0;
             Y = Cell_Length + (j-0.5) * 6.0;
             if ((i+j)%2 == 0)
                 {for (k=-1; k<=1; k+=2)
                     for (l=-4; l<=4; l++)
                         {counter = counter +1;
                          rand_tilt = 0.1 *
                              (2.0 * (double) rand()/(RANDMAX) - 1.0);
                          Real_Xpos[counter] = X + k*(Pili_Length +
                              0.5*Cell_Length+Cell_Width)+rand_tilt;
                          Real_Ypos[counter] = Y + l *
                              (2 * Pili_Length + 1.25 * Cell_Width) + rand_tilt;
                          choose_dir = (double) rand()/(RANDMAX);
                          if (choose_dir < 0.5)
                              coef = -1.0;
                          else
                              coef = 0.0;

                          Real_theta[counter] = coef * PI + PI/2 * rand_tilt;
                          }
                     }
            }
    else
        {for (l=-1; l<=1; l+=2)
            for (k=-4; k<=4; k++)
                {counter = counter +1;
                 rand_tilt = 0.1 *
```

```

        (2.0 * (double) rand()/(RANDMAX) - 1.0);
Real_Xpos[counter] = X + k *
    (2 * Pili_Length + 1.25 * Cell_Width) + rand_tilt;
Real_Ypos[counter] = Y + l *
    (Pili_Length+0.5*Cell_Length+Cell_Width)+rand_tilt;
choose_dir = (double) rand()/(RANDMAX);
if (choose_dir < 0.5)
    coef = 1.0;
else
    coef = 3.0;

Real_theta[counter] = coef*PI/2+PI/2*rand_tilt;}
    }
}
}

```

### A.3 BufferFn.h

```

void initializer(double Real_Xpos[],double Real_Ypos[],
    double Real_theta[]){
double X, Y, tta, delta_Dx, delta_Dy, rand_tilt, coef=1.0;
double choose_dir, x_change=0.0, y_change=0.0;
int counter=0, i, j, k, l;
const double PI = 3.141592653589793;

    srand((unsigned)time(NULL));

for (i = 1; i<= 6; i++)
    for (j=1; j<=6; j++)
        {X = Cell_Length + (i-0.5) * 6.0;
        Y = Cell_Length + (j-0.5) * 6.0;
        if ((i+j)%2 == 0)
            {for (k=-1; k<=1; k+=2)
                for (l=-4; l<=4; l++)
                    {counter = counter +1;
                    rand_tilt = 0.1 * (2.0*(double) rand()/(RANDMAX) -1.0);
                    Real_Xpos[counter] = X + k *
                        (Pili_Length + 0.5*Cell_Length+Cell_Width)+rand_tilt;
                    Real_Ypos[counter] = Y + l *
                        (2 * Pili_Length + 1.25 * Cell_Width) + rand_tilt;

```

```

        choose_dir = (double) rand()/(RAND_MAX);
        if (choose_dir < 0.5)
            coef = -1.0;
        else
            coef = 0.0;

        Real_theta[counter] = coef * PI + PI/2 * rand_tilt;
    }
}
else
    {for (l=-1; l<=1; l+=2)
        for (k=-4; k<=4; k++)
            {counter = counter +1;
            rand_tilt=0.1*(2.0*(double) rand()/(RAND_MAX)-1.0);
            Real_Xpos[counter] = X + k *
            (2 * Pili_Length + 1.25 *Cell_Width) + rand_tilt;
            Real_Ypos[counter] = Y + l *
            (Pili_Length+0.5*Cell_Length+Cell_Width)+rand_tilt;
            choose_dir = (double) rand()/(RAND_MAX);
            if (choose_dir < 0.5)
                coef = 1.0;
            else
                coef = 3.0;

            Real_theta[counter] = coef*PI/2 + PI/2*rand_tilt;}
        }
    }
}

```

#### A.4 BufferCounter.h

```

void BuffCounter(double Real_Xpos[], double Real_Ypos[],
    double Real_theta[], int &cc){
    double Buffer_Width = 2.0 * Cell_Length;
    int counterBuff =0;

    for (int i=1;i<=Num_Of_Cells;i++)
    {
        if (Real_Xpos[i] < Buffer_Width)
            counterBuff = counterBuff+1;
        if (Real_Xpos[i] < Buffer_Width && Real_Ypos[i] > Ly )

```

```

        counterBuff = counterBuff+1;
    if (Real_Xpos[i] < Buffer_Width && Real_Ypos[i]<Buffer_Width)
        counterBuff = counterBuff+1;
    if (Real_Xpos[i] > Lx)
        counterBuff = counterBuff+1;
    if (Real_Xpos[i] > Lx && Real_Ypos[i] > Ly)
        counterBuff = counterBuff+1;
    if (Real_Xpos[i] > Lx && Real_Ypos[i]<Buffer_Width)
        counterBuff = counterBuff+1;
    if (Real_Ypos[i] < Buffer_Width)
        counterBuff = counterBuff+1;
    if (Real_Ypos[i] > Ly)
        counterBuff = counterBuff+1;
}
cc = counterBuff;
}

```

## A.5 CellDistance.h

```

void CellDistance(double All_Xpos[], double All_Ypos[],
double All_theta[], int &BuffSize, double **x_hit,
double **y_hit, double **disBcells){

    int i, j, p1, p2, pmid, N = 10;//number of segments on each cell
    double delta = Cell_Length/N;//size of each segment
    double *TAILxPOS, *TAILyPOS, *SLOPE, **X, **Y;
    double dmin, dx1, dx2, dx3, dy1, dy2, dy3, dr1, dr2, dr3;
    TAILxPOS = dvector(1,Num_Of_Cells + BuffSize);
    TAILyPOS = dvector(1,Num_Of_Cells + BuffSize);
    SLOPE = dvector(1,Num_Of_Cells + BuffSize);
    X = dmatrix(1,Num_Of_Cells + BuffSize, 1, N);
    Y = dmatrix(1,Num_Of_Cells + BuffSize, 1, N);

    for ( i=1;i<=Num_Of_Cells+BuffSize;i++){
        TAILxPOS[i] =All_Xpos[i] - 0.5*(Cell_Length)*cos(All_theta[i]);
        X[i][1] = TAILxPOS[i];
        TAILyPOS[i] =All_Ypos[i] - 0.5*(Cell_Length)*sin(All_theta[i]);
        Y[i][1] = TAILyPOS[i];
        SLOPE[i] = tan(All_theta[i]);
    }
}

```

```

for ( i=1;i<=Num_Of_Cells+BuffSize;i++)
    for ( j=2; j<=N;j++)
    {
        X[i][j] = X[i][j-1] + delta * cos( All_theta[i]);
        Y[i][j] = TAILyPOS[i] + SLOPE[i] * (X[i][j]-TAILxPOS[i]);
    }
int GoodI = 1, GoodJ = 1;
double disCM;
for (int m = 1; m<=Num_Of_Cells+BuffSize; m++)
    for (int n=1;n<= m-1;n++)
    {disCM=sqrt(SQR( All_Xpos[m]-All_Xpos[n])+
        SQR( All_Ypos[m]-All_Ypos[n]));
        if ( abs(abs(cos( All_theta[m]))-abs(cos( All_theta[n])))
            <0.01 || disCM>Cell_Length+2*Pili_Length){
            disBcells[m][n] = disCM;
            disBcells[n][m] = disCM;
            x_hit[m][n] = All_Xpos[m];
            y_hit[m][n] = All_Ypos[m];
            x_hit[n][m] = All_Xpos[n];
            y_hit[n][m] = All_Ypos[n];
        }
    else
    {
        dmin = 1000.0;
        for ( i = 1; i<=N; i++)
            {p1 = 1; p2=N;
                while ( abs(p2-p1) != 1 )
                {
                    pmid = floor(0.5*(p2+p1));
                    dx1 = X[m][i]-X[n][p1];
                    dy1 = Y[m][i]-Y[n][p1];
                    dr1 = SQR(dx1) + SQR(dy1);
                    dx2 = X[m][i]-X[n][p2];
                    dy2 = Y[m][i]-Y[n][p2];
                    dr2 = SQR(dx2) + SQR(dy2);
                    dx3 = X[m][i]-X[n][pmid];
                    dy3 = Y[m][i]-Y[n][pmid];
                    dr3 = SQR(dx3) + SQR(dy3);
                    if ( dr1<dr2 )
                        {dr2 = dr3;

```



```

        p2 = pmid;}
    else
        {dr1 = dr3;
        p1 = pmid;
        }
    }

    if ( (dr1<dr2) && (dr1<dmin) )
        {dmin = dr1;
        GoodJ = p1;
        GoodI =i;}
    else if ( dr2<dmin )
        {dmin = dr2;
        GoodJ=p2;
        GoodI=i;
        }
    }

    disBcells[n][m] = sqrt(dmin);//distance bw cell n and m
    disBcells[m][n] = sqrt(dmin);
    x_hit[m][n] = X[m][ GoodI];//where cell n is hit by cell m
    y_hit[m][n] = Y[m][ GoodI];
    x_hit[n][m] = X[n][ GoodJ];//where cell m is hit by cell n
    y_hit[n][m] = Y[n][ GoodJ];
    }
}

//zero-ing the variables
for (i=1; i<=Num_Of_Cells+BuffSize; i++)
    for (j=1; j<=N; j++)
        {X[i][j] = 0.0;
        Y[i][j] = 0.0;}

/**free the allocated memories that I don't need anymore**
free_dvector(TAILxPOS,1,Num_Of_Cells+BuffSize);
free_dvector(TAILyPOS,1,Num_Of_Cells+BuffSize);
free_dvector(SLOPE,1,Num_Of_Cells+BuffSize);
free_dmatrix(X, 1, Num_Of_Cells + BuffSize, 1, N);
free_dmatrix(Y, 1, Num_Of_Cells + BuffSize, 1, N);

}

```

## APPENDIX B

### SENSITIVITY ANALYSIS OF CELL SHAPE AND SIZE

#### B.1 Calculation of area and roundness

Cell area is calculated by summing the triangles that two neighboring membrane nodes and the cell center create, as is shown in Fig. B.1.

Cell roundness  $R$  is quantified by using the isoperimetric quotient, which is defined as follows:

$$R = 4\pi A/p^2, \quad (\text{B.1})$$

where  $A$  is the cell area and  $p$  is the cell perimeter. Interphase cells have polygonal shape, but their roundness increases as they enter the mitotic phase. The roundness is normalized such that a normalized roundness  $R_{norm}$  of 0 is assigned to a perfect

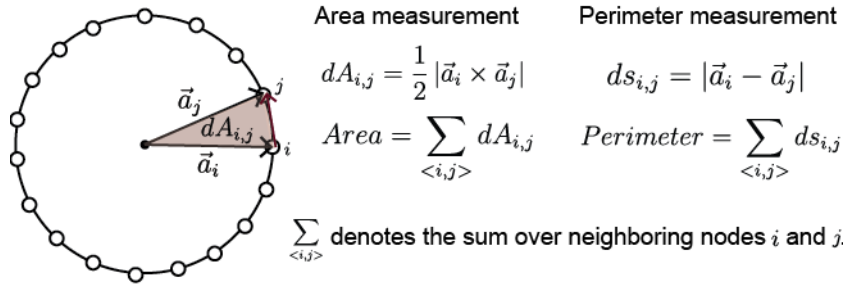


Figure B.1. Calculation of area and perimeter.

hexagon and it becomes 1 for the case of a perfect circle.  $R_{norm}$  is given by:

$$R_{norm} = (R - R_6)/(1 - R_6), \quad (\text{B.2})$$

where  $R_6$  is the isoperimetric quotient of a hexagon and can be calculated from the following general equation for polygons with  $n$  sides.

$$R_n = \frac{\pi}{n \tan(\pi/n)}. \quad (\text{B.3})$$

## B.2 Response surface method

### B.2.1 Exploring the impact of physical properties on MR

Response surface method (RSM) enables one with an efficient way of exploring the parameter space when dealing with computationally expensive models [33, 137]. We developed the RSM of area ratio ( $A_{ratio}$ ) and normalized roundness  $R_{norm}$  as a function of mitotic parameters representing the cortical stiffness, cell adhesion and change of cytoplasmic pressure in mitosis ( $k_{mit}^{Stiff}$ ,  $k_{mit}^{Adh}$  and  $\Delta P$ ). The parameters were first varied in a 3-level full factorial design ( $3^3$  FFD) of experiment. In a  $3^3$  FFD, the three parameters are set to different values in a wide range, and all the possible combinations are tested (Fig. B.2a). The range of variation for each parameter is chosen by including the two extreme values for which cell still behaves biologically and another point set that at the calibration value. A quadratic regression model was fit for each of the two outputs ( $A_{ratio}$  and  $R_{norm}$ ).

### B.2.2 Calibration of mitotic physical parameters

The values of  $R_{norm}$  and  $A_{ratio}$  were measure from timelapse confocal movies of wing disc of *Drosophila* fruit fly. The relative error between the experimental and

computational values of  $R_{norm}$  and  $A_{ratio}$ , is given by:

$$R_{error} = \frac{|R_{exp} - R_{sim}|}{R_{exp}}. \quad (\text{B.4})$$

We report the calibrated values as ones that minimized the error defined above.

### B.2.3 Improving the resolution of investigating the impact of physical properties on MR

We used a central composite design (CCD) to generate a high-resolution RSM of the impact of mitotic parameters ( $k_{mit}^{Stiff}$ ,  $k_{mit}^{Adh}$  and  $\Delta P$ ) on mitotic rounding (Fig. B.2a). CCD was performed over the region where the quadratic model predicted the lowest error in both  $A_{ratio}$  and  $R_{norm}$ . This experiment yielded error values lower than the ones from FFD, and resulted in the biologically calibrated parameter values.

### B.3 Sensitivity analysis

A sensitivity analysis test was performed around the calibrated values at the center of CCD, to predict the relative contributions of increased cortical stiffness (change in  $k_{mit}^{Stiff}$ ), increased cytoplasmic pressure (change in  $\Delta P$ ) and reduction of cell-cell adhesion (change in  $k_{mit}^{Adh}$ ) during mitotic rounding.

Sensitivity of the response variable  $y$  to change in parameter  $x_i$  is given by the following equation [33]:

$$S_i^{y(x)} = \frac{\partial y(x)}{\partial x_i} \frac{x_i}{y(x)} \quad (\text{B.5})$$

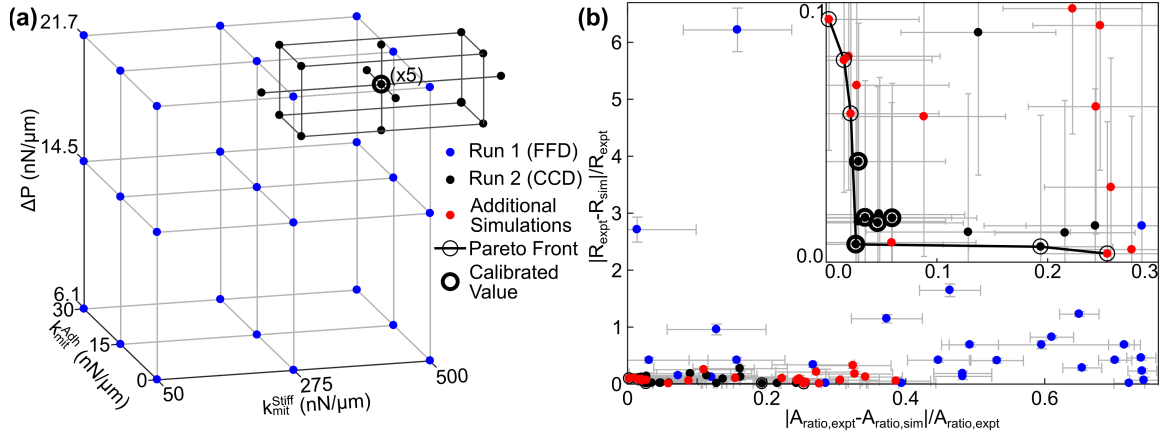


Figure B.2: Response surface method analysis of mechanical properties on regulating mitotic expansion and mitotic rounding. (a) Schematic of initial full factorial design (FFD) for exploring parameter space, and subsequent central composite design (CCD) for developing the response surface models shown in Fig. 4.7. (b) Pareto front indicating computational model parameter values with lowest difference with experimental data for area ratio and normalized roundness. The parameter range defined by the CCD (Run 2) spans parameter variation where the error between experiments and simulations is within the propagated uncertainty of measurements and simulations. Error bars are the standard error of means of the normalized deviation between experiments and simulations.

TABLE B.1:  
VALUES OF THE MODEL PARAMETERS USED TO SIMULATE  
DEVELOPMENT OF EPITHELIAL TISSUE

Interphase parameter	Mitotic parameter	Source or calibration section
$U_{inter}^{II}=0.49nN.\mu m$	$U_{mit}^{II}=21.75nN.\mu m$	Fig. 4.5
$W_{inter}^{II}=0.15nN.\mu m$	$W_{mit}^{II}=6.71nN.\mu m$	Fig. 4.5
$\xi_{inter}^{II}=0.31\mu m$	$\xi_{mit}^{II}=0.58\mu m$	Fig. 4.5
$\gamma_{inter}^{II}=1.25\mu m$	$\gamma_{mit}^{II}=1.34\mu m$	Fig. 4.5
$L_{inter}^{II}=1.56\mu m$	$L_{mit}^{II}=3.12\mu m$	Fig. 4.5
$U_{inter}^{MI}=0.78nN.\mu m$	$U_{mit}^{MI}=4.36nN.\mu m$	Fig. 4.5
$\xi_{inter}^{MI}=0.13\mu m$	$\xi_{mit}^{MI}=0.27\mu m$	Fig. 4.5
$L_{inter}^{MI}=1.56\mu m$	$L_{mit}^{MI}=3.12\mu m$	Fig. 4.5
$U_{inter}^{MMD}=3.9nN.\mu m$	$U_{mit}^{MMD}=3.9nN.\mu m$	Volume exclusion & Fig. 4.2
$W_{inter}^{MMD}=3.9nN.\mu m$	$W_{mit}^{MMD}=3.9nN.\mu m$	Volume exclusion & Fig. 4.2
$\xi_{inter}^{MMD}=0.13\mu m$	$\xi_{mit}^{MMD}=0.13\mu m$	Volume exclusion & Fig. 4.2
$\gamma_{inter}^{MMD}=1.6\mu m$	$\gamma_{mit}^{MMD}=1.6\mu m$	Volume exclusion & Fig. 4.2
$L_{inter}^{MMD}=0.78\mu m$	$L_{mit}^{MMD}=0.78\mu m$	Volume exclusion & Fig. 4.2
$k_{inter}^{Adh}=20nN/\mu m$	$k_{mit}^{Adh}=12nN/\mu m$	[50,59,60] & Fig. 4.5
$L_{max}^{Adh}=0.4\mu m$	$L_{max}^{Adh}=0.4\mu m$	[50,59,60] & Fig. 4.5
$L_{min}^{Adh}=0.062\mu m$	$L_{min}^{Adh}=0.062\mu m$	[50,59,60] & Fig. 4.5
$k_{inter}^{Stiff}=200nN/\mu m$	$k_{mit}^{Stiff}=450nN/\mu m$	[57,58] & Fig. 4.5
$L_{inter}^{Stiff}=0.06\mu m$	$L_{mit}^{Stiff}=0.13\mu m$	[57,58] & Fig. 4.5
$k_{inter}^{Tor}=6.0nN.\mu m$	$k_{mit}^{Tor}=7.0nN.\mu m$	[57,58] & Fig. 4.5

## REFERENCES

1. T. Aegerter-Wilmsen, M. B. Heimlicher, A. C. Smith, P. B. de Reuille, R. S. Smith, C. M. Aegerter, and K. Basler. Integrating force-sensing and signaling pathways in a model for the regulation of wing imaginal disc size. *Development*, 139(17):3221–3231, 2012.
2. A. Amiri, C. Harvey, A. Buchmann, S. Christley, J. D. Shrout, I. S. Aranson, and M. Alber. Reversals and collisions optimize protein exchange in bacterial swarms. *Phys. Rev. E*, 95:032408, Mar 2017. doi: 10.1103/PhysRevE.95.032408. URL <https://link.aps.org/doi/10.1103/PhysRevE.95.032408>.
3. A. Amiri, C. Harvey, A. Buchmann, S. Christley, J. D. Shrout, I. S. Aranson, and M. Alber. Reversals and collisions optimize protein exchange in bacterial swarms. *Physical Review E*, 95(3):032408, March 2017.
4. M. E. Anyan, A. Amiri, C. W. Harvey, G. Tierra, N. Morales-Soto, C. M. Driscoll, M. S. Alber, and J. D. Shrout. Type iv pili interactions promote intercellular association and moderate swarming of *pseudomonas aeruginosa*. *Proc. Natl. Acad. Sci., USA*, 111(50):18013–18018, 2014.
5. I. L. Bajec and F. H. Heppner. Organized flight in birds. *Animal Behaviour*, 78(4):777–789, 2009.
6. R. Balagam and O. A. Igoshin. Mechanism for collective cell alignment in *myxococcus xanthus* bacteria. *PLoS Comput Biol*, 11(8):e1004474, 2015.
7. K. B. Barken, S. J. Pamp, L. Yang, M. Gjermansen, J. J. Bertrand, M. Klausen, M. Givskov, C. B. Whitchurch, J. N. Engel, and T. Tolker-Nielsen. Roles of type iv pili, flagellum-mediated motility and extracellular dna in the formation of mature multicellular structures in *pseudomonas aeruginosa* biofilms. *Environmental microbiology*, 10(9):2331–2343, 2008.
8. A. Be’er, S. K. Strain, R. A. Hernández, E. Ben-Jacob, and E.-L. Florin. Periodic reversals in *paenibacillus dendritiformis* swarming. *Journal of bacteriology*, 195(12):2709–2717, 2013.
9. J. E. Berleman, S. Allen, M. A. Danielewicz, J. P. Remis, A. Gorur, J. Cunha, M. Z. Hadi, D. R. Zusman, T. R. Northen, H. E. Witkowska, et al. The lethal cargo of *myxococcus xanthus* outer membrane vesicles. *Intra-and inter-species interactions in microbial communities*, page 9, 2015.

10. S. P. Bernier, D.-G. Ha, W. Khan, J. H. Merritt, and G. A. O’Toole. Modulation of pseudomonas aeruginosa surface-associated group behaviors by individual amino acids through c-di-gmp signaling. *Research in microbiology*, 162(7):680–688, 2011.
11. E. Bertin. Theoretical approaches to the statistical physics of interacting non-conservative units. *arXiv preprint arXiv:1608.08507*, 2016.
12. B. D. Blackhart and D. R. Zusman. ” frizzy” genes of myxococcus xanthus are involved in control of frequency of reversal of gliding motility. *Proc. Natl. Acad. Sci., USA*, 82(24):8767–8770, 1985.
13. F. Bosveld, O. Markova, B. Guirao, C. Martin, Z. Wang, A. Pierre, M. Balakireva, I. Gaugue, A. Ainslie, N. Christophorou, et al. Epithelial tricellular junctions act as interphase cell shape sensors to orient mitosis. *Nature*, 2016.
14. G. W. Brodland. How computational models can help unlock biological systems. In *Seminars in cell & developmental biology*, volume 47, pages 62–73. Elsevier, 2015.
15. G. W. Brodland, D. Viens, and J. H. Veldhuis. A new cell-based fe model for the mechanics of embryonic epithelia. *Computer methods in biomechanics and biomedical engineering*, 10(2):121–128, 2007.
16. J. Buceta, H. Herranz, O. Canela-Xandri, R. Reigada, F. Sagués, and M. Milán. Robustness and stability of the gene regulatory network involved in dv boundary formation in the drosophila wing. *PLoS One*, 2(7):e602, 2007.
17. I. Bucior, J. F. Pielage, and J. N. Engel. Pseudomonas aeruginosa pili and flagella mediate distinct binding and signaling events at the apical and basolateral surface of airway epithelium. *PLoS Pathog*, 8(4):e1002616, 2012.
18. L. L. Burrows. Pseudomonas aeruginosa twitching motility: type iv pili in action. *Annual review of microbiology*, 66:493–520, 2012.
19. C. Cadart, E. Zlotek-Zlotkiewicz, M. Le Berre, M. Piel, and H. K. Matthews. Exploring the function of cell shape and size during mitosis. *Developmental cell*, 29(2):159–169, 2014.
20. N. C. Caiazza, R. M. Shanks, and G. O’Toole. Rhamnolipids modulate swarming motility patterns of pseudomonas aeruginosa. *Journal of bacteriology*, 187(21):7351–7361, 2005.
21. S. Camazine. *Self-organization in biological systems*. Princeton University Press, 2003.
22. P. Cao, A. Dey, C. N. Vassallo, and D. Wall. How myxobacteria cooperate. *Journal of molecular biology*, 427(23):3709–3721, 2015.



23. A. Cavagna and I. Giardina. Bird flocks as condensed matter. *Annu. Rev. Condens. Matter Phys.*, 5(1):183–207, 2014.
24. G. Charvin, F. Cross, and E. Siggia. Forced periodic expression of g1 cyclins phase-locks the budding yeast cell cycle. *Proc. Natl. Acad. Sci., USA*, 106(16):6632–6637, 2009.
25. R. Chaturvedi, C. Huang, B. Kazmierczak, T. Schneider, J. A. Izaguirre, T. Glimm, H. G. E. Hentschel, J. Glazier, S. Newman, and M. Alber. On multiscale approaches to three-dimensional modelling of morphogenesis. *Journal of the Royal Society interface*, 2(3):237–253, 2005.
26. N. Chen, J. A. Glazier, J. A. Izaguirre, and M. S. Alber. A parallel implementation of the cellular potts model for simulation of cell-based morphogenesis. *Computer physics communications*, 176(11):670–681, 2007.
27. P. Chiang, L. M. Sampaleanu, M. Ayers, M. Pahuta, P. L. Howell, and L. L. Burrows. Functional role of conserved residues in the characteristic secretion ntpase motifs of the pseudomonas aeruginosa type iv pilus motor proteins pilB, pilT and pilu. *Microbiology*, 154(1):114–126, 2008.
28. S. Chiu. Aboav-weaire’s and lewis’ laws—a review. *Materials characterization*, 34(2):149–165, 1995.
29. S. Christley, B. Lee, X. Dai, and Q. Nie. Integrative multicellular biological modeling: a case study of 3d epidermal development using gpu algorithms. *BMC systems biology*, 4(1):1, 2010.
30. J. C. Conrad, M. L. Gibiansky, F. Jin, V. D. Gordon, D. A. Motto, M. A. Mathewson, W. G. Stopka, D. C. Zelasko, J. D. Shrout, and G. C. Wong. Flagella and pili-mediated near-surface single-cell motility mechanisms in p. aeruginosa. *Biophysical journal*, 100(7):1608–1616, 2011.
31. N. C. Darnton, L. Turner, S. Rojevsky, and H. C. Berg. Dynamics of bacterial swarming. *Biophysical journal*, 98(10):2082–2090, 2010.
32. P. Dhar, T. M. Fischer, Y. Wang, T. Mallouk, W. Paxton, and A. Sen. Autonomously moving nanorods at a viscous interface. *Nano letters*, 6(1):66–72, 2006.
33. J. DiStefano III. *Dynamic systems biology modeling and simulation*. Academic Press, 2015.
34. H. Du, Z. Xu, M. Anyan, O. Kim, W. M. Leevy, J. D. Shrout, and M. Alber. High density waves of the bacterium pseudomonas aeruginosa in propagating swarms result in efficient colonization of surfaces. *Biophysical journal*, 103(3):601–609, 2012.

35. H. Du, Q. Nie, and W. R. Holmes. The interplay between wnt mediated expansion and negative regulation of growth promotes robust intestinal crypt structure and homeostasis. *PLoS Comput Biol*, 11(8):e1004285, 2015.
36. A. Ducret, B. Fleuchot, P. Bergam, and T. Mignot. Direct live imaging of cell-cell protein transfer by transient outer membrane fusion in myxococcus xanthus. *Elife*, 2:e00868, 2013.
37. C. Duprat and H. A. Shore. *Fluid-Structure Interactions in Low-Reynolds-Number Flows*. Royal Society of Chemistry, 2015.
38. M. Dworkin. Recent advances in the social and developmental biology of the myxobacteria. *Microbiological reviews*, 60(1):70, 1996.
39. A. G. Evans, H. M. Davey, A. Cookson, H. Currinn, G. Cooke-Fox, P. J. Stanczyk, and D. E. Whitworth. Predatory activity of myxococcus xanthus outer-membrane vesicles and properties of their hydrolase cargo. *Microbiology*, 158(11):2742–2752, 2012.
40. R. Farhadifar, J.-C. Röper, B. Aigouy, S. Eaton, and F. Jülicher. The influence of cell mechanics, cell-cell interactions, and proliferation on epithelial packing. *Current Biology*, 17(24):2095–2104, 2007.
41. F. Farrell, O. Hallatschek, D. Marenduzzo, and B. Waclaw. Mechanically driven growth of quasi-two-dimensional microbial colonies. *Physical review letters*, 111(16):168101, 2013.
42. A. G. Fletcher, M. Osterfield, R. E. Baker, and S. Y. Shvartsman. Vertex models of epithelial morphogenesis. *Biophysical journal*, 106(11):2291–2304, 2014.
43. P. Friedl and D. Gilmour. Collective cell migration in morphogenesis, regeneration and cancer. *Nature reviews Molecular cell biology*, 10(7):445–457, 2009.
44. D. Fristrom. The cellular basis of epithelial morphogenesis. a review. *Tissue and Cell*, 20(5):645–690, 1988.
45. B. S. Gardiner, K. K. Wong, G. R. Joldes, A. J. Rich, C. W. Tan, A. W. Burgess, and D. W. Smith. Discrete element framework for modelling extracellular matrix, deformable cells and subcellular components. *PLoS Comput Biol*, 11(10):e1004544, 2015.
46. O. Gavet and J. Pines. Activation of cyclin b1-cdk1 synchronizes events in the nucleus and the cytoplasm at mitosis. *The Journal of cell biology*, 189(2):247–259, 2010.
47. P. Ghosh, J. Mondal, E. Ben-Jacob, and H. Levine. Mechanically-driven phase separation in a growing bacterial colony. *Proc. Natl. Acad. Sci., USA*, 112(17):E2166–E2173, 2015.

48. M. L. Gibiansky, J. C. Conrad, F. Jin, V. D. Gordon, D. A. Motto, M. A. Mathewson, W. G. Stopka, D. C. Zelasko, J. D. Shrout, and G. C. Wong. Bacteria use type iv pili to walk upright and detach from surfaces. *Science*, 330(6001):197–197, 2010.
49. M. C. Gibson, A. B. Patel, R. Nagpal, and N. Perrimon. The emergence of geometric order in proliferating metazoan epithelia. *Nature*, 442(7106):1038–1041, 2006.
50. W. T. Gibson, J. H. Veldhuis, B. Rubinstein, H. N. Cartwright, N. Perrimon, G. W. Brodland, R. Nagpal, and M. C. Gibson. Control of the mitotic cleavage plane by local epithelial topology. *Cell*, 144(3):427–438, 2011.
51. E. S. Gloag, L. Turnbull, A. Huang, P. Vallotton, H. Wang, L. M. Nolan, L. Mililli, C. Hunt, J. Lu, S. R. Osvath, et al. Self-organization of bacterial biofilms is facilitated by extracellular dna. *Proc. Natl. Acad. Sci., USA*, 110(28):11541–11546, 2013.
52. R. Glowinski, T. Pan, T. Hesla, D. Joseph, and J. Periaux. A fictitious domain approach to the direct numerical simulation of incompressible viscous flow past moving rigid bodies: application to particulate flow. *Journal of Computational Physics*, 169(2):363–426, 2001.
53. G. Guglielmi, J. D. Barry, W. Huber, and S. De Renzis. An optogenetic method to modulate cell contractility during tissue morphogenesis. *Developmental cell*, 35(5):646–660, 2015.
54. B. Gumbiner. Structure, biochemistry, and assembly of epithelial tight junctions. *American Journal of Physiology-Cell Physiology*, 253(6):C749–C758, 1987.
55. A. Haeger, K. Wolf, M. M. Zegers, and P. Friedl. Collective cell migration: guidance principles and hierarchies. *Trends in cell biology*, 25(9):556–566, 2015.
56. D. Hanahan and R. Weinberg. The hallmarks of cancer cell 100: 57–70. *Find this article online*, 2000.
57. B. A. Hart and S. A. Zahler. Lytic enzyme produced by myxococcus xanthus. *Journal of bacteriology*, 92(6):1632–1637, 1966.
58. C. W. Harvey, F. Morcos, C. R. Sweet, D. Kaiser, S. Chatterjee, X. Liu, D. Z. Chen, and M. Alber. Study of elastic collisions of myxococcus xanthus in swarms. *Physical biology*, 8(2):026016, 2011.
59. C. W. Harvey, H. Du, Z. Xu, D. Kaiser, I. Aranson, and M. Alber. Interconnected cavernous structure of bacterial fruiting bodies. *PLoS Comput Biol*, 8(12):e1002850, 2012.

60. J. He and M. W. Deem. Heterogeneous diversity of spacers within crispr (clustered regularly interspaced short palindromic repeats). *Physical review letters*, 105(12):128102, 2010.
61. J. Hodgkin and D. Kaiser. Cell-to-cell stimulation of movement in nonmotile mutants of myxococcus. *Proc. Natl. Acad. Sci., USA*, 74(7):2938–2942, 1977.
62. J. Hodgkin and D. Kaiser. Genetics of gliding motility in myxococcus xanthus (myxobacterales): two gene systems control movement. *Molecular and General Genetics MGG*, 171(2):177–191, 1979.
63. R. Huang, I. Chavez, K. M. Taute, B. Lukić, S. Jeney, M. G. Raizen, and E.-L. Florin. Direct observation of the full transition from ballistic to diffusive brownian motion in a liquid. *Nature Physics*, 7(7):576–580, 2011.
64. B. Jakobczak, D. Keilberg, K. Wuichet, and L. Søgaaard-Andersen. Contact- and protein transfer-dependent stimulation of assembly of the gliding motility machinery in myxococcus xanthus. *PLoS Genet*, 11(7):e1005341, 2015.
65. Y. Jamali, M. Azimi, and M. R. Mofrad. A sub-cellular viscoelastic model for cell population mechanics. *PLoS One*, 5(8):e12097, 2010.
66. J. Jass, S. Schedin, E. Fällman, J. Ohlsson, U. J. Nilsson, B. E. Uhlin, and O. Axner. Physical properties of escherichia coli p pili measured by optical tweezers. *Biophysical journal*, 87(6):4271–4283, 2004.
67. C. Y. Jessica and R. Fernandez-Gonzalez. Quantitative modelling of epithelial morphogenesis: integrating cell mechanics and molecular dynamics. In *Seminars in Cell & Developmental Biology*. Elsevier, 2016.
68. B. A. Jude and R. K. Taylor. The physical basis of type 4 pilus-mediated microcolony formation by vibrio cholerae o1. *Journal of structural biology*, 175(1):1–9, 2011.
69. D. Kaiser. Coupling cell movement to multicellular development in myxobacteria. *Nature Reviews Microbiology*, 1(1):45–54, 2003.
70. M. Klausen, A. Aaes-Jørgensen, S. Molin, and T. Tolker-Nielsen. Involvement of bacterial migration in the development of complex multicellular structures in pseudomonas aeruginosa biofilms. *Molecular microbiology*, 50(1):61–68, 2003.
71. M. Klausen, A. Heydorn, P. Ragas, L. Lambertsen, A. Aaes-Jørgensen, S. Molin, and T. Tolker-Nielsen. Biofilm formation by pseudomonas aeruginosa wild type, flagella and type iv pili mutants. *Molecular microbiology*, 48(6):1511–1524, 2003.
72. T. Kondo, M. Nojiri, Y. Hishikawa, E. Togawa, D. Romanovicz, and R. M. Brown. Biodirected epitaxial nanodeposition of polymers on oriented macromolecular templates. *Proc. Natl. Acad. Sci., USA*, 99(22):14008–14013, 2002.

73. S. Kuchma, A. Ballok, J. Merritt, J. Hammond, W. Lu, J. Rabinowitz, and G. A. O'Toole. Cyclic-di-gmp-mediated repression of swarming motility by *pseudomonas aeruginosa*: the *pilY1* gene and its impact on surface-associated behaviors. *Journal of bacteriology*, 192(12):2950–2964, 2010.
74. S. Kuchma, E. Griffin, and G. O'Toole. Minor pilins of the type iv pilus system participate in the negative regulation of swarming motility. *Journal of bacteriology*, 194(19):5388–5403, 2012.
75. P. Kunda, A. E. Pelling, T. Liu, and B. Baum. Moesin controls cortical rigidity, cell rounding, and spindle morphogenesis during mitosis. *Current Biology*, 18(2):91–101, 2008.
76. T. G. Kuznetsova, M. N. Starodubtseva, N. I. Yegorenkov, S. A. Chizhik, and R. I. Zhdanov. Atomic force microscopy probing of cell elasticity. *Micron*, 38(8):824–833, 2007.
77. S. Lai, J. Tremblay, and E. Déziel. Swarming motility: a multicellular behaviour conferring antimicrobial resistance. *Environmental microbiology*, 11(1):126–136, 2009.
78. O. M. Lancaster, M. Le Berre, A. Dimitracopoulos, D. Bonazzi, E. Zlotek-Zlotkiewicz, R. Picone, T. Duke, M. Piel, and B. Baum. Mitotic rounding alters cell geometry to ensure efficient bipolar spindle formation. *Developmental cell*, 25(3):270–283, 2013.
79. T. Lecuit and P.-F. Lenne. Cell surface mechanics and the control of cell shape, tissue patterns and morphogenesis. *Nature Reviews Molecular Cell Biology*, 8(8):633–644, 2007.
80. F. T. Lewis. A comparison between the mosaic of polygons in a film of artificial emulsion and the pattern of simple epithelium in surface view (cucumber epidermis and human amnion). *The anatomical record*, 50(3):235–265, 1931.
81. E. Licking, L. Gorski, and D. Kaiser. A common step for changing cell shape in fruiting body and starvation-independent sporulation of *myxococcus xanthus*. *Journal of bacteriology*, 182(12):3553–3558, 2000.
82. J. C. Lindbeck, E. A. Goulbourne, M. S. Johnson, and B. L. Taylor. Aerotaxis in *halobacterium salinarum* is methylation-dependent. *Microbiology*, 141(11):2945–2953, 1995.
83. O. J. Maclaren, A. Fletcher, H. Byrne, and P. K. Maini. Models, measurement and inference in epithelial tissue dynamics. *arXiv preprint arXiv:1506.05052*, 2015.
84. R. P. Mann. Bayesian inference for identifying interaction rules in moving animal groups. *PLoS One*, 6(8):e22827, 2011.

85. P. Martin and S. M. Parkhurst. Parallels between tissue repair and embryo morphogenesis. *Development*, 131(13):3021–3034, 2004.
86. R. Matzke, K. Jacobson, and M. Radmacher. Direct, high-resolution measurement of furrow stiffening during division of adherent cells. *Nature Cell Biology*, 3(6):607–610, 2001.
87. C. H. McCONNELL. Mitosis in hydra. mitosis in the ectodermal epitheliomuscular cells of hydra. *Biological Bulletin*, 64(1):86–95, 1933.
88. A. Micoulet, J. P. Spatz, and A. Ott. Mechanical response analysis and power generation by single-cell stretching. *ChemPhysChem*, 6(4):663–670, 2005.
89. S. J. Miller, R. M. Lavker, and T.-T. Sun. Interpreting epithelial cancer biology in the context of stem cells: tumor properties and therapeutic implications. *Biochimica et Biophysica Acta (BBA)-Reviews on Cancer*, 1756(1):25–52, 2005.
90. D. J. Montell. Morphogenetic cell movements: diversity from modular mechanical properties. *Science*, 322(5907):1502–1505, 2008.
91. M. Nagy, Z. Akos, D. Biro, and T. Vicsek. Hierarchical group dynamics in pigeon flocks. *Nature*, 464(7290):890–893, 2010.
92. A. Nematbakhsh, W. Sun, P. A. Brodskiy, A. Amiri, C. Narciso, Z. Xu, J. J. Zartman, and M. S. Alber. Computational study of the impacts of mechanical and physical cell properties on mitotic cell rounding in developing epithelia. *bioRxiv*, page 037820, 2016 (resubmitted for publication).
93. T. J. Newman. Modeling multi-cellular systems using sub-cellular elements. *Mathematical Biosciences and Engineering*, 2(3), August 2005.
94. T. J. Newman. Modeling multicellular structures using the subcellular element model. In *Single-Cell-Based Models in Biology and Medicine*, pages 221–239. Springer, 2007.
95. E. Nudleman, D. Wall, and D. Kaiser. Cell-to-cell transfer of bacterial outer membrane lipoproteins. *Science*, 309(5731):125–127, 2005.
96. M. Osterfield, X. Du, T. Schüpbach, E. Wieschaus, and S. Y. Shvartsman. Three-dimensional epithelial morphogenesis in the developing drosophila egg. *Developmental cell*, 24(4):400–410, 2013.
97. G. A. O’Toole and R. Kolter. Flagellar and twitching motility are necessary for pseudomonas aeruginosa biofilm development. *Molecular microbiology*, 30(2): 295–304, 1998.
98. M. Pargett, A. E. Rundell, G. T. Buzzard, and D. M. Umlis. Model-based analysis for qualitative data: an application in drosophila germline stem cell regulation. *PLoS Comput Biol*, 10(3):e1003498, 2014.

99. B. L. Partridge, T. Pitcher, J. M. Cullen, and J. Wilson. The three-dimensional structure of fish schools. *Behavioral Ecology and Sociobiology*, 6(4):277–288, 1980.
100. J. D. Partridge and R. M. Harshey. Swarming: flexible roaming plans. *Journal of bacteriology*, 195(5):909–918, 2013.
101. D. T. Pathak, X. Wei, A. Bucuvalas, D. H. Haft, D. L. Gerloff, and D. Wall. Cell contact–dependent outer membrane exchange in myxobacteria: genetic determinants and mechanism. *PLoS Genet*, 8(4):e1002626, 2012.
102. A. E. Pelling, Y. Li, W. Shi, and J. K. Gimzewski. Nanoscale visualization and characterization of myxococcus xanthus cells with atomic force microscopy. *Proc. Natl. Acad. Sci., USA*, 102(18):6484–6489, 2005.
103. F. Peruani, L. Schimansky-Geier, and M. Baer. Cluster dynamics and cluster size distributions in systems of self-propelled particles. *The European Physical Journal Special Topics*, 191(1):173–185, 2010.
104. F. Peruani, J. Starruß, V. Jakovljevic, L. Sogaard-Andersen, A. Deutsch, and M. Bär. Collective motion and nonequilibrium cluster formation in colonies of gliding bacteria. *Physical review letters*, 108(9):098102, 2012.
105. M. Prasad, X. Wang, L. He, and D. J. Montell. Border cell migration: a model system for live imaging and genetic analysis of collective cell movement. *Cell Migration: Developmental Methods and Protocols*, pages 277–286, 2011.
106. S. Rafai, L. Jibuti, and P. Peyla. Effective viscosity of microswimmer suspensions. *Physical Review Letters*, 104(9):098102, 2010.
107. N. Ramkumar and B. Baum. Coupling changes in cell shape to chromosome segregation. *Nature Reviews Molecular Cell Biology*, 2016.
108. K. A. Rejniak. An immersed boundary framework for modelling the growth of individual cells: an application to the early tumour development. *Journal of theoretical biology*, 247(1):186–204, 2007.
109. K. A. Rejniak and R. H. Dillon. A single cell-based model of the ductal tumour microarchitecture. *Computational and Mathematical Methods in Medicine*, 8(1): 51–69, 2007.
110. C. Ricotta and L. Szeidl. Towards a unifying approach to diversity measures: bridging the gap between the shannon entropy and rao’s quadratic index. *Theoretical population biology*, 70(3):237–243, 2006.
111. A. M. Rodriguez and A. M. Spormann. Genetic and molecular analysis of cglb, a gene essential for single-cell gliding in myxococcus xanthus. *Journal of bacteriology*, 181(14):4381–4390, 1999.

112. J. P. Rodriguez-Soto and D. Kaiser. Identification and localization of the tgl protein, which is required for myxococcus xanthus social motility. *Journal of bacteriology*, 179(13):4372–4381, 1997.
113. B. Sager and D. Kaiser. Intercellular c-signaling and the traveling waves of myxococcus. *Genes & Development*, 8(23):2793–2804, 1994.
114. D. Sánchez-Gutiérrez, M. Tozluoglu, J. D. Barry, A. Pascual, Y. Mao, and L. M. Escudero. Fundamental physical cellular constraints drive self-organization of tissues. *The EMBO journal*, 35(1):77–88, 2016.
115. S. A. Sandersius, M. Chuai, C. J. Weijer, and T. J. Newman. Correlating cell behavior with tissue topology in embryonic epithelia. *PLoS One*, 6(4):e18081, 2011.
116. C. E. Shannon. Communication theory of secrecy systems. *Bell system technical journal*, 28(4):656–715, 1949.
117. L. J. Shimkets. Social and developmental biology of the myxobacteria. *Microbiological reviews*, 54(4):473–501, 1990.
118. B. I. Shraiman. Mechanical feedback as a possible regulator of tissue growth. *Proc. Natl. Acad. Sci., USA*, 102(9):3318–3323, 2005.
119. J. D. Shrout, D. L. Chopp, C. L. Just, M. Hentzer, M. Givskov, and M. R. Parsek. The impact of quorum sensing and swarming motility on pseudomonas aeruginosa biofilm formation is nutritionally conditional. *Molecular microbiology*, 62(5):1264–1277, 2006.
120. G. Skačej and C. Zannoni. Molecular simulations elucidate electric field actuation in swollen liquid crystal elastomers. *Proc. Natl. Acad. Sci., USA*, 109(26):10193–10198, 2012.
121. J. M. Skerker and H. C. Berg. Direct observation of extension and retraction of type iv pili. *Proc. Natl. Acad. Sci., USA*, 98(12):6901–6904, 2001.
122. O. Sliusarenko, D. R. Zusman, and G. Oster. The motors powering a-motility in myxococcus xanthus are distributed along the cell body. *Journal of bacteriology*, 189(21):7920–7921, 2007.
123. B. Sorce, C. Escobedo, Y. Toyoda, M. P. Stewart, C. J. Cattin, R. Newton, I. Banerjee, A. Stettler, B. Roska, S. Eaton, et al. Mitotic cells contract actomyosin cortex and generate pressure to round against or escape epithelial confinement. *Nature communications*, 6:8872–8872, 2014.
124. M. P. Stewart, J. Helenius, Y. Toyoda, S. P. Ramanathan, D. J. Muller, and A. A. Hyman. Hydrostatic pressure and the actomyosin cortex drive mitotic cell rounding. *Nature*, 469(7329):226–230, 2011.



125. T. Strangeways. Observations on the changes seen in living cells during growth and division. *Proceedings of the Royal Society of London. Series B*, 94(658):137–141, 1922.
126. D. M. Sussman. cellgpu: massively parallel simulations of dynamic vertex models. *arXiv preprint arXiv:1702.02939*, 2017.
127. C. R. Sweet, S. Chatterjee, Z. Xu, K. Bisordi, E. D. Rosen, and M. Alber. Modelling platelet–blood flow interaction using the subcellular element langevin method. *Journal of The Royal Society Interface*, 8(65):1760–1771, 2011.
128. A. Touhami, M. H. Jericho, J. M. Boyd, and T. J. Beveridge. Nanoscale characterization and determination of adhesion forces of *pseudomonas aeruginosa* pili by using atomic force microscopy. *Journal of bacteriology*, 188(2):370–377, 2006.
129. D. van Ditmarsch, K. E. Boyle, H. Sakhtah, J. E. Oyler, C. D. Nadell, É. Déziel, L. E. Dietrich, and J. B. Xavier. Convergent evolution of hyperswarming leads to impaired biofilm formation in pathogenic bacteria. *Cell reports*, 4(4):697–708, 2013.
130. C. Vassallo, D. T. Pathak, P. Cao, D. M. Zuckerman, E. Hoiczyk, and D. Wall. Cell rejuvenation and social behaviors promoted by lps exchange in myxobacteria. *Proc. Natl. Acad. Sci., USA*, 112(22):E2939–E2946, 2015.
131. L. I. Volakis. *Effect of Myoferlin Depletion on Breast Cancer Cell Motility*. PhD thesis, The Ohio State University, 2011.
132. D. Wall. Molecular recognition in myxobacterial outer membrane exchange: functional, social and evolutionary implications. *Molecular microbiology*, 91(2):209–220, 2014.
133. O. Wartlick, P. Mumcu, A. Kicheva, T. Bittig, C. Seum, F. Jülicher, and M. Gonzalez-Gaitan. Dynamics of dpp signaling and proliferation control. *Science*, 331(6021):1154–1159, 2011.
134. X. Wei, D. T. Pathak, and D. Wall. Heterologous protein transfer within structured myxobacteria biofilms. *Molecular microbiology*, 81(2):315–326, 2011.
135. S. Weitz, A. Deutsch, and F. Peruani. Self-propelled rods exhibit a phase-separated state characterized by the presence of active stresses and the ejection of polar clusters. *Physical Review E*, 92(1):012322, 2015.
136. H. H. Wensink, J. Dunkel, S. Heidenreich, K. Drescher, R. E. Goldstein, H. Löwen, and J. M. Yeomans. Meso-scale turbulence in living fluids. *Proc. Natl. Acad. Sci., USA*, 109(36):14308–14313, 2012.

137. P. J. Whitcomb and M. J. Anderson. *RSM simplified: optimizing processes using response surface methods for design of experiments*. Productivity press, New York, 2005.
138. C. W. Wolgemuth. Collective swimming and the dynamics of bacterial turbulence. *Biophysical journal*, 95(4):1564–1574, 2008.
139. Y. Wu, A. D. Kaiser, Y. Jiang, and M. S. Alber. Periodic reversal of direction allows myxobacteria to swarm. *Proc. Natl. Acad. Sci., USA*, 106(4):1222–1227, 2009.
140. Z. Yang and P. I. Higgs. *Myxobacteria: genomics, cellular and molecular biology*. 2014.
141. H. Zhang, Z. Vaksman, D. B. Litwin, P. Shi, H. B. Kaplan, and O. A. Igoshin. The mechanistic basis of myxococcus xanthus rippling behavior and its physiological role during predation. *PLoS Comput Biol*, 8(9):e1002715, 2012.
142. J. Zhao, H. Naveed, S. Kachalo, Y. Cao, W. Tian, and J. Liang. Dynamic mechanical finite element model of biological cells for studying cellular pattern formation. In *Engineering in Medicine and Biology Society (EMBC), 2013 35th Annual International Conference of the IEEE*, pages 4517–4520. IEEE, 2013.
143. E. Zlotek-Zlotkiewicz, S. Monnier, G. Cappello, M. Le Berre, and M. Piel. Optical volume and mass measurements show that mammalian cells swell during mitosis. *J Cell Biol*, 211(4):765–774, 2015.